Thermodynamics and Kinetics of DNA Nanostructure Assembly

by

Jeanette Nangreave

A Dissertation Presented in Partial Fulfillment
of the Requirements for the Degree
Doctor of Philosophy

Approved November 2011 by the
Graduate Supervisory Committee:

Hao Yan, Co-Chair
Yan Liu, Co-Chair
Julian J.-L. Chen
Dong-Kyun Seo

ARIZONA STATE UNIVERSITY

December 2011

ABSTRACT

The unique structural features of deoxyribonucleic acid (DNA) that are of considerable biological interest also make it a valuable engineering material. Perhaps the most useful property of DNA for molecular engineering is its ability to self-assemble into predictable, double helical secondary structures. These interactions are exploited to design a variety of DNA nanostructures, which can be organized into both discrete and periodic structures. This dissertation focuses on studying the dynamic behavior of DNA nanostructure recognition processes. The thermodynamics and kinetics of nanostructure binding are evaluated, with the intention of improving our ability to understand and control their assembly.

Presented here are a series of studies toward this goal. First, multi-helical DNA nanostructures were used to investigate how the valency and arrangement of the connections between DNA nanostructures affect super-structure formation. The study revealed that both the number and the relative position of connections play a significant role in the stability of the final assembly. Next, several DNA nanostructures were designed to gain insight into how small changes to the nanostructure scaffolds, intended to vary their conformational flexibility, would affect their association equilibrium. This approach yielded quantitative information about the roles of enthalpy and entropy in the affinity of polyvalent DNA nanostructure interactions, which exhibit an intriguing compensating effect. Finally, a multi-helical DNA nanostructure was used as a model ‘chip’ for the detection of a single stranded DNA target. The results revealed that the rate constant of hybridization is strongly dominated by a rate-limiting nucleation step.

ACKNOWLEDGEMENTS

First and foremost, I would like to thank my husband Ryan, without whom I would not have accomplished all that I have. For his endless support, devotion, patience and love I am eternally grateful. I am also thankful for my darling Emma, who brings sunshine into my world on even the darkest days. Of course, the contribution that my parents have made to my success cannot be overemphasized. For providing me with a loving and memorable childhood, and for always leading by example, I thank you. In addition, I have been blessed with an amazing extended family; I want to express gratitude to my in-laws for the many ways they have supported Ryan and I through the years.

I want to acknowledge my mentors, Dr. Hao Yan and Dr. Yan Liu. Their passion, dedication, and incredible drive are truly inspirational. The personal and professional support that they provided went above and beyond the norm, and for that I am so thankful. I am also grateful to the members of my committee, Dr. Julian Chen and Dr. Don Seo, for their time and guidance. Finally, I want to thank all the past and present graduate students, postdocs, and lab researchers who I have interacted with along the way. Their advice and support have been instrumental to my success.

TABLE OF CONTENTS

Page

CHAPTER Page

LIST OF TABLES

Table Page

LIST OF FIGURES

Figure Page

Chapter 1

DNA, DNA Nanotechnology, and Assembly of DNA Nanostructures

1.1. Introduction

1.1.1. DNA. "D.N.A. … has novel features which are of considerable biological interest." J.D. Watson and F. H. C. Crick (1953) *Nature.* 171, 737-738.

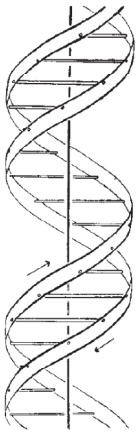

Figure 1.1. The model of double helical DNA proposed by Watson and Crick in 1953.[1]

Deoxyribonucleic acid, or DNA as it's commonly known, is arguably the most important molecule in natural history. Images of double helical DNA are ubiquitous, featured everywhere from college textbooks to popular television crime dramas, a testament to modern society's fascination with nucleic acids. Long before Watson and Crick solved the structure of the now iconic DNA double helix in 1953, DNA was inconspicuously performing its fundamental biological duty, genetic information storage.[1] Often referred to as the 'blue-print' of life, individual molecules of DNA are arranged in a particular order, creating a

biochemical code that specifies the function of individual cells and the development of entire organisms. Since Johann Friedrich Miescher first extracted and characterized DNA from the nuclei of leukocyte cells in 1869, scientists have focused vast energy and resources on uncovering the details of cellular DNA organization, processing, function, and the relationship between DNA and the evolution of the natural world.[2] Remarkably, over a century after Miescher's revolutionary discovery, scientists are still redefining the role of DNA in science and technology.

1.1.2. DNA Nanotechnology. "It appears to be possible to generate covalently joined three-dimensional networks of nucleic acids which are periodic in connectivity and perhaps in space." N. C. Seeman (1982) *J. Theor. Biol.* 99, 237-247.

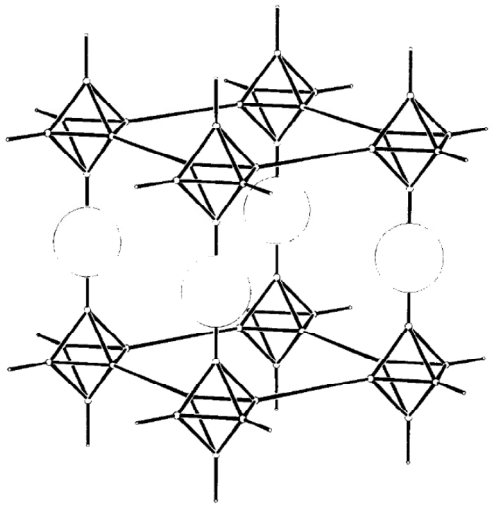

Figure 1.2. A theoretical nucleic acid lattice proposed by Seeman in 1982. The dark lines represent stretches of double helical DNA and the circles represent junction regions.[2]

In 1982 Nadrian Seeman first proposed the idea of using DNA to construct well defined, nanometer-scale arrangements of molecules, giving birth to the field of DNA nanotechnology[3]. He anticipated that the unique structural features of DNA that Watson and Crick recognized made it a valuable engineering material, completely unrelated to its recognized biological function. The suggestion that nucleic acid polymers might have importance outside the context of molecular genetics was incredibly unconventional and forward thinking. With the support researchers around the world, DNA nanotechnology has expanded beyond the production of nanoscale 'tinker-toys' into a diverse, multi-disciplinary field with the potential to develop into a pillar of nanoscale engineering technology[4].

1.2. Structural Properties of DNA

Considering the impressive collection of complex cellular functions in which DNA participates, it is remarkable that the biopolymer is based on relatively simple nucleotide monomers. The structure of DNA

> "has two helical chains each coiled round the same axis … each chain consists of phosphate diester groups joining β-D-deoxyribofuranose residues with 3', 5' linkages. The two chains (but not their bases) are related by a dyad perpendicular to the fibre axis. Both chains follow right-handed helices, but owing to the dyad the sequences of the atoms in the two chains run in opposite directions… the bases are on the inside of the helix and the phosphates on the outside. The configuration of the sugar and the atoms near it is … 'standard configuration', the sugar being roughly perpendicular to the attached base. There is a residue on each chain every 3.4 Å in the z-directions".[1]

Remarkably, the molecular structure of double helical DNA that Watson and Crick proposed over 50 years ago has since been proven valid. Today, the helical 'chains' are referred to as *strands*, and the opposing directionality of the strands is

called an *antiparallel* arrangement. Watson and Crick recognized that "the novel feature of the structure is the manner in which the two chains are held together by the purine and pyrimidine bases".[1] The hydrogen bond interactions between the aromatic nucleobases have since been named 'Watson-Crick' base pairs in honor of their pioneering work.

DNA polymers are classified according to their primary, secondary, and tertiary structures. The primary structure of DNA is composed of individual nucleotide monomers linked together by phosphodiester bonds, with each monomer containing a 2'-deoxy-D-ribose sugar group and an aromatic nucleobase.[5] There are two purine and two pyrimidine nucleobases in DNA, adenine and guanine, and cytosine and thymine, respectively. The resulting polynucleotide chain maintains a 5' to 3' polarity, with amphiphilic features that promote the assembly and preservation of the secondary and tertiary structures.[5]

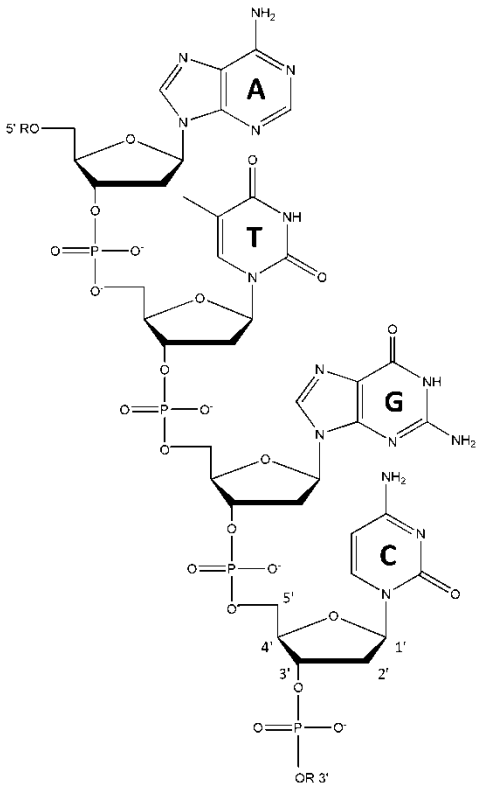

Figure 1.3. The primary structure of DNA.

The predominant secondary structure observed under physiological conditions (and the form of DNA that corresponds to Watson and Crick's report) is referred to as a *B-form* double helix. Double helices are formed by very specific hydrogen bond interactions between the nucleobases of two anti-parallel DNA strands. Adenines from one strand form hydrogen bonds with thymines from a different strand, and similarly, guanines form hydrogen bonds with cystosines.[5] The specific nature of Watson-Crick base pairing results in a double helix composed of two single strands that are said to be complementary.

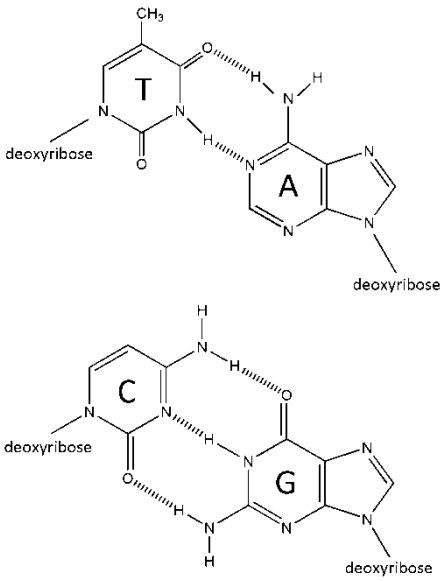

Figure 1.4. The structure of Watson-Crick base pairs.

As Watson and Crick proposed, B-form DNA adopts a right-handed helical structure with a hydrophobic interior composed of paired nucleobases stacked virtually perpendicular to the central polymer axis at 3.4 Å intervals. The plane of each base pair is rotated approximately 36 degrees relative to the adjacent plane, resulting in one complete turn per ~10 base pairs. Thus, the resulting 'helical pitch' (distance between repeating base pair unit planes x number of base pairs per helical turn) of B-form DNA is ~ 34 Å. The π-π stacking interactions between aromatic, nucleobase-paired planes provide a stabilizing force that helps to maintain the double helical structure.[5]

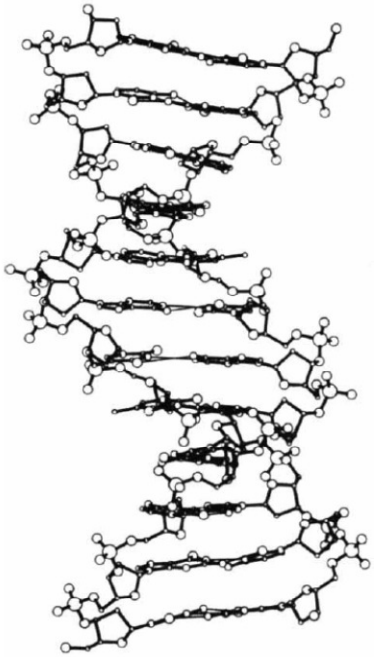

Figure 1.5. Stereoview of a B-form DNA double helix.[6]

The hydrophilic sugar-phosphate backbone spirals around the outside of the helix, imparting a net negative charge to each monomer unit. The precise arrangement of the sugar-phosphate backbone is described by the deoxyribose ring conformation and the N-glycosidic bond angles. In B-form DNA the sugar ring adopts a C2'-endo pucker conformation rather than the alternative C3'-endo conformation to avoid steric clash between two consecutive phosphate groups in the backbone. The N-glycosidic bond between the sugar ring and the nucleobase can adopt either an anti or syn conformation, with the anti configuration dominant in B-form DNA.[5]

The overall chemical structure and spatial arrangement of B-form DNA creates two distinct helical grooves strands referred to as minor and major, which spiral around the outer surface of the paired strands. The major groove is wide

with a moderate depth, while the minor groove is narrow with a nearly equal depth. The bottom of both grooves are defined by the opposite sides of the stacked nucleobase-pair planes which result in unique hydrogen bond donor and acceptor patterns within the plane of the base pair.[5] It is clear that each position along the double helix will possess a unique structure depending on the identity of the base pairs and flanking base pairs. The sequence dependent changes in local structure produce a microheterogeneity that can be exploited for site specific binding and other interactions. The overall helical structure is also influenced by other external factors including solvent, ionic strength, temperature, and hydration.[5] Watson and Crick described the structure of B-form DNA as "an open one" with high water content. They predicted that at lower water content "we would expect the bases to tilt so that the structure could become more compact".[1] Their prediction of a more compact DNA conformation in low humidity was later proven experimentally and is referred to as an *A-form* double helix.

A-form DNA is observed when the relative humidity of the environment decreases to 75% and the salt concentration drops below 10%.[5] As Watson and Crick predicted, the structure of A-form DNA is stout in comparison to B-form, adopting a right handed helix with 11 base pairs per one helical turn and a helical pitch of ~28 Å. The most prominent structural feature of A-form DNA is a net displacement of the nucleobase-pair planes away from the polymer axis accompanied by a 20° tilting of each plane. Another distinguishing property of A-form DNA is that the sugar rings adopt a C3'-endo pucker conformation. Taken

together, these differences result in a narrow and deep major groove and a wide and shallow minor groove.[5]

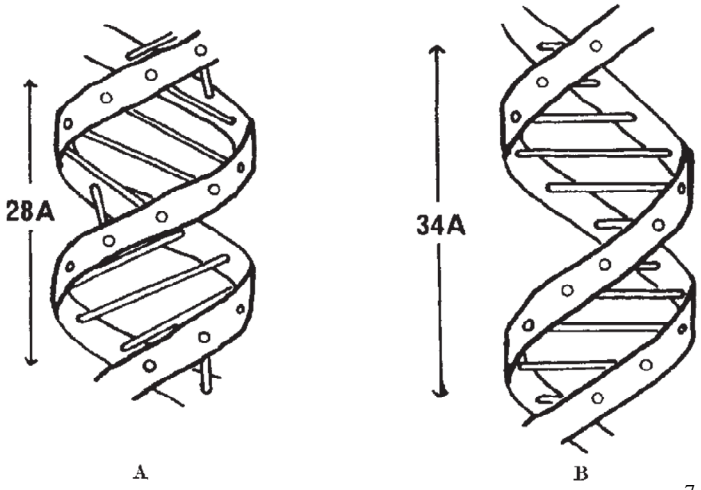

Figure 1.6. A comparison of the structure of A- and B- form DNA.[7]

In high salt conditions and an alternating purine-pyrmidine sequence, double helical DNA can take on an alternative conformation referred to as Z-form. In contrast to A- and B-form DNA, Z-form DNA adopts a left-handed helical structure which is more elongated and slender. Z-form DNA contains 12 nucleobase-pairs per one complete turn and a helical pitch of ~45 Å, with a wide and shallow major groove and a narrow and very deep minor groove. Alternating sugar pucker and N-glycosidic bond conformations result in a left-handed helix with a backbone that appears to zigzag around the outside of the helix.[5]

In addition to the linear secondary structure observed in A-, B-, and Z-form double helices, there are indications that DNA can adopt a number of other unusual structures in a natural setting. Some examples of alternative structures

include hairpin loops, cruciforms that appear within palindromic DNA sequences, pseudoknots, triple helices, branched helical junctions and quartet structures that contain four DNA strands.[5] The natural ability of DNA to adopt a variety of structures provides evidence that DNA might be engineered to form other proposed structures under certain conditions. However, to fulfill Seeman's vision of using DNA to construct well defined, nanometer-scale arrangements of molecules, several other essential elements must be considered.

1.3. Engineering DNA

The mechanical, physical, and environmental properties of materials are important issues that every engineer must consider before launching any construction project. Several examples of descriptors of these properties are Young's modulus, tensile strength, thermal expansion, conductivity, melting temperature, resistivity, raw materials input, eco indicators, etc. A well planned engineering project will include evaluating a material based on these or other relevant properties, and reaching a compromise between ideal and available materials.

In many contexts, the relevant physics of DNA is described by the worm-like chain model which characterizes a polymer using a single parameter, the flexural persistence length.[8] A very informal explanation of this parameter is to say that sections of the polymer that are shorter than the persistence length will behave like a rod, while sections that are longer than the persistence length will behave more flexibly, simulating a random three-dimensional walk. Although the mechanical properties vary according to local sequence and particular helical

structure, the characteristic nucleobase stacking and braided architecture of a DNA double helix impart an unusual level of stiffness. Rigid DNA double helices are necessary if DNA is to be used to build *well-defined* nanoscale structures, in which the position of each atom is relatively fixed. For double stranded DNA in physiological conditions, the persistence length is approximately 50 nm. Put another way, it takes approximately 50 times more energy to bend a DNA double helix into a circle than a single strand of DNA.[8] With a 50 nm persistence length, short pieces of DNA, two or three full turns long (~ 7 – 10 nm), can be regarded as stiff building components suitable for molecular engineering.[9]

In addition to being appropriately stiff enough, DNA is a chemically stable material. This is evidenced by Nature's selection of DNA as the primary molecule to store and maintain vital genetic information for nearly every living organism on earth. Although DNA is subject to hydrolytic, oxidative, and UV-induced damage by external influences, careful control over the local environment can drastically reduce the occurrence of damage.[10] The use of appropriate buffer solutions and protection from UV light should ensure minimal damage to a DNA structure. The double helical structure of DNA is also quite stable. For example, the expected melting temperature (based on the nearest neighbor model) for a random, 20 nucleotide (~ 2 turns) long DNA double helix (ATG CAT GCA TGC ATG CAT GC) is approximately 55°C .[11] With a high thermal stability, DNA can easily be manipulated under normal experimental conditions.

Beyond the advantageous mechanical and physical properties of DNA, there are several practical aspects of DNA that facilitate its use as a material for

molecular engineering. The explosion of scientific interest in studying DNA, either to modify gene expression levels, to optimize certain cellular processes, or to study the molecular biology of the cell, has led to major advances in methodologies for synthesizing DNA.[12] Automated phosphoramidite chemistry is convenient and relatively inexpensive, and permits the assembly of arbitrary sequences containing 100 nucleotides or even more.[13] In addition, the needs of the biotechnology industry have resulted in the creation of many modified phosphoramidites that can be used for non-traditional purposes. Further, with the number of commercially available enzymes that can be used to manipulate DNA, either to ligate different pieces together, cleave specific sequences, phosporylate nucleotides, etc., it is becoming easier and easier to control the molecular structure and behavior of DNA.

Perhaps the most useful property of DNA for molecular engineering is ability of DNA to *self-assemble* into a predictable, double helical secondary structure. In any architectural endeavor, the available tools must always be considered and any material that cannot be manipulated by accessible instruments must be avoided. This is particularly important for nano-scale engineering, where there is a scarcity of tools and techniques to control individual atoms and molecules. With appropriately designed complementarity and reaction conditions, single strands of DNA will self-assemble into double helices with no external pressure, eliminating the need for any sophisticated tools for assembly.

Considered together, the properties of the DNA double helix are unlike those of any other natural or synthetic polymer and make DNA well suited to

serve as an engineering material.[8] For the last 30+ years DNA nanotechnologists have exploited the unique properties of DNA to create an amazing variety of well-defined nanoscale structures.

1.4. Development of DNA Nanotechnology

The most essential behavior of DNA that DNA nanotechnologists rely is the spontaneous self-assembly of single strands into double helices through complementary base pairing. Adenine nearly always forms hydrogen bonds with thymine, and guanine with cytosine. The predictable nature of these intermolecular interactions allows researchers to "program" (design specific, complementary sequences) single stranded molecules of DNA to associate with one another to form double helices. Despite this remarkable ability, double helical molecules have linear topologies and will only sustain one dimensional organization. By specifically designing nucleotide sequence and local strand complementarity, it is possible to produce branched DNA molecules and expand the complexity of potential arrangements.

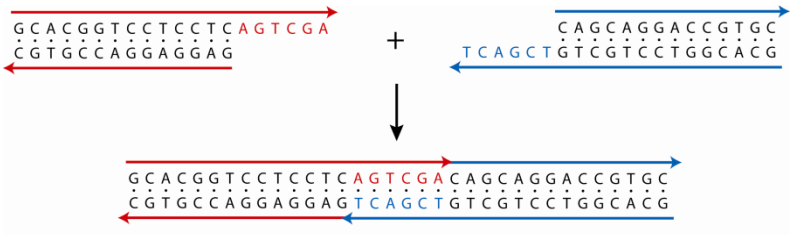

Figure 1.7. 1D organization of two double helical DNA molecules.

Individual branched DNA motifs are analogous to molecular bricks, often referred to as 'tiles', and are used as the basic building blocks of nearly all DNA

nanostructures. Equally important as the individual building blocks is the method employed to bring them together. Without a dependable way to link the tiles, higher-order structures and patterns could not be generated. Attaching single stranded overhangs, or 'sticky ends' (analogous to molecular cement) to the individual components provides a consistent and convenient method for inter-structure association. Since early in the development of DNA nanotechnology, the combination of branched DNA tile motifs and sticky end interactions have been used to generate highly structured and ordered materials.

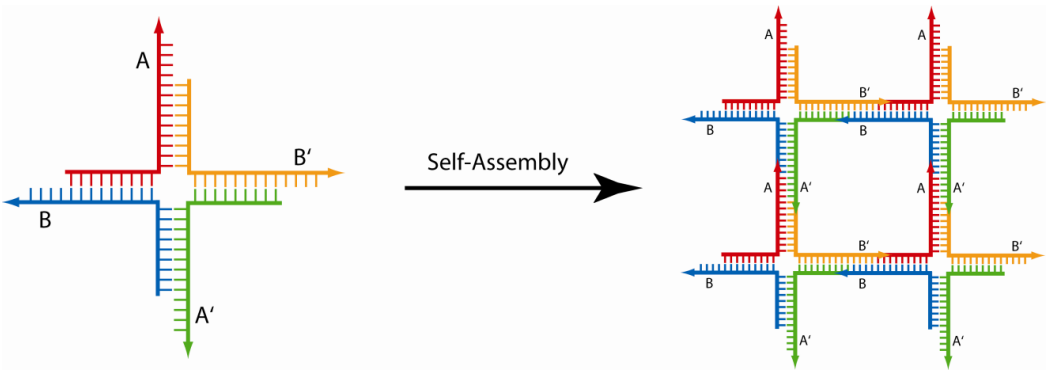

Figure 1.8. Formation of a 2D lattice from a branched DNA molecule with sticky ends.

The very first branched DNA tiles were composed of several double helical 'arms' connected at a single branch point. Initial attempts to use these tiles to construct higher order structures were unsuccessful.[14] Apparently, the inherent flexibility of DNA tile motifs with a single junction point did not facilitate inter-tile association and the creation of higher order structures. The use of multiple crossover points between helices overcame this limitation and provided tiles the rigidity necessary for the assembly of larger objects. In particular, the double

crossover motif first reported in 1993, is the foremost motif in DNA nanotechnology and is used in a wide variety of discrete and periodic assemblies.[15]

Following the production of discrete, geometric DNA objects including a quadrilateral, a cube, and truncated octahedron, researchers used branched DNA tiles for the synthesis of periodic structures.[16-18] Researchers developed a variety of rigid, multiple-crossover building blocks such as double and triple crossover molecules, multi-helical planar molecules, and bundled helix molecules and several types of one and two dimensional periodic networks were constructed.[15, 19-23] The ability to generate precisely patterned structures represented a momentous development and has facilitated the organization of a variety of molecules including proteins, aptamers, metal nanoparticles, and quantum dots.[22-27]

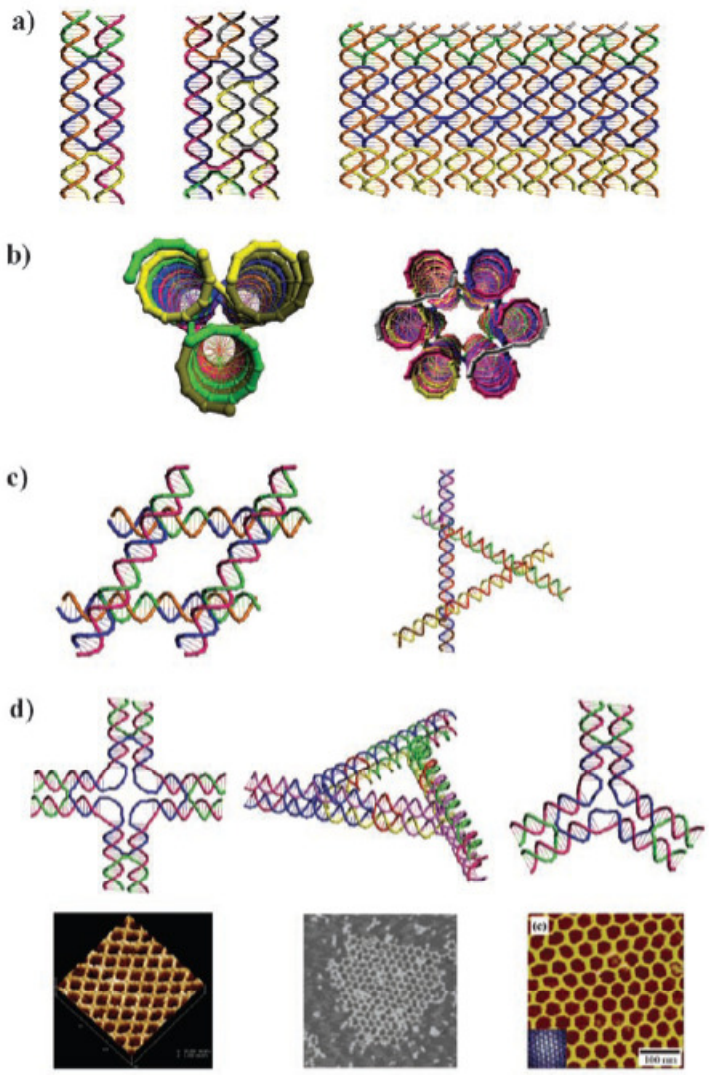

Figure 1.9. Examples of DNA nanostructure building blocks.[23] (a) left: double crossover tile; center: triple crossover tile; right: 12 helix tile. (b) left: three helix bundle tile; right: six-helix bundle tile. (c) left: parallelogram tile; right: triangular tile. (d) left: cross shaped tile and corresponding AFM image (below) of a 2D array of self-assembled tiles; middle: triangular tile and corresponding AFM image (below) of a 2D array of self-assembled tiles; right: 3 point star tile and corresponding AFM image (below) of a 2D array of self-assembled tiles.

1.5. DNA Nanostructure Assembly

1.5.1. Intermolecular Binding Interactions. There are abundant examples of individual 2D and 3D DNA nanostructure building blocks that have been engineered for a range of functions including: scaffolding and study of various nanomaterials, encapsulation of nanoparticles, biosensing etc. Intermolecular binding interactions are vital to almost all of these functions, facilitating communication and cooperation between the individual building blocks, and also, among unique elements within a single building block. This is particularly important in the assembly of higher-order arrays of nanostructures. Incredibly, for all the diversity that exists in the building blocks themselves, they communicate almost exclusively by hybridization of complementary single stranded extensions from the individual units, linking individual DNA nanostructures together to form much larger nanostructure complexes and arrays. In addition, binding of many targets (including oligonucleotides, proteins, metal nanoparticles) to an underlying DNA nanostructure scaffold occurs by the same type of complementary single stranded interactions. The importance of these intermolecular binding interactions cannot be overstated; to exert full control over a nanosystem it is imperative to fully understand the binding character of the interacting units.

Natural systems are a testament to the importance and complexity of intermolecular binding. Reversible, non-covalent associations are fundamental to biochemistry.[28] Noncovalent associations control gene expression, regulate metabolism, govern cell signaling, facilitate the immune reponse and aid in many

other functions. The interactions that are responsible for noncovalent association include hydrogen bonds, dispersion and van der Waals interactions, ionic and other electrostatic interactions, and hydrophobic interactions. These interactions are energetically weak, ranging from 1 to 5 kcal per mole. Simple thermal agitation is enough to disrupt a single weak interaction; however, the likelihood of simultaneously breaking two or more interactions is significantly reduced.[28] A typical biochemical macromolecule-ligand complex will have several weak interactions operating simultaneously, increasing the stability of the complex. The use of multiple binding interactions between partners is a strategy that DNA nanotechnology has embraced. A single DNA nanostructure building block will often contain several sticky end extensions that operate cooperatively to organize the individual units into a more complex pattern. This strategy has played an essential role in the development and success of DNA nanotechnology. Thus, characterizing various aspects of binding phenomena among DNA nanostructures is of the utmost importance.

Non-covalent binding is often evaluated in terms of binding specificity and strength. Binding specificity implies the rejection of incorrect binding partners in favor of the correct ones and is measured in terms of binding constants.[28] High specificity promotes fidelity, the faithful performance of a certain behavior over time, a desirable trait for DNA nanostructures. Binding specificity derives from the highly organized structure of the binding site and the three-dimensional alignment of the interacting groups. All binding events involve the joining of two molecular surfaces and for there to be specificity in binding the

two surfaces should fit together sterically, without substantial gaps in the interface. One of the attractive features of DNA nanostructures is the high level of control over the size and shape of the building blocks, and the arrangement of sticky ends within the structure. Thus, there are a variety of binding situations among DNA nanostructures that can be evaluated.

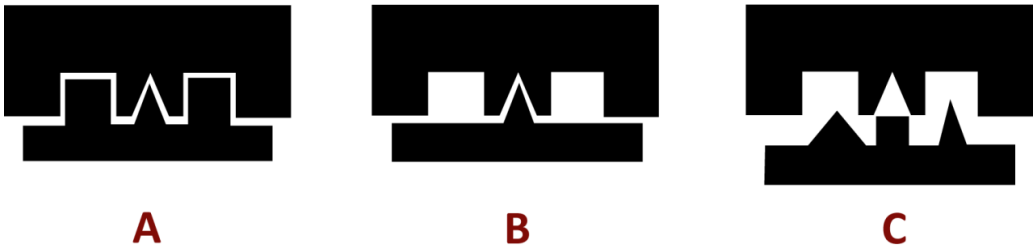

Figure 1.10. Binding affinity and specificity. (a) closely matched complementary surfaces with multiple binding interactions result in high affinity. (b) partially matched complementary surfaces with a single binding interaction results in lower affinity. (c) lack of matching molecular surfaces results in minimal binding affinity.

There are several factors that affect molecular recognition processes. The amount of binding surface that is exposed to solvent has a profound impact on the binding between two molecules.[28] In an unbound state, each molecular surface is exposed to solvent and this solvent must be removed in order for a complex to form. The release of bound solvent is generally entropically favorable and may help drive complex formation. A second, equally important factor is the convergence of functional groups, referred to as polyvalency, which is a potent

way to increase both the strength and specificity of binding.[28] There are many reports that reveal that the strength of association increases dramatically with increasing numbers of points of attachment between two molecules. A polyvalent arrangement of attachment points brings all of the weak interactions together in a very small spatial region. The entropic penalty for gathering individual binding elements together is paid when each molecule is formed, thus, there is a reduced entropic penalty upon complex formation.

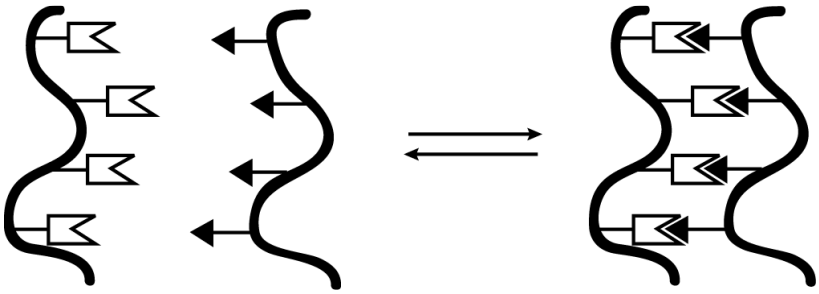

Figure 1.11. Two molecules interact through multiple, simultaneous molecular contacts.

Finally, the conformational flexibility of a molecule will influence its binding performance.[28] Biopolymers such as DNA or proteins are small enough molecules that energy fluctuations are an important determinant of their behavior. Noncovalent interactions are easily broken on an individual basis and are constantly in a state of equilibrium between formed and broken states. Observation of these biopolymers at equilibrium would reveal the presence of a mixture of conformational states and each state would have a different level of interaction with a binding partner. Interconversion between the various states

(microstates) is rapid because there are only small potential energy barriers between them. The fluctuation that occurs over related conformations permits structural flexibility in the biopolymer without the loss of essential structural features. Thus, the functional structure is maintained while dynamic local transitions are permitted. If the binding section is flexible then binding of the molecule to a partner will not require disruption of a stable structure. In effect, this will minimize the activation energy for binding. However, if binding results in the ordering of a flexible, conformationally fluctuating region of the binding site then an entropic penalty will have to be paid. Because some binding energy will be dissipated to cover this entropic debt, the complex will be less stable in terms of free energy.

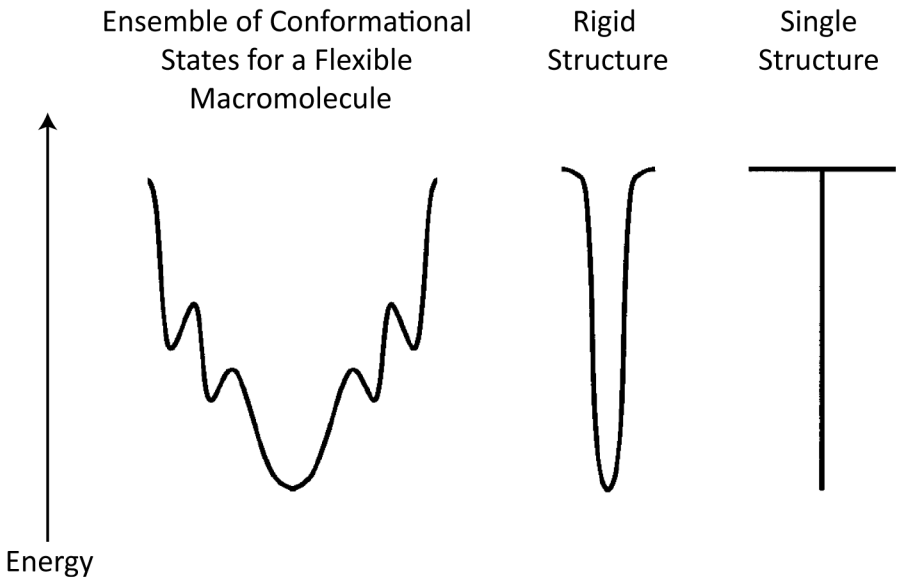

Figure 1.12. Energy diagram reflecting the microstates of a biopolymer.[29] Flexible structures will have an ensemble of related conformations, separated by low-energy barriers (left), while more rigid structures will have a single-energy

minimum (middle). In the extreme case of a completely rigid structure, the distribution of energy states collapses.

Each of these factors is applicable to the assembly of DNA nanostructures. Depending on the structural details of the individual building blocks, the binding region of a DNA nanostructure will have a particular degree of exposure to the solvent and affect the association between two building blocks. Regarding polyvalency, DNA nanostructures are remarkably versatile. It is possible to link two DNA nanostructures together through a single sticky end interaction; and, depending on the size and characteristics of the participating nanostructures it is also possible to connect them through many more interactions, with 25 or more readily achievable. The arrangement and relative location of linkages may also vary depending on the structure of the DNA building blocks. Finally, different DNA nanostructures exhibit an intrinsic, variable degree of conformational flexibility that is the result of particular structural details. There are certain DNA nanostructures that are inherently rigid, while others have proven to be incredibly flexible. Until now, very few studies have examined the effect of these factors on the binding of DNA nanostructures. Herein, various aspects of the role of polyvalency and conformational flexibility of DNA nanostructures are reported.

1.5.2. Characterization of DNA Nanostructure Assembly. Molecular recognition processes can be considered from either a thermodynamic or kinetic perspective, depending on whether a given system is in a state of equilibrium or nonequilibrium. Equilbrium phenomena are describes by thermodynamics

whereas the rate of change of a system is explained by kinetics. Both means of analysis provide useful information about a binding event.

Thermodynamic analysis reflects the overall energy of a system and the transformation of energy that occurs for a given process. Consideration of the thermodynamic aspects of DNA nanostructure assembly will reveal the relative energy (and thus stability) of the reactants and products. The stability is independent of the pathway between the reactants and products and is reflected by the equilibrium constant, K_{eq} of the transformation. There is a fundamental connection between the equilibrium constant and free energy change: $\Delta G^\circ = -RT \ln K_{eq}$. The free energy change of a binding transformation provides a quantitative measure of the relative stabilities of the bound and unbound states of the system. The more negative the free energy change from reactants to products, the more stable the bound complex. However, knowledge of the free energy change alone is not sufficient to characterize the binding process because the change in free energy has both enthalpic (ΔH) and entropic (ΔS) contributions: $\Delta G = \Delta H - T\Delta S$. The magnitude of ΔH indicates the relative contributions of the weak interactions between the binding partners (hydrogen bonding for example), while the magnitude of ΔS helps to indicate the role of solvent reorganization and internal rigidification or flexibility.

The stability of a complex is often measured by a thermal denaturation experiment and is quantitatively described by the T_m (temperature of midtransition) and thermodynamics of assembly.[30] The two most common methods for determining the T_m and thermodynamics of nucleic acid interactions

are optical detection of thermal denaturation and microcalorimetry. Although microcalorimetry is a direct method of measuring transition enthalpy changes, it requires very large sample volumes and can yield free energy values with large errors.[31] Optical detection of thermal denaturation offers the advantages of high sensitivity, thus, very little sample is required. In addition, the entropy and enthalpy values of transition are derived from a two-state van't Hoff analysis of optical melting curves; due to compensating errors in enthalpy and entropy, a van't Hoff analysis provides very accurate measurements of the free energy and melting temperature of a nucleic acid structure.[31]

Optical detection of thermal denaturation usually involves heating/cooling a nucleic acid sample and monitoring the conformational changes that occur at various temperatures via changes in a corresponding optical signal. Often the optical signal is absorbance, but fluorescence is also a very common method used to follow a thermal denaturation experiment. Beyond simply providing a quantitative value for the temperature of midtransition, analysis of a thermal denaturation experiment (in which the folded fraction of a structure or complex is correlated to temperature) yields vital thermodynamic information. The simplest way to derive thermodynamic parameters from optical melting data is to apply the aforementioned van't Hoff analysis to the data, although there are also more rigorous analytical methods.[32, 33]

In this work, Förster resonance energy transfer FRET) was employed to monitor thermal denaturation of dimers of discrete DNA nanostructures. For each dimer investigated, one nanostructure was labeled with a FRET donor, and the

other nanostructure was labeled with a FRET acceptor. The distance between the FRET pair in the assembled dimer is close to the Förster distance, permitting efficient FRET energy transfer between the donor and acceptor when they are near to one another. At low temperatures when the dimer is stable (assembled), the fluorescence emission of the donor will be partially quenched by energy transfer to the acceptor. At high temperatures the dimer is unstable and the monomers will separate from one another, restoring the fluorescence emission of the donor. Monitoring the change in FRET efficiency between the donor and acceptor with respect to temperature generates thermal melting curves, allowing application of the van't Hoff analysis. Chapters 2 and 3 describe thermodynamic characterization of the assembly of several DNA nanostructures in which the role of polyvalency (Chapter 2) and conformational flexibility (Chapter 3) of the participating DNA nanostructures are evaluated.

Kinetic analysis reflects the rate of change of a given transformation and the time required to reach for the system to reach equilibrium. Kinetics can reveal the underlying mechanisms of complex functions, details that are not accessible through thermodynamic analysis. Kinetic stability is related to the pathway between reactants and products and is largely dependent on the activation energy for a given process. Kinetic stability determines the rate constant (k) of a transformation and is entirely independent of the thermodynamic stability. There are several factors that affect the rate of a chemical transformation including concentration of the reactants, steric requirements and accessibility of the reactants (surface area for example), the temperature at which the reaction occurs,

and whether or not any catalysts are present. The accessibility of reactants is a particularly interesting factor in DNA nanostructure assembly, with varying levels of accessibility to binding sites dependent on the structural details of the interacting components. In general, the more accessible the binding site, the faster the rate of transformation. This is because a more accessible binding site will experience a greater number of collisions with the necessary binding partner, leading to a higher frequency of *effective* collisions that result in bound complexes. Chapter 4 describes kinetic characterization of the capture (binding) of an oligonucletide target by a DNA nanostructure in which the role of binding site accessibility is evaluated.

1.6. References

(1) Watson, J. D.; Crick, F. H. C. *Nature.* **1953**, *171*, 737-738.

(2) Dahm, R. *Dev. Biol.* **2005**, *278*, 274-288.

(3) Seeman, N. C. *J. Theor. Biol.* **1982**, *99*, 237-247.

(4) Service, R. F. *Science.* **2011**, *332*, 1141-1143.

(5) Hecht, S. M., Ed. *Bioorganic Chemistry: Nucleic Acids;* Oxford University Press: New York, U.S.A., 1996.

(6) Wing, R.; Drew, H.; Takano, T.; Broka, C.; Tanaka, S.; Itakura, K.; Dickerson, R. E. *Nature.***1980**, *287*, 755-758.

(7) Klug, A. *Nature.***1968**, *219*, 808-812.

(8) Bustamante, C.; Bryant, Z.; Smith, S. B. *Nature.* **2003**, *421*, 423-427.

(9) Seeman, N. C. *Acc. Chem. Res.* **1997**, *30*, 357-363.

(10) Britt, A. B. *Annu. Rev. Plant Physiol. Plant Mol. Biol.* **1996**, *47*, 75-100.

(11) Kibbe, W. A. OligoCalc: an online oligonucleotide properties calculator. *Nucleic Acids Res.* [Online] **2007**, ***35*,** 43-46**.**

http://nar.oxfordjournals.org/content/35/suppl_2/W43.full (accessed July 27, 2011).

(12) Caruthers, M. H. *Science.* **1985**, *230*, 281-285.

(13) Seeman, N. C. *Nanotechnology.* **1999**, *17*, 437-443.

(14) Seeman, N. C. *Annu. Rev. Biophys. Biomol. Struct.* **1998**, 27, 225-248.

(15) Fu, T. J.; Seeman, N. C. *Biochemistry.* **1993**, 32, 3211-3220.

(16) Chen, J. H.; Kallenbach, N. R.; Seeman, N. C. *J. Am. Chem. Soc.* **1989**, 111, 6402-6407.

(17) Chen, J. H.; Seeman, N. C. *Nature.* **1991**, 350, 631-633.

(18) Zhang, Y.; Seeman, N. C. *J. Am. Chem. Soc.* **1994**, 116, 1661-1669.

(19) Li, X. J.; Yang, X. P.; Qi, J.; Seeman, N.C. *J. Am. Chem. Soc.* **1996**, 118, 6131-6140.

(20) LaBean, T. H.; Yan, H.; Kopatsch, J.; Liu, F. R.; Winfree, E.; Reif, J. H.; Seeman, N. C. *J. Am. Chem. Soc.* **2000**, 122, 1848-1860.

(21) Winfree, E.; Liu, F.; Wenzler, L. A.; Seeman, N. C. *Nature.* **1998**, 394, 539-544.

(22) Liu, Y.; Lin, C.; Li, H.; Yan, H. *Angew. Chem. Int. Ed.* **2005**, 44, 4333-4338.

(23) Lin, C.; Liu, Y.; Rinker, S.; Yan, H. *ChemPhysChem.* **2006**, 7, 1641-1647.

(24) Yan, H.; Park, S. H.; Ginkelstein, G.; Reif, J. H.; LaBean, T. H. *Science.* **2003**, 301, 1882-1884.

(25) Loweth, C. J.; Caldwell, W. B.; Peng, X. G.; Alivisatos, A. P.; Schultz, P. G. *Angew. Chem. Int. Ed.* **1999**, 38, 1808-1812.

(26) Deng, Z. X.; Tian, Y.; Lee, S. H.; Ribbe, A. E.; Mao, C. D. *Angew. Chem. Int. Ed.* **2005**, 44, 3582-3585.

(27) Sharma, J.; Ke, Y.; Lin, C.; Chhabra, R.; Wang, Q.; Nangreave, J.; Liu, Y.; Yan, H. *Angew. Chem. Int. Ed.* **2008**, 47, 5157-5159.

(28) Woodbury, C. P. Introduction to macromolecular binding equilibria; CRC Press: New York, 2008; pp 1-20.

(29) Carlson, H. A.; McCammon, J. A. *Mol. Pharmacol.* **2000**, 57, 213-218.

(30) Mergny, J.-L.; Lacroix, L. *Oligonucleotides.* **2003**, 13, 515-537.

(31) SantaLucia, Jr., J.; Turner, D. H. *Biopolymers.* **1997**, 44, 309-319.

(32) Wartell, R. M.; Benight, A. S. *Phys. Rep.* **1985**, 126, 67-107.

(33) Schmitz, M.; Steger, G. *Comput. Appl. Biosci.* **1992**, 8, 389-399.

(34) Gutfreund, H. *Kinetics for the Life Sciences: receptors, transmitters and catalysts*; Cambridge University Press: Cambridge, U.K., 1995.

Chapter 2

Studies of Thermal Stability of Multivalent DNA Hybridization in a Nanostructured System

Adapted with permission from Nangreave, J.; Yan, H.; Liu, Y,: Studies of thermal stability of multivalent DNA hybridization in a nanostructured system, *Biophys. J.* **2009**, *97*, 563-571.

2.1. Abstract

A fundamental understanding of molecular self-assembly processes are important for improving the design and construction of higher-order supramolecular structures. DNA tile based self-assembly has recently been used to generate periodic and aperiodic nanostructures of different geometries, but there have been very few studies that focus on the thermodynamic properties of the inter-tile interactions. Here we demonstrate that fluorescently-labeled multihelical DNA tiles can be used as a model platform to systematically investigate multivalent DNA hybridization. Real-time monitoring of DNA tile assembly using fluorescence resonance energy transfer revealed that both the number and the relative position of DNA sticky-ends play a significant role in the stability of the final assembly. As multivalent interactions are important factors in nature's delicate macromolecular systems, our quantitative analysis of the stability and cooperativity of a network of DNA sticky-end associations could lead to greater control over hierarchical nanostructure formation and algorithmic self-assembly.

2.2. Introduction

Biological systems contain a myriad of macromolecular structures formed through self-assembly of interacting molecular components.[1] Emulation of biological self-assembly processes offers great potential for nanofabrication.[2] In recent years, a number of research groups have begun developing nanofabrication methods based on DNA self-assembly.[3-23] The chemical properties of DNA that allow it to successfully function as life's information carrier have been exploited for advances in the field of nanotechnology.[24] The DNA molecule has attractive features for use in nanotechnology as a result of its nanoscale dimensions, its ability to form duplexes and other higher-order structures, and its combined stiffness and flexibility.[25] The exceptional specificity of Watson-Crick hydrogen-bonding interactions allows the convenient programming of synthetic DNA via a simple four-letter alphabet.

The fabrication of a DNA nanostructure begins with the assembly of a collection of deliberately designed single-stranded DNA molecules into branched DNA motifs commonly referred to as DNA tiles. A diverse architectural toolbox of rigid, branched DNA nanostructural motifs that serve as “molecular bricks” has been developed.[26] The most convenient way of bringing individual DNA tiles together to form higher-order structures is by sticky-end cohesion through complementary basepairing, where a sticky end is a short, single-stranded overhang that extends beyond the end of a double-stranded helical DNA molecule.

Despite the importance of inter-tile sticky-end interactions in structural DNA nanotechnology, very few studies of the effect of multivalency and strength of sticky-end cohesion have been performed. Particularly, research on the effect of varying the number and position of sticky ends on the thermodynamics of a multi-tile assembly is lacking. With an enhanced understanding of the thermal stability of a network of sticky-end associations, greater control over nanostructure formation and self-assembly may be achieved. For example, one of the main obstacles in achieving robust algorithmic DNA self-assembly is the presence of several types of errors: structural, nucleation, and growth errors have hampered the development of this field.[9] It may be possible to reduce error rates by carefully tuning the kinetics and thermodynamics of assembly, and studies that provide such quantitative information could lead to better control over the self-assembly process.

Analysis of the thermodynamic stability of DNA architectures has frequently been carried out by way of melting temperature examination. The melting curves of DNA complexes provide a measure of the stability and cooperativity of internal interactions via the transition temperature, and the width of the transition, respectively. Melting curves of DNA complexes are most often acquired by exploitation of the hyperchromatic effect of nucleotides, through measurement of the absorption change (at 260 nm) of basepaired oligonucleotides upon thermal denaturation. There have been many reports on the melting temperatures of discrete DNA nanostructures.[8, 27] However; there have been very few reports on the thermal stability and dynamics of inter-tile sticky-end

associations. This is because the amplitude of the absorbance change for the dissociation of sticky ends (usually only 5–10 nucleotides long) is overshadowed by the much larger absorbance change resulting from the dissociation of the core of the DNA tile.[28] In addition, the existence of multiple intermediate states during the melting of a DNA tile makes the assignment of particular transitions to distinct structural changes very difficult. Additionally, ultraviolet-based melting measurements are restricted to final-product analysis, which constrains the ability to detect and optimize the self-assembly process.

Recently Sacca et al. developed a method to analyze the self-assembly of DNA nanostructures in real-time using temperature-dependent fluorescence resonance energy transfer (FRET) spectroscopy.[29] In this method, the direct monitoring of the self-assembly process is enabled by the precise placement of a pair of FRET fluorophores on two constituent oligonucleotides of a DNA nanostructure. The interfluorophore distance changes as a result of temperature-dependent conformational changes. Correct assembly of the nanostructure upon cooling brings the FRET pair into close proximity and induces maximum FRET efficiency at low temperatures. In contrast, the complete dissociation of the nanostructure upon thermal melting results in separation of the FRET pair and induces minimal FRET efficiency at high temperatures. By monitoring the change of FRET efficiency with temperature, the equilibrium constant of the self-assembly process at each temperature can be obtained. In the case of reversible assembly and disassembly of a DNA nanostructure, application of the van 't Hoff's law yields the enthalpy and entropy changes of the assembly process.

Herein the FRET-based method was used to systematically investigate the behavior and thermal stability of a series of sticky-end associations occurring between two multihelical DNA nanostructures, illustrated in Figure 2.1a.[30] Two types of multihelical tiles, 4HX and 6HX, were used, differing only in the number of helices contained in each tile. Within each tile, the DNA helices are arranged parallel to adjacent helices and are joined with oligonucleotides that cross-over from one helix to its neighboring helices.

As shown in Figure 2.1, two 4HX tiles (4HX-A and 4HX-B) capable of specifically associating to form heterodimers through 1–4 sticky-end connections were designed and constructed. Each of the 4HX tiles were formed from nine constituent DNA oligomers that self-assembled into the desired tiles when mixed together and annealed. The 3′ ends of the four helices were extended with six-nucleotide-long, single-stranded overhangs, which functioned as sticky ends for the tile-tile association (on the right side of tile A and the left side of tile B). The complementarities of the corresponding sticky ends on tile A and B are labeled with numbers (1 and 1′, etc.) and represented by different colors and shapes. The sequences of all of the sticky ends were designed to contain the same GC content. A systematic study of sticky-end associations between the tiles in the dimer assembly was carried out by analyzing a variety of combinations of number and position of sticky-end pairs. Figure 2.1b illustrates the different designs of the 4HX dimers labeled from #1 to #8. Between the tiles, the helical positions without sticky-end attachments were trimmed to be blunt ends to prevent them from interfering with dimer formation. Oligomers on the opposite (outer) end of the

tiles contain a poly-thymine (T4) sequence extending outward to prevent the undesired, nonspecific association of tiles through blunt-end stacking, thus ensuring that the resulting assemblies are discrete dimers.

To rule out the possibility that base-stacking interactions between the tiles (at positions without sticky-end attachments) might have an influence on the experimental measurements, four thymines were added to the corresponding oligomers in control experiments. The melting curves obtained for the standard and control samples were not substantially different, indicating that the end-to-end base stacking interactions in the designs here provided no significant contribution to the thermal stability of the dimers. It should be noted that there are approximately three full helical turns (31 basepairs) separating neighboring inter-tile crossover points, so that the two tiles in the dimer should lie within the same plane. However, for dimer assemblies connected by a single sticky-end association, tiles A and B may be positioned slightly out of plane, due to a twisting (underwinding) of the hybridized helical region of the connection. The effect of this twisting on the stability of these dimers will be discussed later.

Additionally, two 6HX tiles (6HX-A and 6HX-B) that are capable of forming heterodimers with a number of sticky-end connections ranging from one to six were also prepared. The 6HX tiles were formed from 14 constituent oligomers that self-assembled into the desired tile when mixed together and annealed. Similarly, selected 3′ ends of the six helices were extended with six-nucleotide-long complementary sticky ends to facilitate dimer formation. For 6HX tiles, the sequences of the sticky-end pairs were kept the same for designs

with the same number of sticky-end connections. For example, for designs with one sticky-end connection the same sticky-end sequence was used for each of the six possible positions. Additionally, for designs with two sticky-end associations, two pairs of unique sticky-end sequences with the same GC content were used for each of the 15 possible arrangements. For the 6HX system, all possible combinations of number and position of sticky ends were constructed and analyzed.

The thermal-stability of the various dimer assemblies was determined by the aforementioned FRET method. To enable the in situ monitoring of the self-assembly process by FRET spectroscopy, the A and B tiles of the heterodimer were labeled with a pair of fluorescent dyes. One constituent oligomer from tile A was labeled with a FRET donor, Fluorescein (Ab_{max} = 495 nm, Em_{max} = 520 nm) and one constituent oligomer from tile B was labeled with a FRET acceptor, TAMRA (Ab_{max} = 559 nm, Em_{max} = 583 nm). The fluorescent dyes were covalently attached to the corresponding oligomers on the 5′ end of strands not carrying a sticky end, on the third and second helical positions of tiles A and B, respectively (Figure 2.1). All dimer constructions investigated shared the same pair of fluorescently-labeled oligomers. When the individual DNA strands comprising each tile are annealed and assembled into the dimer superstructure, the FRET pair is brought into proximity and induces maximum FRET efficiency. The dissociation of the dimer superstructure results in separation of the FRET pair and leads to minimal FRET efficiency.

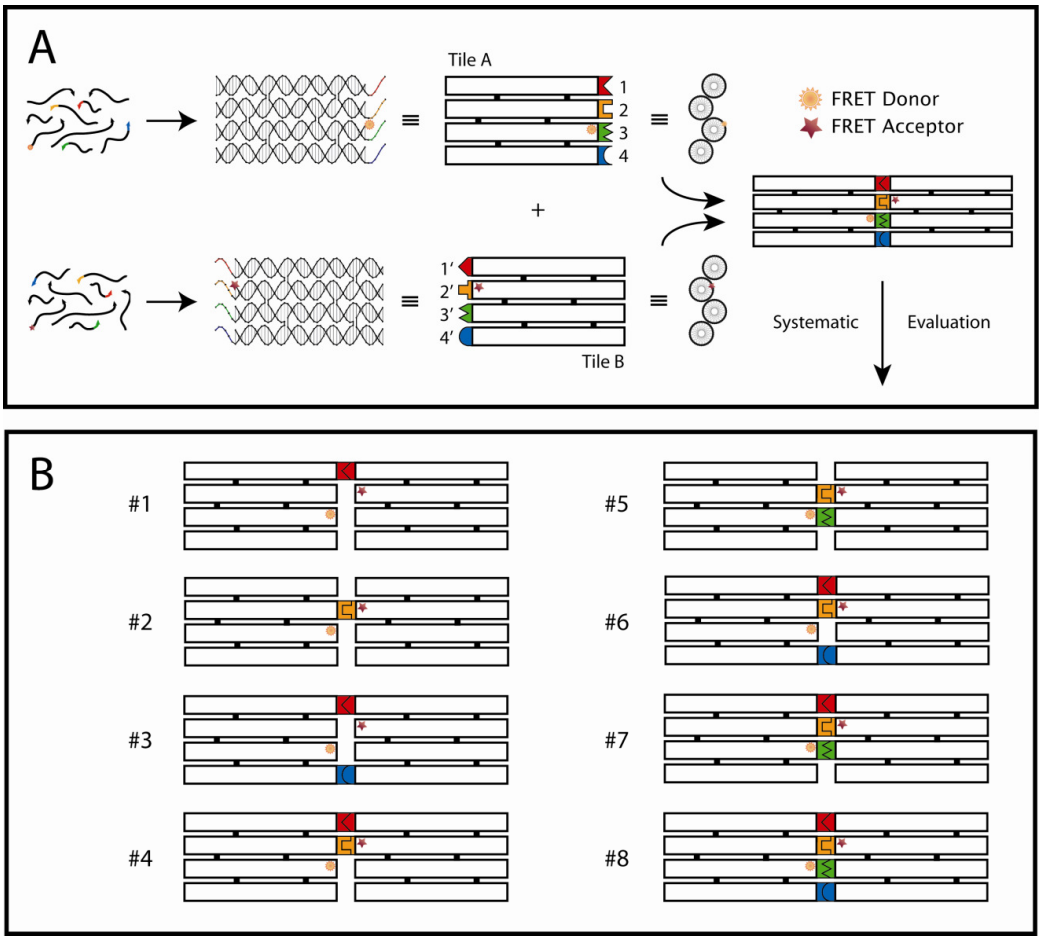

Figure 2.1. (a) Schematic representation of the labeling strategy used for the FRET thermal analysis of the self-assembly of DNA tile dimers. The FRET pair is Fluorescein (orange sunburst, donor) at the right end of helix 3 on tile A, and TAMRA (red star, acceptor) at the left end of helix 2 on tile B. Correct formation of the DNA tile dimer through sticky-end association (labeled by numbers and represented by different colors and complementary shapes) brings the FRET pair into proximity leading to efficient FRET. (b) Schematic representation of the collection of designs (#1–#8) for the 4HX dimers formed though numbers of sticky ends ranging from 1 to 4, with variable sticky-end positions.

2.3. Materials and Methods

2.3.1. Self-Assembly of DNA Nanostructures. All DNA strands used for assembly of nanostructures were purchased from Integrated DNA Technologies and purified by denaturing PAGE gel electrophoresis (6–10% acrylamide in 1× TBE buffer: 89 mM Tris base, 89 mM Boric acid, 2mM EDTA, pH 8.0) or HPLC for the dye-labeled DNA oligomers. Assembly of the individual tiles as well as the final superstructure was performed by mixing equimolar amounts of all the oligomers present in the structures at a final concentration ranging from 0.6 to 1 μM in 1× TAE Mg buffer (40 mM Tris base, 20 mM Acetic acid, 2 mM EDTA·Na_2·12H_2O, 12.5 mM $(CH_3COO)_2Mg·4H_2O$). The oligomer mixture was heated at 95°C for 5 min and cooled down to 25°C (~ −0.1°C/min) using an automated real-time PCR thermocycler (Mx3005P; Stratagene, La Jolla, CA). The formation of self-assembled individual tiles as well as the final superstructure was demonstrated by nondenaturing PAGE (8% acrylamide in 1× TAE Mg buffer (40 mM Tris base, 20 mM Acetic acid, 2 mM EDTA·Na_2·12H_2O, 12.5 mM $(CH_3COO)_2Mg·4H_2O$; 150V, 20°C for 5 h) and FRET spectroscopy.

2.3.2. Fluorescence Spectroscopy. The fluorescence thermal curves were measured in eight-well optical tube strips using a MX3005P real-time thermocycler (Stratagene). After mixing equimolar amounts of all oligomers present in the nanostructures (0.3 or 0.5 μM concentration in 1× TAE Mg buffer), 20 μL of each sample was pipetted into Stratagene optical tube strips and closed with Stratagene optical caps. The samples were heated to 95°C for 5 min, and upon excitation at 492 nm, the fluorescence emission of fluorescein (522 nm) was

monitored while the temperature was reduced from 80°C to 25°C with a temperature gradient of −0.1°C/min. Heating cycles were performed in the same manner: after one cooling cycle the samples were held at 25°C for 10 min and upon excitation at 492 nm, the fluorescence emission was monitored while the temperature was increased from 25°C to 80°C with a temperature gradient of +0.1°C/min. All experiments were repeated at least in duplicate to ensure reproducibility. For all the nanostructures investigated, two samples were prepared with identical experimental conditions: One sample contained the donor on tile A and the acceptor on tile B (A^DB^A), whereas the second sample contained only the donor fluorophore on tile A and corresponding unlabeled oligomer on tile B (A^DB) as the reference. This scheme allowed for the measurement of the decrease in donor emission resulting from energy transfer to the TAMRA acceptor to calculate the FRET efficiency. This method also allowed for the variations in the donor's fluorescence as a result of changes in temperature to be taken into account. Analysis of the data illustrated variations in the FRET efficiency of the donor-acceptor pair during the self-assembly process.

2.4. Results and Discussion

The proper formation of the AB tile dimers was confirmed by native polyacrylamide gel electrophoresis. The AB tile dimer constructs exhibited a distinct mobility as compared to that of the individual tiles. The efficiency of energy transfer (E) was determined at each temperature according to

$$E(T) = 1 - \frac{I_{DA}(T)}{I_D(T)}$$

where I_{DA} and I_D are, respectively, the fluorescence intensities of the FRET donor (Fluorescein) in the presence and absence of the FRET acceptor (TAMRA). Assuming the change in the fluorescence intensity of the donor is proportional to the formation of dimers containing the FRET pair, and that the system reaches equilibrium at each temperature as a result of the slow temperature gradient, the fraction of assembled dimer structures at any given temperature $\theta(T)$ is obtained by normalization of FRET efficiency as a function of temperature,

$$\theta(T) = \frac{E(T) - E_{min}}{E_{max} - E_{min}}$$

where E_{min} represents the minimum FRET efficiency that occurs when the superstructure is completely dissociated, and E_{max} represents the maximum FRET efficiency that occurs when the superstructure is completely assembled. $\theta(T)$ gives information about the equilibrium shift of the reaction of A+B ↔AB as a function of temperature: at E_{max}, all DNA tiles are fully assembled to form AB dimers, and therefore $\theta = 1$. In contrast, at E_{min}, all DNA strands are completely dissociated and therefore $\theta = 0$.

The intensity of fluorescence emission of the FRET donor in the presence and absence of the acceptor, I_{DA} and I_D, was obtained for each pair of samples. The raw data were plotted against temperature in the 25–80°C range and the heating and cooling profiles were superimposed (a typical sample is shown in Figure 2.2a). After determining the assembled fraction of dimers at each temperature using the above equations, θ was also plotted against temperature with the heating and cooling profiles superimposed (Figure 2.2b). It is observed

that the heating and cooling profiles for an individual construct followed each other closely with negligible hysteresis, especially for the normalized data (Figure 2.2b), indicating the reversibility of the dimer formation and dissociation processes.

The raw fluorescence intensity data (Figure 2.2a) reflects the assembly process for a typical sample. During the assembly (cooling) process, the A^DB^A constructs exhibited a minor and gradual increase in the donor emission as a result of changes in temperature, in addition to two sharp decreases in the donor emission at the characteristic transition temperatures, at ~62°C and ~52°C, respectively. In contrast, the A^DB reference sample (donor only) exhibited two sharp transitions—a similar decrease at ~62°C, but then an increase at ~52°C, in the opposite direction of the change for the A^DB^A sample. For both samples, the decrease in donor emission at ~62°C corresponds to the formation of the individual DNA tiles from their constituent strands during the cooling phase. It is known that for a fluorescein dye conjugated to DNA, the fluorescence quantum yield decreases as the DNA transforms from single-stranded to double-stranded, possibly due to weak, noncovalent interactions of the dye with the DNA helix.[31] This transition, occurring in both samples, has a similar magnitude of change, thus a subtraction operation will cancel out this transition. For both samples, the transition at ~52°C corresponds to the dimer formation. The increase of PL for the A^DB sample may result from the formation of sticky-end associations, expelling the donor fluorophore out of the DNA helix by electrostatic or steric repulsion, thereby yielding a higher fluorescence emission. On the other hand, the decrease

of the donor emission at ~52°C for the dimer containing the FRET pair is a result of the FRET donor and acceptor being forced into close proximity, inducing maximum FRET efficiency, thus decreasing the donor emission. The subtraction of the two curves and normalization results in the curves shown in Figure 2.2b, which exhibit only one transition that is directly related to the dimer formation.

The transition temperature (melting temperature) was obtained by fitting the first derivative of θ versus temperature with a Gaussian function,

$$Y = Y_0 + \frac{A}{w\sqrt{\pi/2}} e^{-2\left(\frac{T-T_m}{w}\right)^2}$$

where T_m is the midpoint of the transition temperature, and w is ~0.849 × the full width of the peak at half-height (Figure 2.2c). All the constructs analyzed showed a reversible thermal transition, allowing the application of the van 't Hoff law.

For van 't Hoff analysis, the variation of the equilibrium constant (K_{eq}) with temperature is used to obtain the enthalpy and entropy changes of the complex formation. The equilibrium constant of dimer formation can be expressed as a function of the assembled fraction of dimers at equilibrium,

$$K_{eq} = \frac{\theta}{C_0(1-\theta)^2}$$

where C_0 is the molar concentration of the individual tiles in the mixture, and θ is the assembled fraction of the dimer structure at equilibrium assuming a two-state transition. The following equation describes K_{eq} as a function of temperature,

$$K_{eq} = \frac{-\Delta H}{RT} + \frac{\Delta S}{R}$$

where ΔH is the enthalpy change and ΔS is the entropy change. Plots of ln K_{eq} versus $1/T$ in the temperature range of the transitions were linear, indicating that ΔH and ΔS are temperature-independent (Figure 2.2d). The van 't Hoff enthalpy and entropy changes for the reversible thermal transitions allowed the calculation of changes in free energy for the assembly process using the Gibbs equation,

$\Delta G = \Delta H - T\Delta S$,

where T is 298 K (25°C).

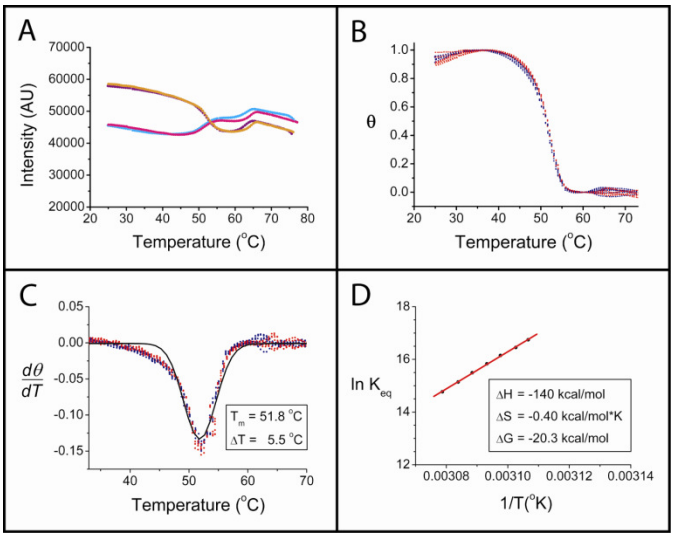

Figure 2.2. Illustration of data analysis for a typical sample (design #6 as shown in Figure 2.1b). (a) The raw data (fluorescence intensity versus temperature) are read directly from the real-time PCR thermocycler detector, with the heating and cooling curves for the A^DB^A sample in orange and cyan, respectively, and the heating and cooling curves for A^DB in magenta and olive, respectively. (b) The plot of normalized FRET efficiency, θ, as a function of temperature. Eight profiles for both heating (*red*) and cooling (*blue*) are plotted together here, exhibiting negligible hysteresis. In this figure only one transition, at ~52°C, is observed. (c) The first derivative of the profiles in panel *B*, $d\theta/dT$, versus temperature is plotted, and a Gaussian fit yields the transition temperature and the width of the transition (again, eight profiles are superimposed). (d) A linear fit of the van 't Hoff plot generates the changes of enthalpy (ΔH), entropy (ΔS), and thereby the free energy change (ΔG).

The results of data analysis for the 4HX tile constructions are shown in Table 2.1. Analysis of the experimental results reveals that changes in the number and position of sticky ends lead to significant differences in the thermal stability of superstructure associations.

No. of sticky ends	Positions of sticky ends	T_m (°C)	$w/2$ (°C)	$-\Delta H$ (kcal/mol)	$-298\Delta S$ (kcal/mol)	ΔG (kcal/mol)
1	1	28.6 ± 0.8	5.5 ± 0.8	85.5 ± 26	75.1 ± 26	–10.5 ± 0.5
	2	34.4 ± 0.2	5.5 ± 0.4	87.5 ± 5.5	75.7 ± 5.4	–11.7 ± 0.3
2	1, 4	42.0 ± 0.8	3.5 ± 0.4	82.4 ± 13	69.1 ± 12	–13.3 ± 0.8
	2, 3	44.6 ± 2.2	4.9 ± 0.4	105.1 ± 7.8	89.7 ± 7.5	–15.3 ± 0.5
	1, 2	46.5 ± 1.2	4.0 ± 0.9	116.6 ± 19	99.8 ± 17	–16.8 ± 1.7
3	1, 2, 4	51.8 ± 0.2	2.7 ± 0.1	166.4 ± 15	143.9 ± 14	–22.5 ± 1.3
	1, 2, 3	53.3 ± 0.5	3.0 ± 0.2	148.2 ± 11	126.4 ± 10	–21.7 ± 1.1
4	1, 2, 3, 4	54.7 ± 0.9	2.9 ± 0.3	143.7 ± 27	121.6 ± 25	–21.9 ± 2.5

Table 2.1. Thermostability data for the 4HX DNA dimers associated through various combinations of number and position of sticky-end interactions. Structural schemes for these samples are shown in Figure 2.1b. The ± values are the standard deviations of the average for both the heating and cooling curves from multiple repeats (12–18 curves for each sample), representing the uncertainty of the experimental measurements.

First of all, there is a clear trend of enhanced thermal-stability with increasing numbers of sticky ends for both 4HX and 6HX tiles. This increase in melting temperature is accompanied by a more negative free energy change. Figure 2.3 summarizes the dramatic effect of increasing the number of sticky-end associations on melting temperature and free energy changes for the 4HX system. For 4HX dimers, there is a considerable increase in melting temperature, by ~ 13°C, when the number of sticky ends between tiles is changed from one to two. Previous studies have qualitatively shown that larger and more stable arrays are generated using two sticky-end associations between constituent tiles as compared to one sticky-end association.[32] The results of the current study provide direct quantitative confirmation of this phenomenon. Increasing the number of sticky-end associations between the 4HX tiles from two to three further elevates the melting temperature of the dimer superstructure by another ~8°C, to above 50°C. It is notable that increasing the number of sticky-end associations further from three to four does not result in as dramatic an increase in melting temperature.

The same trends were observed in the amplitude of the free energy changes (Figure 2.3b). Rather than a purely additive effect, the number of sticky-end associations between the two tiles reaches a saturation point when all of the sticky ends available are fully utilized. The deviation from a linear dependence of the increase of the melting temperature and free energy change on the number of sticky ends may be a result of the less-than-ideal cooperativity of binding. It seems that for the multihelical tiles (n> = 4), addition of the last sticky end (from $n-1$ to n) does not contribute significantly to the overall thermal stability of the

construct. This could be the result of more negative entropy changes, given that the degrees of freedom for the vibrational and rotational motions of the tile dimer decrease when more of the helical ends are employed for the association of two tiles.

The width of the transition reflects the degree of cooperativity of the assembly: the sharper (corresponding to a narrow temperature range) the transition is, the more cooperative the assembly process is. Here the cooperativity is defined vaguely as the number of species involved in the assembly. The error bar in Figure 2.3a represents the width of the transition, which grows smaller as the number of sticky ends involved increases, consistent with the notion that multivalency improves cooperativity.

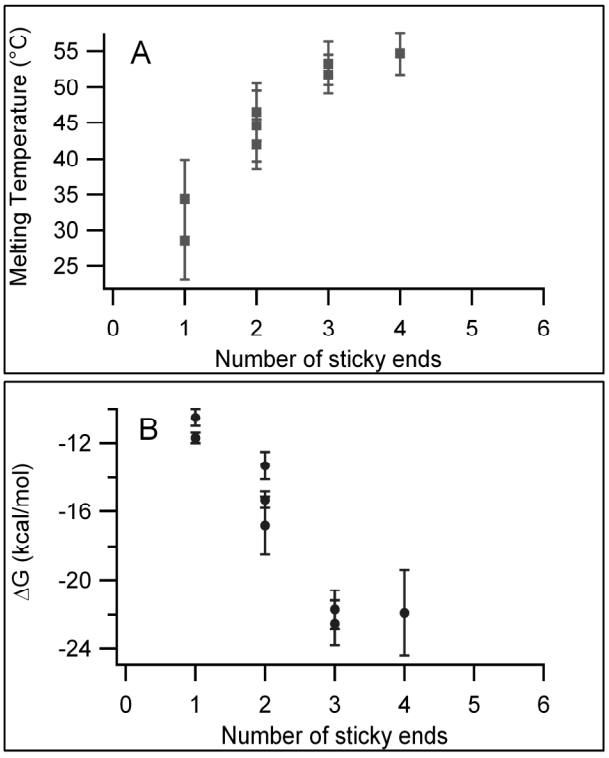

Figure 2.3. (a) Transition temperature and (b) free energy change versus the number of sticky ends for the 4HX dimers. In panel *A,* the error bars reflect the width of the transition temperature (*w*/2), and in panel *B,* the error bars reflect the standard deviation of the calculated free energy changes. The variations in the different data points for the same number of sticky ends (one, two, and three sticky ends) reveal the positional effects of sticky-end placement.

The melting temperature data corresponding to various numbers of sticky-end associations for both the 4HX (*squares*) and 6HX systems (*circles*) are superimposed in Figure 2.4. There are considerable variations in the melting temperatures for dimers with the same number of sticky ends at different positions. The variation in the melting temperature for designs with the same number of sticky ends exceeds the uncertainty of the measurements indicating the differences are real, not merely a result of experimental errors.

On average, 6HX dimers exhibited overall lower melting temperatures than 4HX dimers with the same number of sticky-end associations. This can be explained in analogy to the anharmonic vibration model of a chemical bond between two atoms: with severe elongation of the bond, the dimer structure is doomed to dissociate. This bond weakening occurs when the bond distance is far removed from the equilibrium distance, i.e., the normal length of a B-type DNA duplex with six basepairs, stacked nearly in parallel with a plane gap of 0.34 nm. 4HX and 6HX dimers with the same number of sticky-end associations can be considered to have the same force constant (k). Consequently, dimers formed from larger tiles (6HX) will have a lower vibrational resonance frequency, and will dissociate at a lower. The melting phenomenon of crystalline structures was studied by Einstein a hundred years ago.[33] He derived that a crystalline lattice with a lower characteristic vibrational frequency will have a lower melting temperature than a lattice with a higher characteristic vibrational frequency. The corresponding melting temperature is referred to as the Einstein temperature. Our observations are in agreement with the Einstein theory.

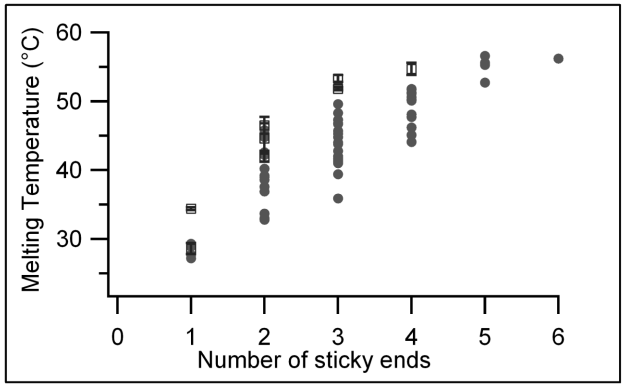

Figure 2.4. Effect of the number of sticky-end associations on the melting temperature of 4HX dimers (*squares*) as compared to 6HX dimers (*circles*). The error bars on the 4HX data are the standard deviations, reflecting the repeatability of the melting temperature measurements using 4–6 repeats for each sample including both heating and cooling. The error bars for the 6HX data are not included to make the figure more readable. The range of the transition temperatures for designs with the same number of sticky ends is generally wider than the error of the measurements, reflecting the dramatic positional effects of sticky-end placement.

The positions of the sticky-end connections have a distinct influence on the thermal-stability of the dimer structure, especially for the 6HX system, which has a large number of different positional combinations available. It is noted that the sequences of the sticky ends for designs with the same number of associations (e.g., 1, 2, and 3 sticky ends) are all the same for the 6HX system, thus the sizeable variations in the melting temperatures observed at different positions can only be explained by the positional effects described below.

First, the absolute position of sticky ends relative to the multihelical tile has a profound effect on the thermal stability of the tile-to-tile connection (Figure 2.5a). Experimental results for designs with one sticky-end association indicate that constructs with sticky ends located at central helical positions (positions 2–5) are significantly more stable than those with sticky ends located at the terminal positions (positions 1 or 6). The same trend was observed for the 6HX dimer constructs with two adjacent sticky-end associations. Figure 2.5b demonstrates the lower melting temperature resulting from a pair of terminal sticky-end positions (pair position 1-2, or 5-6) as compared to a pair of central sticky-end positions (pair position 2-3, 3-4, or 4-5).

The effects of the absolute positions of sticky ends on the dimer stability can be explained by considering the repulsive forces that exist between the multihelical tiles. Constructs in which the sticky end(s) are located on terminal helices experience repulsive forces between the two tiles that do not pass through the center-of-mass of the system. This generates a torque, leading to distortions of the helix or helices involved in the association. Bending (in plane of the tiles) and

twisting (out of plane of the tiles) of the helical region corresponding to the sticky ends could effectively weaken the strength of the complementary base pair hydrogen-bond interactions and disrupt base-stacking interactions between the neighboring base pairs. The in-plane bending effect is expected to be less dramatic for constructs with sticky ends located at central helical positions due to a near-symmetric distribution of charge and mass, thus resulting in less of a reduction of thermal stability. The out-of-plane twisting effect should be less important for any number of sticky-end connections greater than one.

Second, it must be noted that the positional effect is not perfectly symmetric, e.g., when comparing the designs with two sticky ends on terminal helices, sticky ends at positions 1 and 2 yields a higher melting temperature than those at positions 5 and 6. This may be due to the fact that the structural strain of the tile is not evenly distributed, resulting in a distortion of the inner, parallel helices so that the tile structure is not as symmetric as illustrated in the model. The melting of the dimer can be thought of as an unzipping of the sticky-end connections, with the separation of tile A from tile B beginning from the nick points between sticky ends. At the same time the melting of the individual tiles starts from the ends of the helices with no sticky-end connections. In this context it is important to note that the FRET donor and acceptor fluorophores are located on the second and third helices of the dimer structure. When there are no sticky ends extended from helices where the acceptor and donor molecules are attached, the donor and acceptor molecule could be separated before the tiles are fully dissociated at the sticky ends. Consequently, dimers that have sticky-end

connections far away from the donor and acceptor molecule positions could show relatively lower melting temperatures. This can also partially explain the asymmetric positional effect.

Furthermore, for multi-sticky-end associations ($n \geq 2$), the relative position of sticky ends with respect to each other also results in a significant effect on the thermal stability of the tile-to-tile association. Experimental results show that for two sticky-end associations, the wider the gaps between the sticky ends, the less stable the dimer. Figure 2.5c displays the effect of relative position of sticky ends on dimer melting temperature. The melting temperature for a 6HX dimer with two sticky ends located at the two extreme helical positions (positions 1 and 6) is 10°C lower than that of a dimer with two sticky ends adjacent to one another (positions 1 and 2). The previously mentioned effect of absolute sticky-end position on thermal stability is further illustrated with the reduction of another 3°C in the melting temperature of dimers with adjacent sticky ends at terminal helical positions (e.g., positions 1 and 2) as compared to those with adjacent sticky ends at central positions (e.g., positions 3 and 4), as shown in Figure 2.5b. The same trend holds true for 6HX constructs with three sticky-end associations; three sticky ends adjacent to one another, located at central positions of the tile, result in constructs with higher melting temperatures than those with gaps between the sticky ends.

These differences are not only reflected in the changes of the melting temperatures, but also in the enthalpy and entropy changes (Table 2.1). Increasing the number of sticky-end associations from 1 to 2 is expected to double the

enthalpy change, but our results show that this is not the case. Table 2.1 shows that rather than an increase, there is a small decrease in the value of the enthalpy change upon addition of a second sticky-end at position 4 to a dimer with a sticky-end already at position 1. Nevertheless, this additional sticky-end results in a higher melting temperature (from 28 to 42°C) with a more negative free energy change. The much lower melting temperature for one sticky end located at position 1 can be explained by the weakening of the sticky-end association by two kinds of relative motions of the two tiles in the dimer: an out-of-plane motion that disrupts the normal helical twist and an in-plane rotational motion that disrupts the parallel base-stacking. The out-of-plane motion is eliminated for the dimers formed through two sticky ends. The in-plane motions still exist as the two sticky ends alternate in the stretching and compressing phases. However, as the two sticky ends are adjacent to one another, their motions are restricted and must be coordinated to avoid any steric hindrance. Since the sticky ends positioned far apart from one another experience more rotational freedom, this results in a smaller loss of entropy and a smaller enthalpy change. For example, for the 4HX dimers, when the sticky-end connection is changed from one sticky end at position 1 to two sticky ends at positions 1 and 2, the most significant contribution to the more negative free energy change comes from a large change in enthalpy. In contrast, when the sticky-end connection is changed from position 1 to positions 1 and 4, the greater contribution to the more negative free energy change comes from a less negative entropy change, with a negligible difference in the enthalpy change.

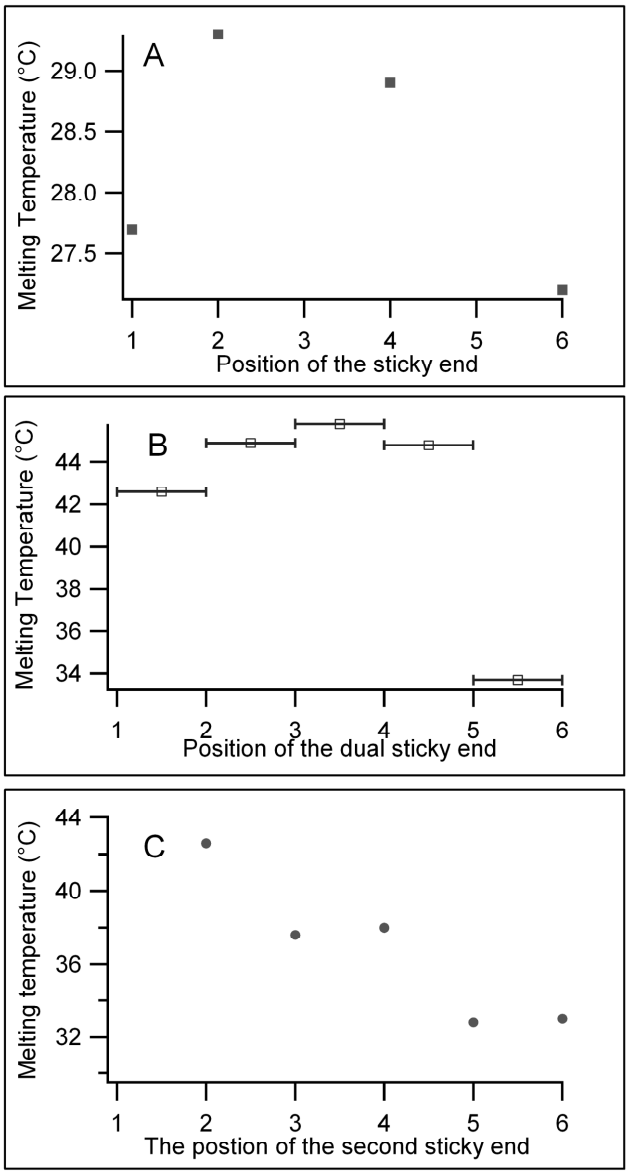

Figure 2.5. (a) Effect of absolute position of one sticky end on the thermal stability (represented by T_m) of 6HX dimers. (b) The effect of absolute position of two adjacent sticky ends on the T_m of 6HX dimers. The horizontal bars in the figure indicate the adjacent positions of the two sticky ends. (c) The effect of relative position of two sticky ends on T_m of 6HX dimers. The horizontal axis is

the position of the second sticky end, where in all cases the first sticky end is positioned on helix 1.

2.5. Conclusion

In summary, we have designed a set of DNA tiles for use as a model system to study the thermal behavior of multivalent DNA hybridization that would otherwise be difficult to achieve using simple DNA duplexes. The real-time monitoring of tile-to-tile associations revealed that both the number and the relative position of sticky-end connections play significant roles in the stability of the final assembly. The differences in the melting temperature and free energy, resulting from various geometric arrangements of sticky ends, provide more options for the deliberate control of self-assembling DNA nanostructures. For example, one could utilize these parameters to design DNA tile sets for algorithmic self-assembly and/or hierarchical self-assembly based on the cooperative interactions determined by multivalent associations. One may also be able to design and produce kinetically trapped products by engineering the sticky-end pairs. Nevertheless, more research must to be done to reveal the fundamental aspects of intricate DNA self-assembly systems that may in turn provide insights into other macromolecular assembly processes found in nature. For example, measurements of enthalpy by calorimetry may be used in the future to gain additional insights on such systems.

2.6. References

(1) Klug, A. *Phil. Trans. R. Soc. Lond. A.* **1994**, *348*, 167-178.

(2) Van Workum, K.; Douglas, J. F. *Phys. Rev. E.* **2006**, *73*, 031502.

(3) Seeman, N. C. *J. Theor. Biol.* **1982**, *99*, 237-247.

(4) Winfree, E.; Liu, F.; Wenzler, L. A.; Seeman, N.C. *Nature.* **1998**, *394*, 539-544.

(5) Chen, J. H.; Seeman, N. C. *Nature.* **1991**, *350*, 631-633.

(6) Yan, H.; Park, S. H.; Finkelstein, G.; Reif, J. H.; LaBean, T. H. *Science.* **2003**, *301*, 1882-1884.

(7) Shih, W. M.; Quispe, J. D.; Joyce, G. F. *Nature.* **2004**, *427*, 618-621.

(8) Goodman, R. P.; Schaap, I. A.; Tardin, C. F.; Erben, C. M.; Berry, R. M.; Schmidt, C. F.; Turberfield, A. J. *Science.* **2005**, *310*, 1661-1665.

(9) Rothemund, P. W.; Papadakis, N.; Winfree, E. *PLOS Biol.* **2004**, *2*, 2041-2053.

(10) Rothemund, P. W. K. *Nature.* **2006**, *440*, 297-302.

(11) Aldaye, F. A.; Sleiman, H. F. *J. Am. Chem. Soc.* **2007**, *129*, 13376-13377.

(12) He, Y.; Ye, T.; Su, M.; Zhang, C.; Ribbe, A. E.; Jiang, W.; Mao, C. *Nature.* **2008**, *452*, 198-202.

(13) Le, J. D.; Pinto, Y.; Seeman, N. C.; Musier-Forsyth, K.; Taton, T. A.; Kiehl, R. A. *Nano Lett.* **2004**, *4*, 2343-2347.

(14) Zhang, J.; Liu, Y.; Ke, Y.; Yan, H. *Nano Lett.* **2006**, *6*, 248-251.

(15) Zheng, J.; Constantinou, P. E.; Micheel, C.; Alivisatos, A. P.; Kiehl, R. A.; Seeman, N. C. *Nano Lett.* **2006**, *6*, 1502-1504.

(16) Sharma, J.; Chhabra, R.; Liu, Y.; Ke, Y.; Yan, H. *Angew. Chem. Int. Ed.* **2006**, *45*, 730-735.

(17) Sharma, J., Y. Ke, C. Lin, R. Chhabra, Q. Wang, Nangreave, J.; Liu, Y.; Yan, H. *Angew. Chem. Int. Ed.* **2008**, *47*, 5157-5159.

(18) Williams, B. A. R.; Lund, K.; Liu, Y.; Yan, H.; Chaput, J. C. *Angew. Chem. Int. Ed.* **2007**, *46*, 3051-3054.

(19) He, Y.; Tian, Y.; Ribbe, A. E.; Mao, C. *J. Am. Chem. Soc.* **2006**, *128*, 12664-12665.

(20) Liu, Y.; Lin, C.; Li, H.; Yan, H. *Angew. Chem. Int. Ed.* **2005**, *44*, 4333-4338.

(21) Malo, J.; Mitchell, J. C.; Venien-Bryan, C.; Harris, J. R.; Wille, H.; Sherratt, D. J.; Turberfield, A. J. *Angew. Chem. Int. Ed.* **2005**, *44*, 3057-3061.

(22) Gothelf, K. V.; LaBean, T. H. *Org. Biomol. Chem.* **2005**, *3*, 4023-4037.

(23) Feldkamp, U.; Niemeyer, C. M. *Angew. Chem. Int. Ed.* **2006**, *45*, 1856-1876.

(24) Seeman, N. C.; Lukeman, P. S. *Rep. Prog. Phys.* **2005**, *68*, 237-270.

(25) Seeman, N. C. *Nature.* **2003**, *421*, 427-431.

(26) Lin, C.; Liu, Y.; Rinker, S.; Yan, H. *ChemPhysChem.* **2006**, *7*, 1641-1647.

(27) LaBean, T. H.; Yan, H.; Kopatch, J.; Liu, F.; Winfree, E; Reif, J. H.; Seeman, N. C. *J. Am. Chem. Soc.* **2000**, *122*, 1848-1860.

(28) Schulman R.; Winfree, E. *Proc. Nat. Acad. Sci*. **2007**, *104*, 15236-15241.

(29) Sacca, B.; Meyer, R.; Feldkamp, U.; Schroeder, H.; Niemeyer, C. M. *Angew. Chem. Int. Ed.* **2008**, *47*, 2135-2137.

(30) Ke, Y.; Liu, Y.; Zhang, J.; Yan, H. *J. Am. Chem. Soc.* **2006**, *128*, 4414-4421.

(31) Sjoback, R.; Nygren, J.; Kubista, M. *Biopolymers*. **1998**, *46*, 445-453.

(32) Ding, B.; Sha, R.; Seeman, N. C. *J. Am. Chem. Soc.* **2004**, *126*, 10230-10231.

(33) Cohen-Tannoudji, C.; Diu, B.; Laloe, F. *Quantum Mechanics, 2nd Edition*. **1977**, *1*, 632.

Chapter 3

DNA Nanostructures as Models for Evaluating the Role of Enthalpy and Entropy in Polyvalent Binding

Adapted with permission from Nangreave, J.; Yan, H.; Liu, Y.: DNA nanostructures as models for evaluating the role of enthalpy and entropy in polyvalent binding, *J. Am. Chem. Soc.* **2011**, *133*, 4490-4497.

3.1. Abstract

DNA nanotechnology allows the design and construction of nanoscale objects that have finely tuned dimensions, orientation, and structure with remarkable ease and convenience. Synthetic DNA nanostructures can be precisely engineered to model a variety of molecules and systems, providing the opportunity to probe very subtle biophysical phenomena. In this study, several such synthetic DNA nanostructures were designed to serve as models to study the binding behavior of polyvalent molecules and gain insight into how small changes to the ligand/receptor scaffolds, intended to vary their conformational flexibility, will affect their association equilibrium. This approach has yielded a quantitative identification of the roles of enthalpy and entropy in the affinity of polyvalent DNA nanostructure interactions, which exhibit an intriguing compensating effect.

3.2. Introduction

Polyvalent interactions are essential to the function of many biological systems. They are characterized by the simultaneous, specific association of multiple ligands on one molecule to complementary receptors on another

molecule and may have unique collective properties as compared to the corresponding monovalent interactions.[1] In medicinal chemistry there is a need to design more effective (efficient) polyvalent inhibitor or promoter drugs, which requires a clear and comprehensive understanding of the thermodynamics of the reaction between inhibitor and target molecules. The collection of ligands in a synthetic, polyvalent molecule can be covalently or non-covalently linked to a backbone molecule, commonly referred to as a scaffold, whose conformational flexibility has a considerable effect on the affinity for a target. Notably, scaffold flexibility can affect both the entropic and enthalpic aspects of binding. To better understand these effects, a polyvalent scaffold with tunable conformational flexibility is required.

DNA nanotechnology offers a unique opportunity to probe the thermodynamics of polyvalent interactions; synthetic DNA nanostructures can be used to gain insight about how subtle changes to ligand/receptor scaffolds may affect their association. DNA nanostructures have previously been used as models to demonstrate that both the number of linkers between scaffolds and their spatial arrangement affect the stability and thermodynamics of intermolecular binding.[2] The basic building blocks of DNA nanostructures, or"tiles", are collections of double-helical DNA domains connected by periodic crossovers. Complementary, single-stranded overhangs, or "sticky ends", are extended from the termini of the double helices to facilitate the intermolecular association of the tiles.[3] For polyvalent binding studies, the double-helical core region of the DNA tile serves as the nanoscale scaffold, with the sticky ends modeling the corresponding

ligands/receptors of intermolecular binding. Small variations in the design of a tile can be introduced to modify its conformational flexibility. In particular, immobile Holliday junction and double crossover tiles have demonstrated unique conformational flexibility, allowing their use as scaffolds for subsequent study.[4-15]

Holliday junction (J) tiles are composed of four DNA strands that self-assemble into four double-helical arms, which are stacked into two helical domains connected at a single branch point, or junction.[4] The junction is formed by a reciprocal crossover, where the two linking strands traverse both helical domains at the same position (Figure 3.1a). There is evidence that transitions between the two possible stacking conformers occur with strong bias toward one conformer, determined by the junction sequence.[16, 17] The J tiles used in the present study have been shown to adopt the stacking preference illustrated in Appendix B.[18] In addition, J tiles have been shown to have a high degree of conformational flexibility, with a wide range of angles between the arms of the junction.[19] As a result, J tiles are well suited to serve as "flexible" scaffolds.

DAE double crossover (DX) tiles consist of five single strands of DNA that self-assemble into two, side-by-side, anti-parallel helical domains with two reciprocal crossovers between the helices.[14] The distance between the intra-tile crossovers is an even number of helical half-turns, resulting in a nearly planar tile (Figure 3.1b). The presence of a second crossover restricts conformational flexibility, and DX tiles were found to be approximately twice as stiff as double-stranded DNA molecules of the same length.[20, 21] Thus, DX tiles represent relatively "rigid" scaffolds.

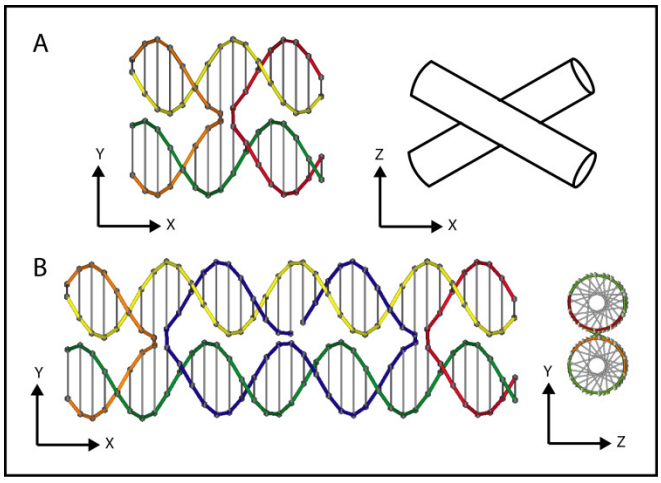

Figure 3.1. Helical structures of J and DX core tiles. (a) Two strands of J (yellow and green) preserve their helical structure, while the remaining two strands (red and orange) form the reciprocal crossover between the helical domains. The equilibrium distribution between the two possible crossover isomers is primarily determined by strand sequence.[16-18] J tiles are flexible at the crossover point with a variety of possible angles between arms.[11, 13, 22, 23] Top view is shown on the right. (b) DX tiles are essentially two J tiles connected by two double-helical arms, with a cyclic central strand. The two crossover points are separated by an even number of half-turns (shown here with four half-turn separation). Side view is shown on the right.

Here, we report the construction of a range of dimer superstructures composed of J and DX tile monomers, which represent flexible and rigid scaffolds, respectively. For both DNA tiles, two double-helical domains in the scaffold allow construction of "bivalent molecules", with the attached sticky ends serving as the sites of intermolecular binding. The distance between the inter-tile crossover points is exactly two full turns, ensuring that both sticky ends can be paired side-by-side in the dimer. A well-established fluorescence resonance energy-transfer (FRET)-based method was employed to study the dimer assembly and disassembly reactions in real-time, permitting the determination of dimer melting temperature and calculation of thermodynamic parameters from the corresponding thermal profiles.[24, 25] In this method, a FRET donor is attached to a selected strand within one DNA tile monomer, while the complementary DNA tile is labeled with the corresponding FRET acceptor. Formation of the dimer (upon cooling) brings the FRET pair into close proximity, and following the temperature-dependent change in FRET efficiency facilitates monitoring of the assembly/disassembly process.

Figure 3.2 illustrates the J and DX monomer tiles used for the assembly of dimers that can be described as flexible (J/J homo-dimer), semi-rigid (DX/J hetero-dimer), and rigid (DX/DX homo-dimer). A-type tiles (J-A and DX-A) contain two unique sticky ends that are five nucleotides each, labeled as 1 and 2, while B-type tiles (J-B and DX-B) contain sticky ends 1′ and 2′, complementary to sticky ends 1 and 2, respectively. These two pairs of complementary sticky ends link A- and B-type tiles together, creating a bivalent association between the

tile scaffolds. This design, where analogous tiles share the same sticky end sequences, ensures that any observed difference in the formation of dimers from these monomeric units is a result of variations in the scaffold core (flexible vs rigid), not the nature of the ligand/receptor interaction. A yellow star and a red triangle identify the position of the FRET donor (fluorescein) and acceptor (TAMRA) fluorophores, respectively.

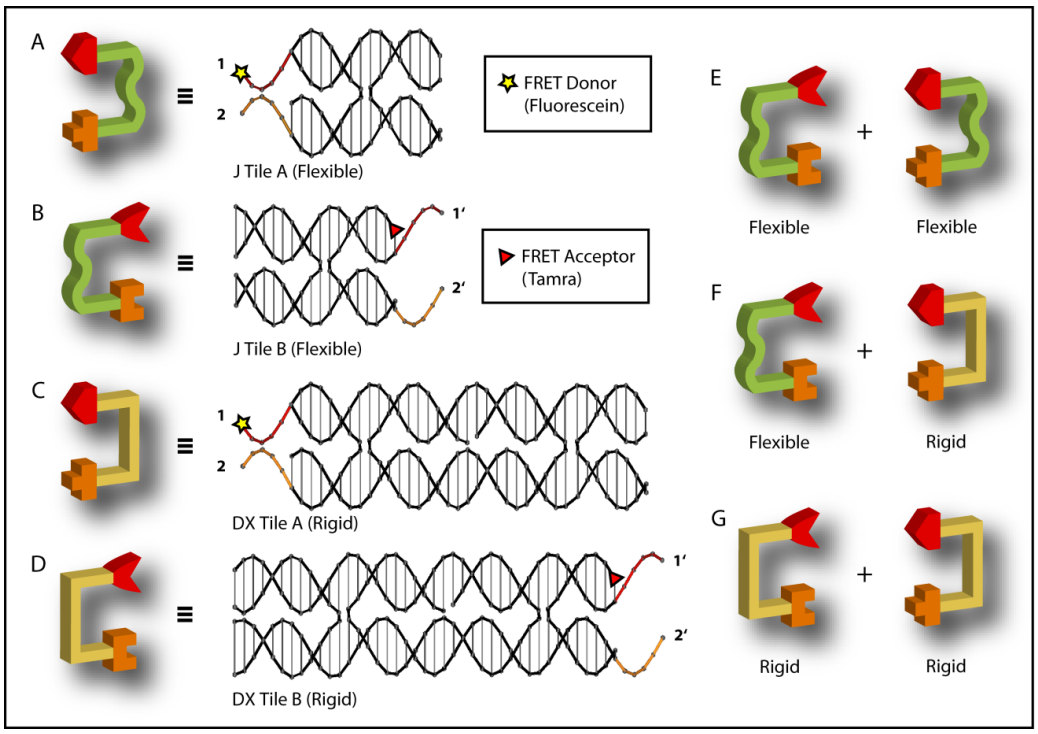

Figure 3.2. Schematic representation and helical structure of the J (flexible scaffold in green) and DX (rigid scaffold in yellow) tiles used in the study. FRET donor and acceptor fluorophores are shown as yellow stars (fluorescein) and red triangles (TAMRA), respectively. Two pairs of complementary sticky ends, 1/1′ and 2/2′ (shown as complementary shapes in the schematics), were added to the ends of the tiles to create a bivalent association between the scaffolds. (a) J-A (32 bp); (b) J-B (36 bp); (c) DX-A (74 bp); (d) DX-B (82 bp). The numbers mark the size of the hybridized domains in the tiles. For all dimers, the inter-tile junctions are separated by two full turns to ensure an in-plane dimer conformation. (e-g) The flexible, semi-rigid, and rigid dimers that contain J-A/J-B, J-A/DX-B, and DX-A/DX-B, respectively.

3.3 Results and Discussion

3.3.1. Real-Time Monitoring of Dimer Formation. For the FRET experiments, determination of the melting temperature of dimer complexes and extraction of thermodynamic parameters from thermal profiles has been previously detailed.[2, 24, 25] For each dimer assembly, two samples were prepared with identical experimental conditions: one sample contained a donor fluorophore (5′-fluorescein-labeled oligomer) in tile A and an acceptor fluorophore (5′-TAMRA-labeled oligomer) in tile B, while the second sample contained only the donor fluorophore in tile A and the corresponding unlabeled oligomer in tile B. Comparing the donor emission of these two samples yields the efficiency of energy transfer between the donor and acceptor. The inter-fluorophore distance (and therefore the FRET efficiency) changes as a result of temperature-dependent conformational changes, which directly reflects the assembly/disassembly process of the DNA tile dimers (the donor and acceptor pair has a Förster distance 4.8−5.0 nm). The fluorescence thermal curves were measured with a real-time PCR thermocycler: for cooling profiles, the samples were held at a high temperature (80 °C), and the fluorescent emission of the donor at 522 nm (excited at 492 nm) was monitored while the temperature was decreased to 25 °C, with a gradient of −0.1 °C/min. Heating profiles were similarly collected, and all experiments were repeated at least twice in triplicate to ensure reproducibility.

A comprehensive description of FRET data processing can be found in Appendix B. Briefly, for each dimer assembly: (1) The efficiency of energy transfer (E) is determined at each temperature on the basis of the intensity of

donor/acceptor (I^{DA}) and donor-only (I^{D}) samples (typical results shown in Figure 3.3a) (2) E is subsequently related to the fraction of assembled dimer structures (θ) by normalizing the FRET efficiencies as a function of temperature. θ is plotted against temperature with heating and cooling profiles superimposed (Figure 3.3b). It is important to note that negligible hysteresis was observed for all dimer assemblies, especially for the normalized data, indicating the reversibility of the dimer formation and dissociation processes and thermal equilibrium at each temperature. (3) The melting temperature (Tm) is obtained by fitting the first derivative of θ versus temperature with a Gaussian function and identifying the midpoint of the transition (Figure 3.3c). (4) As each of the dimer assemblies demonstrated a reversible thermal transition, it can be assumed that the system reached equilibrium at each temperature, allowing application of the van't Hoff law where the variation of the equilibrium constant (K_{eq}) with temperature is used to obtain the enthalpy (ΔH) and entropy changes (ΔS) of the complex formation. K_{eq} of dimer formation is expressed as a function of θ at equilibrium, based on a bi-molecular reaction scheme. Plots of $\ln K_{eq}$ vs 1/T in the temperature range of the transitions were linear, indicating that ΔH and ΔS are temperature independent (Figure 3.3d). (5) Finally, the van't Hoff enthalpy and entropy changes for the reversible thermal transitions allow the calculation of the free energy change (ΔG) for the assembly process using the Gibbs equation.

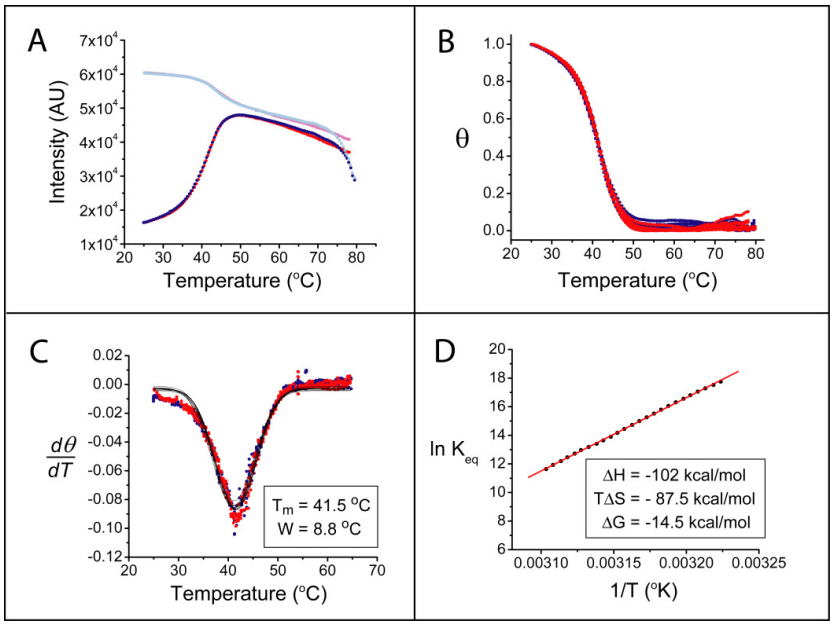

Figure 3.3. Illustration of FRET data analysis for a typical sample (DX-A/DX-B homo-dimer). (a) The raw data (fluorescence intensity versus temperature) were collected by a RT-PCR thermocycler. The heating and cooling curves for the donor/acceptor sample are shown in red and blue, respectively, and the heating and cooling curves for the donor-only sample are shown in magenta and cyan, respectively. (b) Plot of normalized FRET efficiency or fraction of dimer formation, θ, as a function of temperature. Multiple thermal profiles (heating cycles shown in red and cooling cycles shown in blue) are plotted together (six replicate profiles), exhibiting the negligible hysteresis and high reproducibility of the data. A single thermal transition at ~41.5 °C is observed. (c) First derivatives of the profiles in panel B, dθ/dT, are plotted versus temperature (dots), and a Gaussian fit (solid line) yields the melting temperature (41.5 °C) and the width of the transition (8.8 °C). (d) The linear fit of a corresponding van't Hoff plot

generates the changes of enthalpy (ΔH) and entropy ($T\Delta S$), and thereby the free energy changes (ΔG).

The results of the FRET data analysis for each of the dimer designs illustrated in Figure 3.2e-3.2g are listed in Table 3.1.

	Tm (°C)	W/2 (°C)	Δ H (kcal/mol)	Δ S (kcal/mol*K)	TΔS (kcal/mol)	Δ G (kcal/mol)
Flexible Dimer	31.0 ± 0.6	4.3	-123.2 ± 9.1	-0.373 ± 0.030	-113.3 ± 9.1	-11.9 ± 0.1
Semi-rigid Dimer	36.2 ± 0.6	4.8	-106.8 ± 3.9	-0.314 ± 0.012	-93.5 ± 3.7	-13.3 ± 0.2
Rigid Dimer	41.4 ± 0.2	4.3	-102.0 ± 1.4	-0.293 ± 0.004	-87.5 ± 1.3	-14.5 ± 0.1

Table 3.1. Melting Temperature and Thermodynamic Characterization of Dimers Composed of Bivalent Monomer Scaffolds (J and DX) with Variable Conformational Flexibility. The structures of the monomer units are shown in Figure 3.2. The values listed are the mean and standard deviation of measurements from multiple thermal profiles (six independent samples, with analysis of the heating and cooling cycle for each). *W*/2 indicates the half-width of the Gaussian fit, representing the width of the thermal transition (Figure 3.3c). The temperature used to calculate $T\Delta S$ and ΔG is 25 °C. The concentration of the individual tiles in each sample is 0.3 μM. The details of data analysis are described in Appendix B.

Examination of the experimental results reveals that subtle changes in the conformational flexibility of the bivalent monomer scaffolds lead to significant differences in the thermal stability of the dimer superstructures. The melting temperature was the highest, 41 °C, for dimers composed of two rigid scaffolds (DX/DX homo-dimer) and the lowest, 31 °C, when both scaffolds were flexible (J/J homo-dimer). The 10 °C difference in the melting temperatures of these two DNA tile dimers is rather remarkable considering that both dimer structures have identical sticky end sequences. The semi-rigid (J/DX hetero-dimer) construct had a melting temperature of 36 °C, the mid-point between the flexible and rigid dimers.

The change in free energy reflected the same trend: the rigid dimer requires the smallest conformational change of each monomer unit, and thus it shows the most favorable binding, with the most negative ΔG. Interestingly, introducing flexibility into the scaffold significantly affects the changes in both the enthalpy and entropy of the corresponding dimerization reaction. For example, comparing the semi-rigid and rigid dimers, ΔG for the semi-rigid dimer formation is 1.2 kcal/mol less negative than that of the rigid dimer, which can be translated to an 10-fold reduction of the equilibrium constant at room temperature. This difference in ΔG is mostly the result of a more negative TΔS, originating from the larger entropic cost to form a J/DX tile compared to a rigid DX/DX dimer. On the other hand, for a flexible J/J dimer, its formation significantly restricts the range of branch angles that are available to the J monomers and carries a corresponding entropic penalty. It should be noted that both the ΔH and TΔS values for the

flexible dimer are significantly more negative than those for the rigid dimer (with TΔS exhibiting a larger difference). This result indicates that the association of two flexible tiles involves a more favorable enthalpic gain. This may be because the junction flexibility permits enhanced hydrogen-bonding interactions and more favorable base stacking between the sticky ends and their flanking base pairs, thus resulting in reduced energetic strain within the helical arms in the final dimer assembly. However, this enthalpic gain is completely offset by an even greater entropic loss because the conformations available to both monomeric units are largely restricted upon dimer formation. Overall, the thermodynamic effects result in a flexible dimer that is less thermally stable than the corresponding rigid dimer.

3.3.2. Competitive Displacement Reactions. The relative stability of the dimers was further demonstrated through competition assays, and the results were visualized using polyacrylamide gel electrophoresis (PAGE). Figure 3.4 illustrates the three competitive displacement reactions that were performed, each involving the addition of an increasing amount of secondary tile to a pre-assembled dimer.

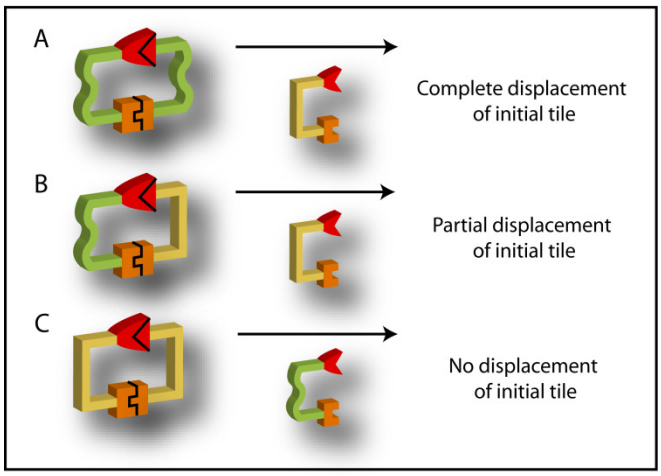

Figure 3.4. Schematic representation of the competitive displacement reactions. Each tile of the initial dimer is present at equimolar concentration and labeled with a fluorescent dye. The unlabeled secondary tiles are added in a range of relative concentrations, from submolar to excess compared to the initial tiles. (a) Rigid DX tile is added to pre-assembled flexible J/J dimer. (b) Rigid DX tile is added to pre-assembled semi-rigid J/DX tile. (c) Flexible J tile is added to pre-assembled rigid DX/DX dimer.

Three possible outcomes of the displacement reactions are predicted on the basis of the relative thermal stability of the corresponding dimers: complete, partial, or no exchange of one tile in the initial dimer by the secondary tile. For the case in which the initial dimer is relatively less stable than the replacement dimer, as applies to the schemes shown in Figure 3.4a and 3.4b, quantitative displacement should be observed. For the case in which the initial dimer is relatively more stable, as shown in Figure 3.4c, minimal formation of the replacement dimers would be detected, even with a large excess of the secondary tile present.

To make identification of the gel bands corresponding to each individual tile and the assembled dimers possible, the tiles in the initial dimers were labeled with two fluorescent dyes, fluorescein and TAMRA. The dyes were placed at positions away from the intermolecular, sticky-end binding sites (different from those used in the FRET experiment with inter-dye distances a minimum 10 nm in the dimer) to minimize energy transfer between the fluorophores, so that the intensities of the fluorescent bands measured from the gel images provide a semi-quantitative measure of the concentration of the species they represent. In addition, the tiles (secondary) that were added to the pre-assembled dimers contained no dye label, so that both a color change and a gel shift are expected if any exchange reaction occurs. Multicolor gel images were generated by superimposing the fluorescent intensity of the green (fluorescein) and red (TAMRA) channels (collected with a Typhoon Trio gel imaging system).

The results of the competitive displacement experiments are in agreement with the predictions based on the FRET study. Figure 3.5 shows typical PAGE results for the reactions represented in Figure 3.4 (additional gel images are shown in Appendix B).

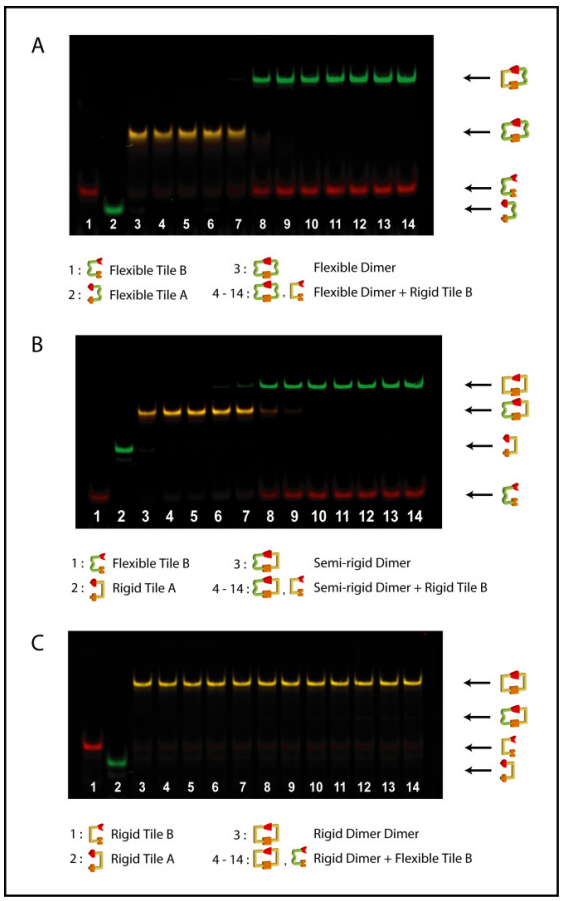

Figure 3.5. Polyacrylamide gel analysis of the reaction schemes shown in Figure 3.4, at 20 °C. The gel images represent overlay of both green and red fluorescent channels. (a) Rigid DX tile added to pre-assembled flexible J/J dimer. (b) Rigid DX tile added to pre-assembled semi-rigid J/DX tile. (c) Flexible J tile added to pre-assembled rigid DX/DX dimer. Lanes 4–14 represent an increasing amount of secondary tile, with the molar ratio to the initial dimer ranging from 0.1:1 to 5:1. The amount of secondary tile (compared to 1× initial dimer) is indicated above the top band in each gel. The displacement reactions for all three cases were allowed to proceed for 2 h before loading onto the gel for analysis. Additional

gels for each reaction at various temperatures and different reaction times are included in Appendix B.

For each gel, lanes 1−3 contain the individual monomer units and their pre-formed 1:1 dimers, respectively. In addition to confirming the formation of each individual tile and the initial dimer, these bands (which have a unique size and fluorescent label) also serve as markers that help to determine the identity of each band in the remaining lanes. Lanes 4−14 correspond to the displacement reactions that contain the initial dimer with increasing amounts of secondary tile. The presence and relative concentrations of all species in the gels before and after the replacement reaction can be determined by measuring the fluorescent intensity of the corresponding bands.

The gel image in Figure 3.5a shows the equilibrium shift when the pre-formed J-A/J-B homo-dimer was mixed with increasing amounts of DX-B secondary tile. The displacement of J-B in the initial dimer by DX-B to form a J-A/DX-B hetero-dimer is readily observed, as evidenced by the disappearance of the middle yellow J-A/J-B dimer band, the simultaneous appearance of a lower red band (displaced J-B), and the appearance of an upper green band (the newly formed J-A/DX-B dimer). Note that the secondary DX-B tile is unlabeled, and the newly formed dimer contains only the green fluorescent label on J-A. The pattern of intensity changes that occur for each of the various bands supports the prediction of a quantitative displacement reaction, confirming that the semi-rigid J/DX dimer is thermodynamically more favored than the flexible J/J dimer.

Similarly, the PAGE result shown in Figure 3.5b that corresponds to the reaction of pre-assembled J-B/DX-A dimer with DX-B as the secondary tile revealed that the favored reaction product is the rigid DX/DX dimer, with quantitative displacement of J-B in the dimer by DX-B. However, the PAGE result in Figure 3.5c, corresponding to the reaction of initial DX/DX dimer with J-B as the secondary tile, showed that the dominant species in each reaction mixture was the initial, rigid DX/DX dimer, with little replacement of DX-B by J-B, even with a 5X molar excess of the secondary J tile. Collectively, the PAGE experiments support the conclusions drawn from the FRET experiments: dimers composed of two rigid tiles are more stable than those composed of one rigid and one flexible tile, and dimers composed of two flexible tiles are the least favored.

For each dimer, the entropy change of formation is fairly negative (see Table 3.1), so the relative equilibrium of the dimers is expected to change with temperature. For example, compared to the J/DX dimer, formation of the J/J dimer involves a more negative entropy change, implying that the J/J dimer should exhibit a greater increase in equilibrium binding constant at lower temperatures. The ratio of the J/DX dimer equilibrium constant to that of the J/J dimer is 1 at 5 °C, compared to 5 at 20 °C. Indeed, gel results reflect the temperature dependence of the equilibrium constants: for displacement reactions carried out at temperatures ranging from 5 to 20 °C, only partial exchange was observed at lower temperatures. At 5 °C, 30% of the initial J/J dimer (yellow band) remained, even with an excess of DX secondary tile compared to the J/J dimer, in contrast to the 20 °C reaction, in which this band completely

disappeared. The same trend was observed for the J/DX displacement reaction (DX secondary tile), in which the ratio of the DX/DX dimer equilibrium constant to that of J/DX dimer is expected to change from 10 at 20 °C to 6 at 5 °C. Collectively, the results of the gel assays for all three displacement reactions are in agreement with the thermodynamic data obtained by the FRET experiments.

3.3.3. Tiles with Variable Flexibility. To further study how the flexibility of a bivalent scaffold affects its association, two additional series of modified J tiles (in which the flexibility of the tiles were finely tuned) were constructed. The modified tiles were designed to form homo-dimers, and FRET analyses revealed an intriguing detail: the enthalpy and entropy changes associated with dimerization have partly compensating effects on strength of binding. In addition, the thermodynamics of polyvalent dimer formation clearly reflects the flexibility of the monomeric components.

The first series of modified J tiles, referred to as mesojunction tiles (Figure 3.6a), are similar to J tiles but have two individual crossovers at separate positions between the two helical domains rather than a single reciprocal crossover, and this structural feature is expected to result in an overall increase in the conformational flexibility of the scaffold.[26, 27] One of the strands that connect the two helical domains contains a variable number of thymine nucleotides (2T, 4T, or 6T), forming a single-stranded loop (shown in blue in Figure 3.6a) on the opposite side as the sticky ends (shown in red/orange). Among this series, the structure of the 2T mesojunction tile is expected to be the most constrained, while the 6T mesojunction tile should be the most flexible.

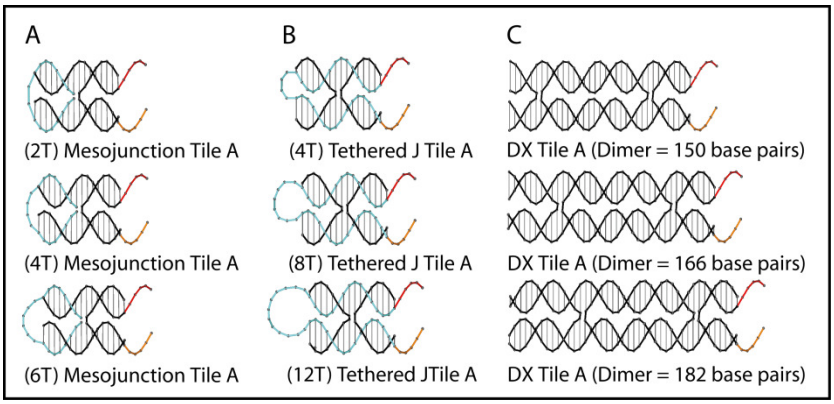

Figure 3.6. Helical structure of modified J tiles of varying flexibility and DX tiles of various size. (a) Series of mesojunction tiles. To further tune the flexibility, the arms of the tile were constrained by varying the number of thymines (T) within one of the crossover strands (shown in blue), forming a single-stranded loop of 2, 4, or 6T's. Note that the helical domains are not connected by a reciprocal crossover, as in a J tile, but are connected by two separate single-stranded crossovers. The blue strand has a nick at the junction position. (b) Series of tethered J tiles. For this series, the helical domains of each tile are connected by a reciprocal crossover, the same as in the unmodified J tiles. To reduce the flexibility of the scaffold, the two strands of the tile that do not participate in the crossover are connected by a short loop of 4, 8, or 12 T's, respectively, shown in blue. (c) Series of DX-A tiles of various sizes: 70, 78, and 86 bp, respectively. Binding of the DX-A tiles to their corresponding DX-B tiles results in 150, 166, and 182 bp homodimers.

As shown in Table 3.2, all three mesojunction tile dimers have nearly the same melting temperature (Tm) and free energy change (ΔG), with values of 30 °C and −12 kcal/mol, respectively, which are very similar to those of the flexible J/J dimer. These results suggest that the mesojunction dimers have a thermal stability comparable to that of the J/J dimers, and the addition of multiple T's within each mesojunction tiles does not significantly affect their formation or participation in a dimer superstructure. However, the decrease in tile flexibility as the number of T's is reduced results in considerable differences in the enthalpy (ΔH) and entropy (ΔS) changes associated with dimer formation. The ΔH values for mesojunction dimer formation exhibit a clear trend (2T > 4T > 6T), becoming more negative as the loop size is increased; ΔS follows the same pattern. Meanwhile, all the mesojunction dimers have comparable ΔG of formation. This indicates that, while increasing the conformational flexibility of the participating scaffolds (with longer T loop) increases the entropic cost of dimer association, the same flexibility results in a more favorable gain in enthalpy, and these two effects are compensating, resulting in a similar thermal stability for all of the mesojunction dimers at room temperature. Compared to the unmodified, flexible J/J dimer, the ΔH values for mesojunction dimers are significantly more negative (more favorable), and the ΔS values are also more negative (less favorable). The mesojunction tiles are the only series of tiles that do not have a reciprocal crossover at the junction, resulting in a significant increase in the freedom of motion around the junction point. This freedom may interfere with the base stacking of nucleotides flanking the junction in unbound tiles. Dimerization of the

mesojunction tiles will constrain the junction and improve the base stacking for both tiles involved, thus resulting in a much more favorable change in enthalpy upon binding as compared to the other tile dimers. An approximate calculation indicates that 2–4 additional base-stacking interactions can account for the more negative ΔH for mesojunction dimer formation than for the J/J dimer.

	Tm (°C)	W/2 (°C)	Δ H (kcal/mol)	Δ S (kcal/mol*K)	TΔS (kcal/mol)	Δ G (kcal/mol)
(2T) Mesojunction Dimer	29.1 ± 0.3	2.8	-140.5 ± 6.6	-0.433 ± 0.022	-129.2 ± 6.5	-11.3 ± 0.1
(4T) Mesojunction Dimer	30.6 ± 0.5	2.6	-169.2 ± 5.6	-0.526 ± 0.019	-156.8 ± 5.6	-12.4 ± 0.3
(6T) Mesojunction Dimer	30.7 ± 0.2	2.6	-180.4 ± 9.7	-0.563 ± 0.032	-167.8 ± 9.6	-12.6 ± 0.2
(4T) Tethered J Dimer	35.4 ± 0.2	4.5	-108.2 ± 1.8	-0.320 ± 0.006	-95.3 ± 1.7	-12.9 ± 0.1
(8T) Tethered J Dimer	36.0 ± 0.8	4.4	-105.1 ± 3.0	-0.309 ± 0.010	-92.1 ± 2.9	-13.0 ± 0.2
(12T) Tethered J Dimer	34.3 ± 0.4	4.4	-103.0 ± 2.9	-0.303 ± 0.010	-90.4 ± 2.8	-12.6 ± 0.2
Rigid Dimer (182 bp)	41.4 ± 0.3	4.5	-99.7 ± 1.2	-0.286 ± 0.004	-85.3 ± 1.2	-14.4 ± 0.1
Rigid Dimer (166 bp)	41.4 ± 0.2	4.3	-102.0 ± 1.4	-0.293 ± 0.004	-87.5 ± 1.3	-14.5 ± 0.1
Rigid Dimer (150 bp)	41.5 ± 0.1	4.1	-104.2 ± 0.4	-0.300 ± 0.001	-89.6 ± 0.3	-14.6 ± 0.1

Table 3.2. Melting temperature and thermodynamic characterization of dimers composed of bivalent monomer scaffolds (modified J and DX) with variable conformational flexibility and size. The structures of the monomer units are shown in Figure 3.6. The values listed are the mean and standard deviation of measurements from multiple thermal profiles (three independent samples, with analysis of the heating and cooling cycle for each). *W*/2 indicates the half-width of the Gaussian fit, representing the width of the thermal transition (Figure 3.3c). The temperature used to calculate $T\Delta S$ and ΔG is 25 °C. The concentration of the individual tiles in each sample is 0.3 μM. The details of data analysis are described in Appendix B.

The second series of the modified J tiles are referred to as tethered J tiles (Figure 3.6b), and like J tiles, they consist of four strands of DNA with a reciprocal crossover between the double-helical domains. However, the two strands that do not participate in the crossover are linked by a short loop of thymines (shown in blue in Figure 3.6b), ranging from 4T to 12T. Compared to unmodified J tiles, the entire series of tethered J tiles should be more constrained, with the tethered loop preventing free movement about the junction point.

The results of the FRET experiments reveal that the thermal stabilities of homo-dimers formed from the tethered tile series are similar to that of the semi-rigid J/DX hetero-dimer, with melting temperatures of 35, 36, and 34 °C for 4T, 8T, and 12T tiles, respectively. The ΔG values for this series of tiles also mirror that of the J/DX hetero-dimer, −13 kcal/mol. Interestingly, varying the number of T's that connect the two helical arms of the tiles does not result in significant differences in ΔH and ΔS. The range of ΔH, from −108 kcal/mol for the 4T tile dimer to −103 kcal/mol for the 12T tile dimer, is about the same as for the semi-rigid hetero-dimer (−107 kcal/mol). Similarly, $T\Delta S$ varies from −95 kcal/mol for the 4T tile dimer to −90 kcal/mol for the 12T tile dimer, also about the same range as fpr the J/DX hetero-dimer (−94 kcal/mol). Overall, the entire series of tethered J tiles behave as relatively rigid scaffolds, and it seems that increasing the number of T's in the tether loop from 4 to 12 does not effectively relieve the constraint.

Finally, to determine if variations in size (not only flexibility) would impact the binding affinities of the DNA tile scaffolds, several sizes of DX/DX dimers (150, 166, and 182 bp) were evaluated (Figure 3.6c). The experimental

data (Table 3.2) suggest that the size of the scaffold has very little effect on the thermal stability of the resulting dimers, as the melting temperature and ΔG values for all three DX/DX dimers were approximately equal. The ΔH and TΔS values of the smallest and largest dimers varied by less than 5 kcal/mol (demonstrating a small but notable dependence on size), again compensating for each other and yielding similar ΔG values. The sole difference in the three tiles is on the side opposite the sticky ends (the DNA strand sequence and length of all common regions are identical). One possible explanation for the observed difference in ΔH and ΔS is that stabilization in the central, sticky-end region of the dimer may propagate throughout the complex, further improving base stacking in the periphery. It seems that the more extended (larger) the tile is, the less susceptible it is to long-range stabilization. However, size-dependent effects cannot account for the ΔH and ΔS differences observed in the other experiments. The results suggest that the variation in the thermal stabilities of the other dimer assemblies is the product of differences in the conformational flexibility of the DNA scaffolds, and not merely a consequence of component tile size.

3.4. Materials and Methods

See APPENDIX B

3.5. Conclusions

It is generally accepted that the flexibility of a DNA nanoscaffold is related to the number of connections between helical domains, with the least rigid structures formed from the fewest number of crossovers. Besides the number of crossovers, the structure of the connection points influences the overall flexibility

of the tile; e.g., compared to single crossovers, reciprocal crossovers are more rigid. It is also evident that appropriate use of thymine tethers can restrict the motion of the junction points, thereby reducing the conformational flexibility of the tiles. With these design parameters in mind, a collection of DNA tiles were constructed to characterize the influence of conformational flexibility on multivalent scaffold binding.

The most significant insights gained by this multivalent binding study are illustrated in Figure 3.7. First, increasing the conformational flexibility of a bivalent scaffold increases the entropic cost of association; however, the same flexibility results in a more favorable enthalpy of binding. This can be understood in the following way: imposing order on a flexible object through a binding event will carry an entropic penalty; on the other hand, adequate flexibility increases the likelihood that all ligand–receptor interactions can occur without energetic strain. Second, the overall thermal stability of bivalently linked scaffolds is highest when both scaffold components are rigid and lowest when both scaffolds are flexible. This observation indicates that reducing the entropic cost of association plays an important role in increasing the overall thermal stability.

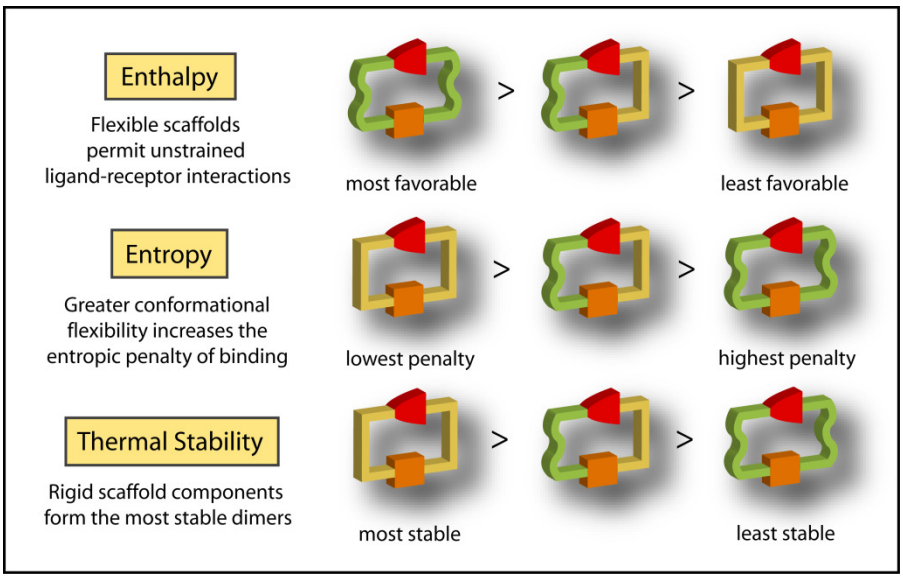

Figure 3.7. Result summary: the conformational flexibility of two scaffolds linked by bivalent associations affects the enthalpy, entropy, and thermal stability of their binding.

This study demonstrates how precisely engineered DNA nanostructures can be used to probe very subtle biophysical phenomena, including the effect of scaffold flexibility on the binding of a multivalent molecule. The use of DNA nanostructures as models of polyvalent binding has made it possible to quantify the compensating effects of enthalpy and entropy, which is a notoriously difficult relationship to characterize. This technique may be used to generate valuable structural and functional characterizations and may have applications in various research fields, such as polyvalent inhibitor drug discovery and the study of spatially controlled chemical reactions.

3.6. References

(1) Mammen, M.; Choi, S. K.; Whitesides, G. M. *Angew. Chem. Int. Ed.* **1998**, *37*, 2754– 2794.

(2) Nangreave, J.; Yan, H.; Liu, Y. *Biophys. J.* **2009**, *97*, 563– 571.

(3) Seeman, N. C. *J. Theor. Biol.* **1982**, *99*, 237– 247.

(4) Seeman, N. C.; Kallenbach, N. R. *Biophys. J.* **1983**, *44*, 201– 209.

(5) Kallenbach, N. R.; Ma, R. I.; Seeman, N. C. *Nature* **1983**, *305*, 829– 831.

(6) Marky, L. A.; Kallenbach, N. R.; McDonough, K. A.; Seeman, N. C.; Breslauer, K. J. *Biopolymers* **1987**, *26*, 1621– 1634.

(7) Cooper, J. P.; Hagerman, P. J. *J. Mol. Biol.* **1987**, *198*, 711– 719.

(8) Churchill, M. E. A.; Tullius, T. D.; Kallenbach, N. R.; Seeman, N. C. *Proc. Natl. Acad. Sci. U.S.A.* **1988**, *85*, 4653– 4656.

(9) Duckett, D. R.; Murchie, A. I. H.; Diekmann, S.; von Kitzing, E.; Kemper, B.; Lilley, D. M. J. *Cell* **1988**, *55*, 79– 89.

(10) Cooper, J. P.; Hagerman, P. J. *Proc. Natl. Acad. Sci. U.S.A.* **1989**, *86*, 7336– 7340.

(11) Murchie, A. I. H.; Clegg, R. M.; von Kitzing, E.; Duckett, D. R.; Diekmann, S.; Lilley, D. M. J. *Nature* **1989**, *341*, 763– 766.

(12) Lu, M.; Guo, Q.; Marky, L. A.; Seeman, N. C.; Kallenbach, N. R. *J. Mol. Biol.* **1992**, *223*, 781– 789.

(13) Mao, C.; Sun, W.; Seeman, N. C. *J. Am. Chem. Soc.* **1999**, *121*, 5437– 5443.

(14) Fu, T. J.; Seeman, N. C. *Biochemistry* **1993**, *32*, 3211– 3220.

(15) Winfree, E.; Liu, F.; Wenzler, L. A.; Seeman, N. C. *Nature* **1998**, *394*, 539– 544.

(16) Miick, S. M.; Fee, R. S.; Millar, D. P.; Chazin, W. J. *Proc. Natl. Acad. Sci. U.S.A.* **1997**, *94*, 9080– 9084.

(17) McKinney, S. A.; Declais, A.-C.; Lilley, D. M. J.; Ha, T. *Nat. Struct. Biol.* **2002**, *10*, 93– 97.

(18) Altona, C. *J. Mol. Biol.* **1996**, *263*, 568– 581.

(19) Petrillo, M. L.; Newton, C. J.; Cunningham, R. P. *Biopolymers* **1988**, *27*, 1337– 1352.

(20) Li, X.; Yang, X.; Qi, J.; Seeman, N. C. *J. Am. Chem. Soc.* **1996**, *118*, 6131– 6140.

(21) Sa-Ardyen, P.; Vologodskii, A. V.; Seeman, N. C. *Biophys. J.* **2003**, *84*, 3829– 3837.

(22) von Kitzing, E.; Lilley, D. M. J.; Diekmann, S. *Nucleic Acids Res.* **1990**, *18*, 2671– 2683.

(23) Eis, P. S.; Millar, D. P. *Biochemistry* **1993**, *32*, 13852– 13860.

(24) Sacca, B.; Meyer, R.; Feldkamp, U.; Schroeder, H.; Niemeyer, C. M. *Angew. Chem. Int. Ed.* **2008**, *47*, 2135– 2137.

(25) Sacca, B.; Meyer, R.; Niemeyer, C. M. *Nat. Protoc.* **2009**, *4*, 271– 285.

(26) Du, S. M.; Zhang, S.; Seeman, N. C. *Biochemistry* **1991**, *31*, 10955– 10963.

(27) Wang, H.; Seeman, N. C. *Biochemistry* **1995**, *34*, 920– 929.

Chapter 4

Steric Crowding and the Kinetics of DNA Hybridization in a DNA Nanostructure System

Used with permission from Vidal Pinheiro, A.; Nangreave, J.; Yan, H.; Liu, Y.: Steric crowding and the kinetics of DNA hybridization in a DNA nanostructure system, submitted to *J. Am. Chem. Soc.,* **2011**.

4.1. Abstract

The ability to generate precisely designed molecular networks and modulate the surrounding environment is of paramount importance for fundamental studies of chemical reactions. DNA nanotechnology simultaneously affords versatility and modularity for the construction of tailored, nanoscale molecular environments. In this work, we systematically isolate and study the effects of steric crowding corresponding to the hybridization of a 20-nt single strand of DNA to a 6-helix tile, where the number and character of the surrounding strands influence the molecular environment of the hybridization site. It was observed that both the location of the hybridization site along the tile, and the presence of flanking strands modestly decrease the hybridization rate constant. Further, the presence of secondary structures within the hybridization site dramatically reduces the reaction kinetics. We propose that the observed changes in the hybridization rate constants are related to the probability of nucleation of the invading single stranded DNA, determined solely by steric hindrance.

4.2. Introduction

Acquiring a fundamental understanding of the local aspects of chemical reactions and how complex molecular environments affect reaction kinetics is of great interest both to basic science and for technological applications. For example, the ultra-efficient electron transfer present in photosynthetic systems is due to the precise arrangement of various protein and chromophore components, and the heterogeneous catalytic reactions widely used in the chemical industry are characterized by large surface areas and very specific micro-environments. However, among the tools and approaches chemists have at their disposal to modulate molecular surroundings for the study of chemical reactions, few offer the combination of spatial accuracy and versatility.

In recent years, the use of DNA nanostructures has become an attractive method of organizing matter at the molecular level, due to the reliability of base-pair interactions, improved DNA manipulation techniques, and easy and affordable custom oligonucleotide synthesis. Structural DNA nanotechnology allows the construction of discrete, nanometer sized structures in a variety of shapes and designs, with incredibly high assembly yields[1-4]. It is now possible to control not only the relative position of two molecules, but also the number and spacing of surrounding molecular interactions. This is a valuable tool for the study of how molecular environment influences the kinetics of chemical reactions.

As new DNA nanostructure design strategies have evolved that support enhanced structural complexity and function, interest in dynamic structures has

grown[5,6]. The next generation of dynamic DNA assemblies interacts with the surrounding environment, responds to external stimuli with concomitant state changes, and even actuates according to programmed responses. There are several examples of elegant 'proof-of-concept' structures, including reconfigurable topological structures[7], a wire-frame tetrahedron with controllable dimensions[8], nano-tubes for the controlled release of gold nanoparticles[9] and DNA walkers[10-12]. Also, the development of DNA computing[13-16] enables researchers to embed the path to a desired end state within the DNA nanostructures themselves, with an external input triggering an automatic system response. Understanding how individual molecular components interact with one another, both in terms of their spatial arrangement and temporal interaction within the DNA architectures is of paramount importance, and may lead to development of new and improved design rules and active motifs for the construction of dynamic DNA structures.

Independent of the external trigger, the fate of dynamic structures is governed by the kinetics of the hybridization process that occurs between interacting DNA strands[17-19]. Many strategies can be used to modulate the changes of state, thereby determining the overall arrangement of the system components at any given moment, including strand displacement, multimerization of monomeric units, binding and release of protein-aptamer complexes, interaction with DNA binding proteins or small molecules (hormones, ATP, lipids, etc.), cross-linking through photonic energy, secondary structure changes with varying pH, or interaction with other hetero-elements (such as single-wall carbon nanotubes or metal nanoparticles). Thus, the reliable modulation of

hybridization kinetics is extremely significant for the design and functionality of dynamic structures.

The thermodynamics and kinetics of nucleic acid hybridization have been thoroughly studied[20-27], but very few reports describe the behavior of any complex structures, involving more than two or three DNA strands. The thermodynamics of DNA tile dimerization has been investigated by our group[28,29] and others[24]. However, no systematic study of hybridization kinetics involving DNA nano-structures has been reported. Here, we examined several steric factors that affect the kinetics of hybridization of a single-stranded DNA target to a complementary single stranded probe extension of a rectangular six-helix DNA tile. The steric factors that were evaluated include: 1) the presence/absence of elements surrounding the hybridization site; 2) the position of the target probe relative to the complete tile; and 3) the presence of secondary structure formed between the target probe and other components of the tile. It is our aim to take the first step towards understanding the complexity of hybridization kinetics in higher-order DNA assemblies. This work might facilitate the development of new approaches to study the influence of molecular surroundings on chemical kinetics.

4.3 Results and Discussion

4.3.1. System Model and Measurement. We designed a model in which a 20 nucleotide (nt) long DNA Target strand hybridizes to a Target Probe (TP) displayed at specific positions on one side of a six-helix tile (6HX) (Figure 1). The design of the six-helix tile was adapted from previous reports[28,30], and consists of six parallel DNA double helices joined by oligonucleotides that cross-

over from one helix to adjacent helices. This arrangement of helices results in a planar, rectangular-shaped tile; the 14 constituent oligomers self-assemble into the desired tile when mixed together and annealed. The 3' termini of selected helices were extended by twenty nucleotides, generating single-stranded overhangs that were designated as Target Probe (TP) or Off-Target Probe (OTP) sequences. Target and Off-Target strands, each 20 nt long, were designed to be fully complementary to the Target- and Off-Target Probes, respectively. For all experiments, only one of the selected helices displayed the Target Probe, while the remaining five helices contained Off-Target probes. This design permits accurate control of the number of strands surrounding the site of hybridization, as well as the distance between the site and neighboring strands.

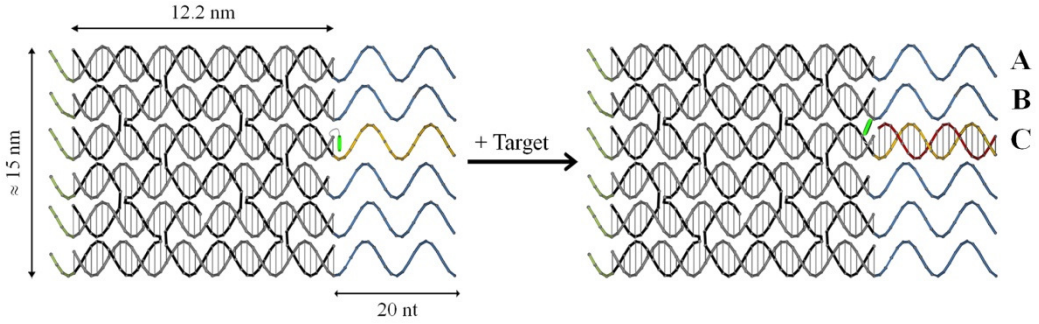

Figure 4.1. Detailed helical structure of the 6HX tile used in this study. The core section of the tile is shown in gray and black, with the strands that participate in crossovers between adjacent helices in black. The schematic shown here corresponds to the design in which the Target Probe (yellow), extended from the right side of the core on the third helix from the top (position C), is surrounded by single stranded Off Target Probe extensions (blue) at every other position. The covalently attached FAM dye reporter is shown in green, at the interface between the core and the Target Probe (at position C). Poly T extensions, at every helical position on the left side of the core, are shown in dark green. After the addition of the Target (red), the Target is hybridized to the Target Probe on helix three, forming a 20 bp duplex.

To determine the effect of steric accessibility of the binding site on the rate of hybridization, several degrees of 'crowding' of the Target Probe were evaluated. First, the positional dependence of the rate of hybridization was examined by measuring the hybridization kinetics when the same TP sequence was displayed from each of the three degenerate positions (Figure 4.1, outermost – position A, inner – position B, and innermost – position C, helices). The degree of accessibility of the binding site varies depending on the position of the TP with respect to the 6HX tile, presumably with the accessibility of the three positions decreasing as the TP moves inward (A>B>C). Second, the effect of steric crowding on the kinetics of hybridization was further evaluated by surrounding the TP site with single- and double-stranded DNA at the adjacent helixes (Figure 4.2). Three sets of experiments were performed to evaluate these effects (for all three sets of experiments, the TP was displayed from each of the three unique positions on the 6HX tile): [1] The TP was surrounded by blunt-ended helices, i.e. each of the five non-Target Probe helices did not contain an Off-Target Probe (Figure 4.2, left). This represents the least crowded scenario (Figure S1 in Appendix C); [2] The TP was crowded by single-stranded DNA at the surrounding positions (Figure 4.2, center). Each of the five non-Target Probe helices included a 20 nt poly(T) sequence (Figure S2 in Appendix C); [3] The TP was crowded by double-stranded DNA at the surrounding positions (Figure 4.2, right). Each of the five non-Target Probe helices contained a random, 20 nt sequence (Figure S3 in Appendix C). For [2], the use of a poly(T) sequence for the OTPs minimizes interactions between the OTPs and the TP and the Target

itself, which allows the steric effects on the rate of hybridization to be isolated from any sequence specific interactions. For [3], the fully complementary 20 nt Off-Target was pre-hybridized to the OTPs to form double-stranded extensions prior to any kinetic measurements, aiming to further increase the level of crowding of the TP (Figure S3 in Appendix C).

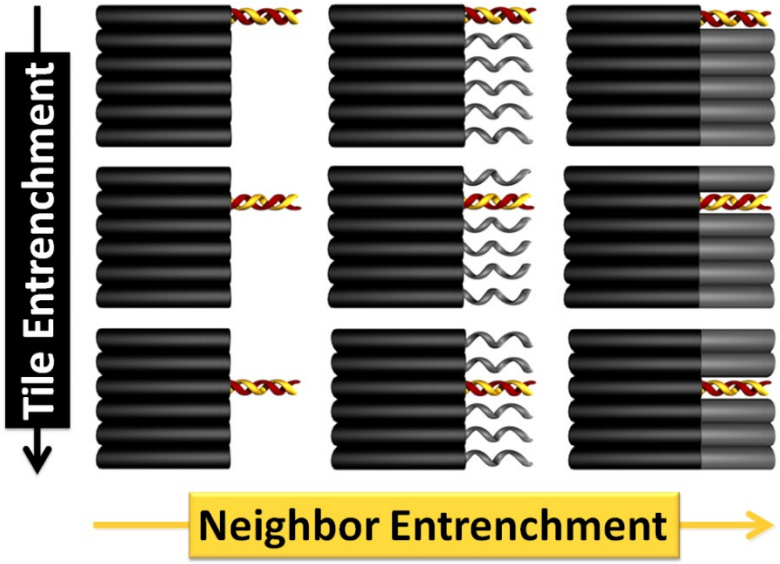

Figure 4.2. Schematic representation of the series of 6HX tile designs used to determine the effect of steric accessibility of the binding site on the rate of hybridization. From top to bottom, the site of Target hybridization is located at position A, B and C, respectively. From left to right, the site of Target hybridization is not surrounded by single or double stranded extensions, and crowded by single and double stranded DNA, respectively. Accessibility of the Target to the Target Probe is expected to become increasing restricted in the designs shown from top to bottom and from left to right.

Experiments were also designed to evaluate the influence of the secondary structure of the probes, and the interaction of the TP with other components of the tile, on the rate of Target hybridization. For these experiments, the TP was displayed from Position C (the innermost), while a single OTP with a specifically designed sequence (partially complementary to the TP) was displayed from the adjacent helix (Position B). The remaining four OTP positions were extended with 20 nt poly(T) sequences (Figures S4-S7 in Appendix C).

To suppress any non-specific base stacking interactions between the blunt ends of individual tiles that might affect the rate of diffusion and thus, the hybridization kinetics, four thymine nucleotides were extended from one strand in all helices on the side of the tile opposite to the binding domain. For the same reason, those experiments in which the TP was displayed without any surrounding single- or double-stranded DNA, three thymine nucleotides were extended from one strand in the five helices that did not contain the TP (on the same 'binding' side of the tile). Additional design, sequence, and experimental details can be found in Appendix C.

Electrophoretic analysis of equilibrium products was performed to determine the extent of the forward and reverse reactions. 6HX tile solutions were analyzed before and after the addition of the Target for every reported design. The gel results show that at equilibrium, nearly all of the unbound 6HX tile is consumed to produce a Tile/Target hybridized product (Appendix C). These results indicate that the reverse, denaturation reaction is negligible compared to

the forward, hybridization reaction, allowing application of the proposed kinetic analysis.

A covalently attached fluorophore (FAM) was incorporated at the interface between the core of the 6HX tile and the single-stranded TP extension (Figure 4.1), to serve as a reporter of the rate of hybridization of the Target strand. The fluorophore was placed at the three different helical positions (only one fluorophore per experiment), corresponding to the three positions of hybridization described above. The initial intent was to use Förster Resonance Energy Transfer (FRET) between a FAM/TAMRA pair, with a FAM-labeled tile and a TAMRA-labeled Target strand to monitor the hybridization event. However, considerable changes in the fluorescence quantum yields of both individual dyes, FAM and TAMRA, in the absence of the other dye, were observed upon hybridization. For FAM, a 30-40% increase in fluorescence quantum yield was detected upon hybridization of an unlabeled Target (Figure 4.3) to the FAM-labeled tile; and for TAMRA, a fluorescence quenching of ≈30% was observed upon hybridization of the TAMRA-labeled Target to the unlabeled tile (Figure S13 in Appendix C). These signal changes are opposite to the expected donor/acceptor emission changes that occur in FRET, compromising the reliability of the FRET method to monitor hybridization. However, for the FAM-labeled only samples, the fluorescence enhancement observed upon hybridization was investigated further to determine its reliability as a reporter of hybridization.

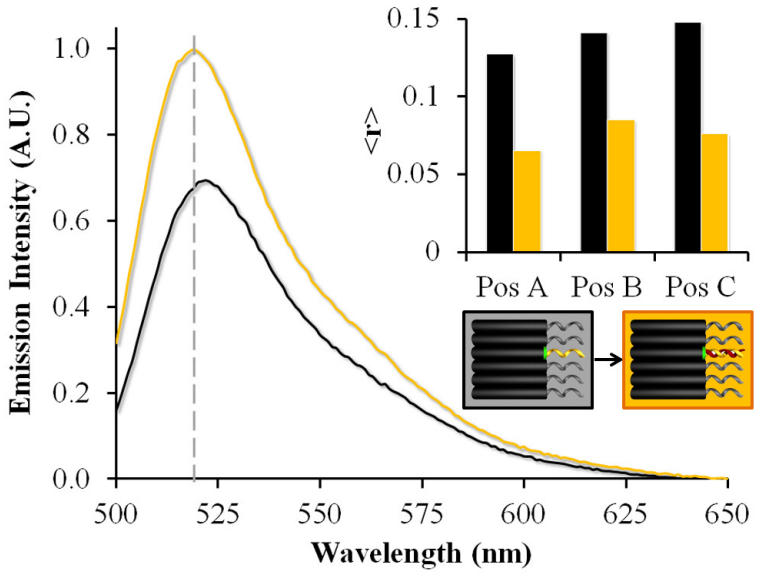

Figure 4.3. Fluorescence enhancement of the FAM reporter dye upon hybridization of the Target to the 6HX tile. The fluorescence emission spectrum of FAM was measured before (black trace) and after (yellow trace) the addition of Target to the 6HX tiles (the design corresponding to single stranded DNA extensions surrounding the Target Probe site located on helix 3). The spectra show an ≈30% increase in the fluorescence quantum yield of the dye after hybridization of the Target. The inset summarizes the results of steady-state fluorescence anisotropy measurements of the same system before (black bars) and after (yellow bars) the addition of Target. The anisotropy was independently measured for 6HX tiles with the Target Probe and the FAM reporter dye located at helical positions A-C. Before Target hybridization (black bars), high anisotropy values for all three designs (0.127-0.147) were observed, indicating the dye has impaired rotation during excited state deactivation. After Target hybridization

(yellow bars), the anisotropy values drop considerably (0.065-0.076) for all designs, demonstrating that the dye is experiencing a more unobstructed rotation.

The variations in FAM fluorescence that occur upon strand hybridization are the result of a combination of several, distinct photo-physical processes. The increase in fluorescence quantum yield and slight blue shift (2-4 nm) indicate that hybridization induces a change in the molecular environment of the fluorophore (Figure 4.3). Time-correlated fluorescence single photon counting (TCSPC) was employed to determine the fluorophore decay times and relative amplitudes, aiming to identify the population distribution of the dye subjected to different molecular environments. In the absence of the Target strand, the fluorescence decay was well fit by a bi-exponential law, with 4.4 ns (92%) and 1.7 ns (8%) components (Figure S17 in Appendix C). The 4.4 ns decay corresponds to the lifetime of free FAM dye in solution[31]. After an excess of Target strand was added, the decay was also fit by a bi-exponential law, but it was dominated by the slower 4.1 ns component (98%), and the amplitude of the 1.7 ns component was only ≈2% (Figure S17 in Appendix C). Thus, hybridization of the Target to the 6HX tile promotes the conversion of a short-lived FAM excited state population to a longer-lived state. No change in the extinction coefficients of absorption "before" and "after" Target addition was observed. Therefore, the increase in fluorescence quantum yield and decrease of the short lifetime component after hybridization can be explained by a decrease in the non-radiative decay rate constant of the dye. This may indicate that the dye is forced into a local environment with fewer quenching factors.

Steady-state fluorescence anisotropy measurements were performed (each of the three FAM positions on the 6HX tile were independently evaluated), before and after Target hybridization (inset Figure 4.3). High anisotropy values were observed before hybridization (0.127-0.147), when compared to linear DNA strands functionalized with fluorescein[32,33], demonstrating that the FAM dye experiences considerably restricted rotation during its excited state deactivation. The measured anisotropy decreased drastically after the addition of Target (0.065-0.076), signifying that the hybridization event leads to increased free rotation of the dye. Taken altogether, the results strongly suggest that before hybridization, a fraction of the FAM population is intercalated within the single stranded TP (or stacked with the adjacent base at the end of the DNA helix, Figure 4.1, left), where the dye is expected to have a highly restricted molecular rotation, leading to a high anisotropy value. Stacking of the fluorophore with adjacent bases also leads to a lower quantum yield and a faster decay, indicating an excited state quenching process, likely the result of photo-induced electron-transfer from FAM to the adenine bases flanking the dye as was observed in simpler systems[31,34]. The higher conformational stringency of the DNA nano-structure is likely to enhance the effect of photo-induced electron transfer, more commonly observed when guanine bases are in the vicinity of the FAM dye[35,36]. Upon Target hybridization, the formation of a double helix displaces the dye from its intercalated state, reducing the interaction with the TP (Figure 4.1, right). This view is supported by the drastically decreased anisotropy, increased emission yield, and increased (up to 98%) amplitude of the longer life time component of the decay.

It was necessary to determine if the observed increase in quantum yield is *site-specific*, i.e., if an increase in FAM emission is only observed when Target hybridization occurs at the same tile position. Six unique 6HX tiles were designed, all with the FAM dye located at Position C. For each tile, one of the six helices displayed the TP and the remaining five helices presented OTPs. The steady-state fluorescence emissions of each unique tile were independently measured before and after the addition of Target (Figure 4.4). The enhancement in fluorescence was only observed when the Target hybridized to Position C, which contained the reporter dye. Similar results were obtained for tiles with FAM labels at positions A and B. Therefore, the fluorescence change of the FAM dye upon DNA hybridization has exclusive site-specificity. This is presumably because the displacement of the dye from an intercalated state to a more freely rotating state involves a very specific change in the local environment of the dye. The single dye approach presented here offers an advantage over the FRET approach because it allows the addition of a large excess of unlabeled Target strand that simplifies the reaction rate determination, which would otherwise be unfeasible due to direct excitation of the acceptor dye.

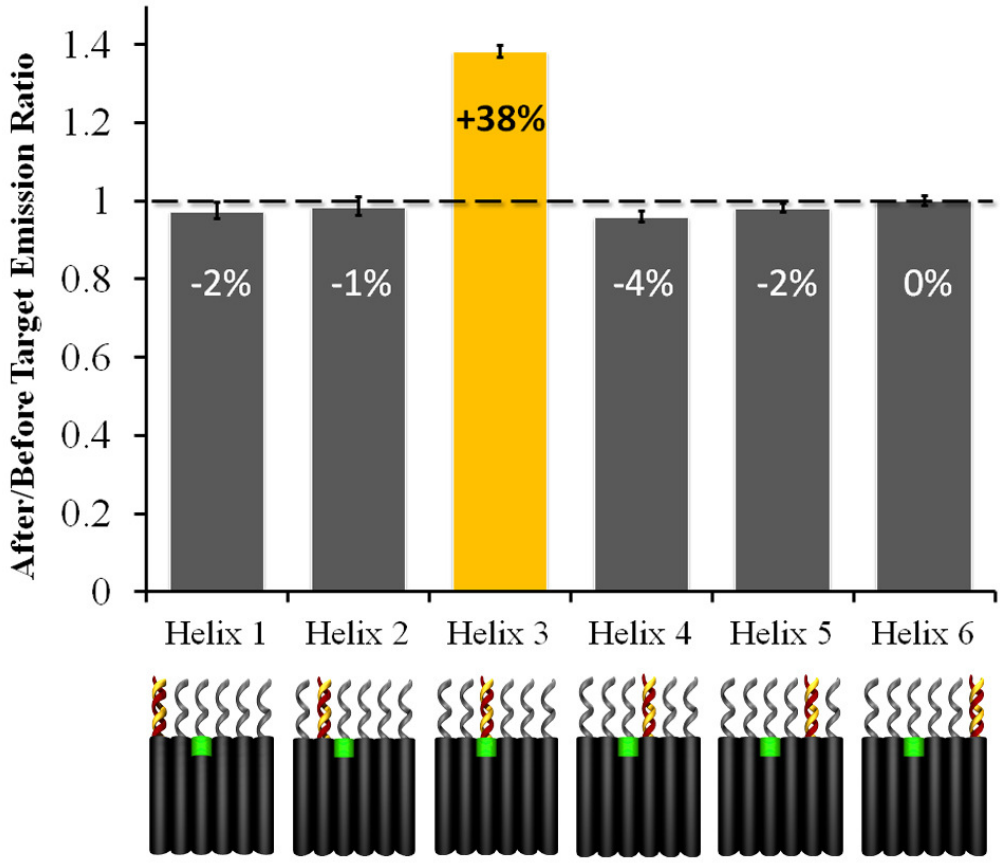

Figure 4.4. Site specificity of the FAM single-dye reporter system. The steady state fluorescence emission of six designs were independently evaluated, where the helical position of the Target Probe was systematically changed, while the position of the FAM dye remained constant at position C (helix 3). Each design corresponds to a situation in which the site of the Target Probe is surrounded by single stranded DNA extensions at every non-Target helical position. The bar graph shows the ratio of emission intensity after and before, respectively, the addition of the Target. Only when the Target Probe was located on helix 3, did the emission of the FAM dye (located on the same helix) exhibit ≈40% enhancement (yellow bar).

4.3.2. Dependence of the Rate Constant of Hybridization on Accessibility of the Hybridization Site.

For the simplest system, in which the Target hybridizes to a single TP displayed from the 6HX tile without the interference of any OTPs, hybridization is expected to follow a two-step mechanism: 1) nucleation of a short segment of the incoming Target to the TP, followed by 2) realignment of both strands and 'zipping' up of the remaining nucleotides for fully complementary base-pairing[21]. Nucleation is the rate-limiting step of hybridization at low DNA concentrations (generally in the nano- to micro-molar range), relying on efficient collisions between the two interacting strands so that a cluster of two or three consecutive bases may form base-pairs with the complementary strand and initiate the hybridization process. The subsequent strand realignment and base pairing of the remaining nucleotides are expected to proceed at a much faster rate. In our system, the fluorescence enhancement of the reporter dye only occurs after the nucleotides in the TP closest to the core of the 6HX have formed base pairs with the 3' end of the Target. Consequently, hybridization of the Target to the TP can be simplified to a bi-molecular process, in which an overall rate constant k_{hyb} can be obtained, but the rate constants associated with the nucleation and the 'zipping' steps cannot be distinctly separated. but Moreover, a large excess of Target strand can be employed to further simplify the kinetics, which permits the use of a pseudo-first order kinetic model to determine the rate constants of hybridization. This method reduces the experimental error associated with differences in strand concentration and stoichiometry, increasing the accuracy of the calculated rate constant.

Figure 4.5 shows the change in the intensity of fluorescence of the FAM reporter as a function of time, after the addition of a 20-fold excess of Target to a solution of 6HX tiles (1 nM) which has the TP displayed at Position C, and no DNA surrounding the site of hybridization. The resulting curve was well fit by a mono-exponential growth equation, as expected for a pseudo-first order reaction, yielding a bi-molecular rate constant of $(1.04 \pm 0.05) \times 10^6$ $s^{-1}M^{-1}$. 6HX tiles with TPs displayed at positions A and B (with the corresponding FAM reporters at positions A and B, respectively) were also tested. An approximate 10% decrease in the hybridization rate constants were observed for the interior positions, compared to the terminal position (Figure 4.6, left series). The expected decrease in the rate of hybridization due to reduced accessibility to the Target Probe, innermost>inner>outermost, was corroborated by the observed hybridization rates. This magnitude of change is significant based on the accuracy of our measurements (SD ≈ 1-2%).

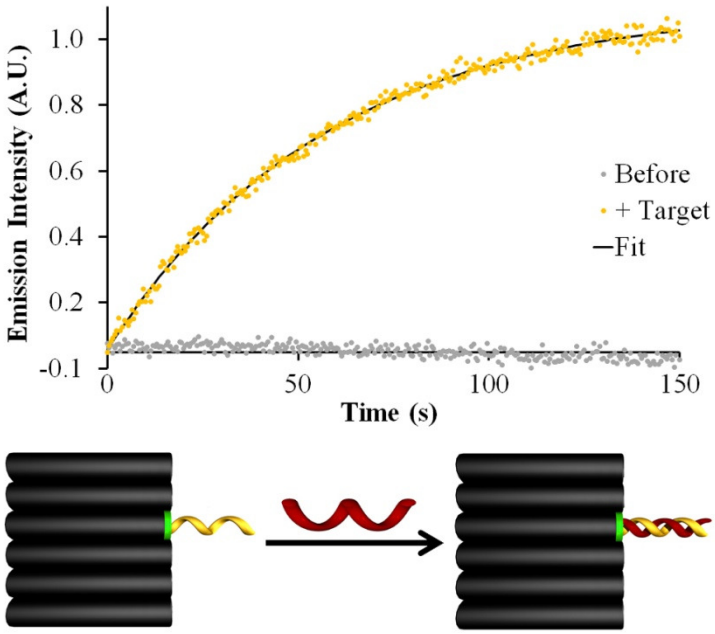

Figure 4.5. Monitoring the hybridization of a 20nt DNA Target to a complementary Target Probe displayed from a 6HX Tile. The measurements correspond to a design in which the Target Probe is located at position C, without the presence of neighboring Off-Target Probes. The hybridization event is monitored in real time by measuring the emission change of FAM dye that occurs as the local environment of the dye changes. Before the addition of Target (schematic, left), the fluorescence emission of a 1 nM 6HX tile solution containing the FAM dye reporter was measured for 150 seconds, providing a baseline signal (gray series). Immediately after the addition of 20 equivalents of Target strand, fluorescence intensity of the same solution was monitored in real time (yellow series). The curve of emission intensity as a function of time was fit by a mono-exponential growth equation, yielding the bi-molecular rate constant of the overall hybridization reaction.

When single-stranded OTPs were displayed from the five helices flanking the TP, a further decrease in the hybridization rate constant was observed (for all three positions – Figure 4.6, middle panel), compared to their counterparts with no OPTs. The presence of single-stranded DNA surrounding the hybridization site is likely to impair the approach of the Target strand, and consequently, reduce the rate of efficient collisions necessary for nucleation. One might argue that the slower kinetics was a result of a decreased effective Target concentration, due to partial interaction of the Target with the OTPs. However, considering the large excess of Target, and negligible sequence complementarity between the Target and the poly(T) OTPs, this scenario is highly unlikely. It is also interesting that the presence of single-stranded DNA surrounding the hybridization site results in a noticeable difference between the observed hybridization rates at Position B and Position C (Figure 4.6, middle panel), an effect that is not as significant for 6HX tiles with no OTPs. This result confirms that the DNA strands flanking the hybridization site further reduces access to the TP.

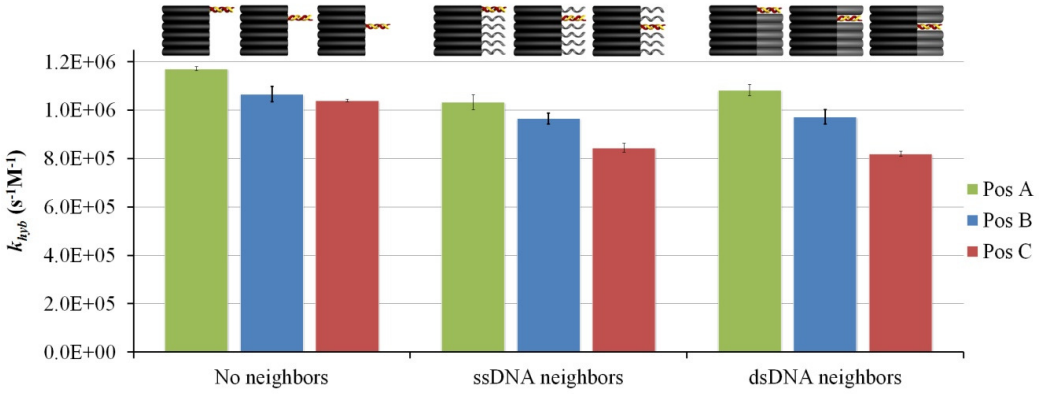

Figure 4.6. Summary of observed hybridization rate constants for various levels of steric crowding of the Target binding site. The left three bars correspond to designs in which the site of Target hybridization is not surrounded by single or double stranded DNA. The middle three bars correspond to designs in which the Target Probe is crowded by the presence of single stranded DNA. The three bars on the right correspond to designs in which the Target Probe is crowded by the presence of double stranded DNA. For all three sets of data, the green, blue, and red bars represent designs in which the Target Probe is located at position A, B, and C, respectively.

6HX tiles with double-stranded DNA surrounding the TP were also assembled and the kinetics of hybridization was measured for different TP positions (Figure 4.6, right panel). Compared to the case with single stranded DNA surrounding the site of hybridization, the presence of double stranded DNA is expected to further reduce the steric accessibility of the Target to the TP, thus leading to a decrease in the overall rate of hybridization. However, the results revealed no significant changes in the rate constants for any of the TP positions in these two cases. It is possible that the rigidity of double strand DNA restricts the distribution of available spatial orientations, while the flexibility of single stranded DNA allows the probe extensions to sample more space, blocking access to the hybridization site. Therefore, the effects of an increased mass (crowding) and decreased spatial distribution of the adjacent double stranded DNA cancel each other and result in similar kinetics as observed for the single stranded case.

It has long been speculated that there is a positional and steric crowding effect on the equilibrium and kinetics of hybridization of a DNA nanostructure probe to an externally added target strand[37].This group of experiments represents the first attempt to obtain quantitative information about these effects. Indeed, the peripheral positions with no or few neighboring strands exhibit significantly faster hybridization kinetics compared to the internal ones, however, the difference is relatively small, only 10%.

The observed rate constants are 4 orders of magnitude slower than diffusion limited bi-molecular reaction kinetics, indicating the presence of a high activation energy barrier for the rate limiting step. We propose that variations in

the rate constants of hybridization are a direct consequence of the spatial confinement of the TP. This is based on two observations: first, the nucleotide sequence of the TP was intentionally held constant for all experiments to avoid any differences in the length and stability of the Target/TP complexes, so that the change in kinetics is not because of any change in the nucleation step. Second, the addition of single and double stranded DNA to a 6HX tile increases its mass and hydrodynamic radius, consequently affecting the diffusion coefficient of the tile, which might cause a reduction in the hybridization rate constant. However, when comparing tiles with single- or double-stranded OTPs, for the same TP position, no significant difference in the rate of hybridization was observed. Therefore, the differences in the rate constants of hybridization of the target to the DNA tiles with or without OTPs cannot be attributed to differences in mass (variation in diffusion coefficients), but directly reflect the spatial accessibility of the TP.

Several questions remain: 1) does the presence of DNA surrounding the TP site reduce the frequency of effective collisions leading to nucleation; 2) is realignment of the nucleated Target impaired due to steric hindrance, or 3) is there a combination of both effects? To answer these questions, the hybridization kinetics of all previously mentioned 'steric accessibility' designs was measured at 4 different temperatures between 10 °C to 20 °C. Typical Arrhenius behavior was observed in all cases (Appendix C), yielding positive activation energies with similar values (Table 4.1) for designs with varying levels of TP accessibility. The energy required to realign the Target/TP pair and to overcome the charge repulsion and solvent reorganization are equivalent for all the presented scenarios.

This result indicates that the differences in kinetics are due to the frequency of efficient collisions between the two strands that lead to a complete hybridization event. Thus, nucleation in a more spatially confined environment is responsible for the slower hybridization kinetics, rather than 'zipping up' and strand realignment.

Table 4.1. Activation energies for the hybridization of a single stranded DNA Target to a 6HX tile for each of the designs shown in Figure 4.6. Regardless of the Target Probe position, or the presence/absence of DNA surrounding the Target Probe, the energy to initiate Target hybridization is approximately 20 kcal/mol.

	Target Probe Position	Activation Energy ($kcal.mol^{-1}$)
no Neighbors	Position A	19.9 ± 1.2
	Position B	18.6 ± 1.1
	Position C	19.3 ± 1.2
ssDNA Neighbors	Position A	20.4 ± 1.2
	Position B	19.9 ± 1.2
	Position C	20.0 ± 1.2
dsDNA Neighbors	Position A	18.4 ± 1.1
	Position B	20.1 ± 1.2
	Position C	19.4 ± 1.2

4.3.3. Effects of Probe Secondary Structure and Target Probe-Off Target Probe Interactions.

In addition to evaluating how steric crowding affects the rate of hybridization of a single stranded DNA target to a 6HX tile, we also characterized how the presence of secondary structure in the TP, and the interaction of the TP with other components of the tile influenced the rate of hybridization. From a practical standpoint, there are many situations in which a given 'probe' sequence is flanked by neighboring single stranded DNA of a different sequence. As the length of the strands increases, there is greater probability of partial sequence complementarily between the strands. When there are base-pairing interactions between the TP and adjacent single stranded DNA, complete hybridization of the Target can only be achieved through a strand displacement reaction[38]. In this case, hybridization of the Target to the 6HX tile can no longer be regarded as a straightforward bimolecular event, but rather a more complex process involving at least three-steps: 1) nucleation of the incoming Target with a single-stranded segment of the TP, 2) realignment and partial hybridization of the strands in the available single-stranded stretch of the TP, and 3) displacement of the hybridized domain of the neighboring, single-stranded DNA from the TP, until full hybridization of the Target strand is achieved. It should be noted that the interaction of the TP with adjacent, single-stranded DNA in a DNA tile is an intramolecular interaction. As a consequence, the "local molecular concentration" increases dramatically, or more precisely, the frequency of collisions that may lead to a TP-ssNeighbor complex is much greater when compared to free strands in solution. Thus, even with minimal

complementarity between a TP and adjacent single-stranded DNA, the effect is amplified beyond what traditional equilibrium calculations would predict.

In our design, the TP and OTPs are arranged parallel to one other with the same polarity. In order to create partial complementarity between the probes, one of the strands must bend toward the other so that anti-parallel base-pairing can occur. To fully evaluate the influence of the interaction and secondary structure of the TP on hybridization kinetics, two distinct situations were considered: 1) the OTP bends toward the TP to form a partially hybridized complex, and 2) the TP bends toward one of the adjacent OTPs (Figure 4.7). The number of base-pair interactions between the Target and OTPs were intentionally varied and evaluated. For all corresponding designs, the TP and the FAM reporter dye were located at helical Position C. The kinetics of hybridization was measured as described previously, and the resulting fluorescence signals were fit by a mono-exponential growth law. The observed rate constants represent a combination of the rates of all three hybridization steps, nucleation, realignment, and strand displacement, into an overall hybridization rate constant. The three phases of hybridization cannot be separated using the current experimental approach.

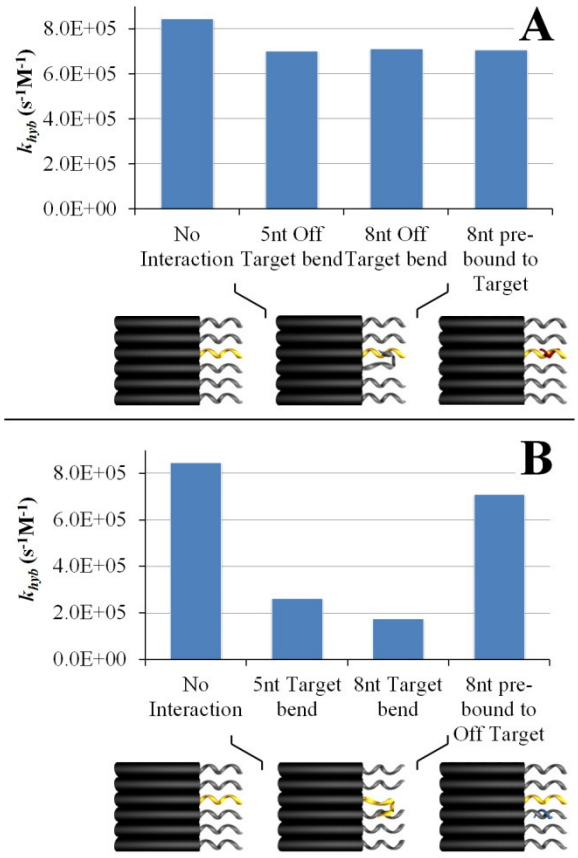

Figure 4.7. Summary of observed hybridization rate constants for variable probe interaction/structure designs. (a) The results of experiments in which the 3' end of the Off Target Probe (sequence designed to be complementary to a domain of the Target Probe) bends toward the Target Probe, forming 5 and 8 bp double helices (middle two bars). The left bar represents the rate constant for a similar design without any complementarity between the Target and Off Target Probes. The right bar shows the rate constant of hybridization in the presence of a pre-bound, 8nt Truncated Target that required displacement by the full length Target. The interaction between the Target and Off Target probes reduced the rate constant of hybridization by ≈16%.

Figure 4.7. continued (b) The results of experiments in which the 3' end of the Target Probe (complementary to a domain of the Off Target Probe) bends toward the Off Target Probe, forming 5 and 8 bp double helices (middle two bars). This situation not only reduces the accessibility of the Target Probe to the invading Target, but also introduces a Target Probe structure with a different character than in (a). Again, the bar on the left represents the rate constant for a similar design without any secondary structure. This specific type of complementarity between the Probes and resulting structure of the Target Probe resulted in a significant 79% decrease in the rate constant of hybridization compared to experiments with no interactions between the Probes. The bar on the right reveals that the rate constant is restored by pre-binding an 8nt Truncated Target to the Target Probe binding domain of the Off-Target Probe.

First, situation 1 was evaluated, where the OTP bends toward the TP to form an 8 base-pair double helix (Figure S4 in Appendix C). A control experiment was designed to determine how the presence of an 8-nt Truncated Target (rather than the full length 20-nt Target) would interfere with the full Target hybridization. An excess of the Truncated Target was pre-hybridized (before addition of the full Target) to a complementary, 8-nt domain of the TP. The double helix formed between the Truncated Target and the TP left an 11-nt toehold at the 3' end of the TP, which serves as a docking station for the incoming full Target. The observed rate constant of full Target hybridization was *circa* 17% lower than the normal case in which no Truncated Target was present (Figure 4.7a). When the same 8-nt domain was transferred to the OTP adjacent to the TP, allowing the end of the OTP to bend and form an 8 base-pair double helix with the TP, the same hybridization rate constant that was observed in the presence of the 8nt Truncated Target (Figure 4.7a). Similarly, when the sequence of the OTP was changed to permit it to bend to form 5 base-pairs (rather than 8 base-pairs) with the TP (Figure S5 in Appendix C), the same hybridization rate was observed. These results imply that the presence of secondary structure (bending) itself in the OTP causes no additional interference in the rate of hybridization of the Target than does pre-hybridization of a Truncated Target. Varying the length of this partial hybridization does not cause any significant difference in the kinetics, either. Therefore, the nucleation site for the hybridization event is close to the 3' end of the TP, which is most accessible for the Target strand introduced in solution.

It is noted that both the 5-nt and 8-nt OTP bending complexes have the same, 8-nt toehold at the 3' end of the TP. This observation raises the question of whether the reduction in the observed rate (compared to the control sample) was due to the presence of an additional hybridization step of strand displacement, or due to a decrease in the number of nucleotides in the TP available for nucleation. Zhang and Winfree[39] presented a model demonstrating that the kinetics of strand displacement reactions is dependent on the toehold length (and AT/GC content). The authors relate an increase in the rate constant with higher toehold binding energy. For a toehold mediated strand displacement reaction, their model predicts that an 8-nt long toehold will have a rate constant between 10^5-10^6 $M^{-1}s^{-1}$, depending on the toehold AT/GC content. This result is in the same order of magnitude as the hybridization rate constants measured in our system. It should be noted that in their study, Zhang and Winfree[39] used simple DNA oligonucleotides, where the sequences were designed to eliminate any undesirable secondary structure. In our study, because secondary structure was intentionally introduced, and one of the participants in the hybridization reaction was a 6HX tile with much slower diffusion than simple, single-stranded DNA, it is difficult to quantitatively compare these two results. However, some qualitative information can still be inferred. Zhang and Winfree[39] proposed a reasonable simplification of their three-step kinetic model (for toehold lengths greater than 5-nt), where the overall rate constant for a strand displacement reaction is approximately equal to the rate constant for the nucleation/zipper step of hybridization. This corresponds to the set of experiments described here, in which an 8-nt toehold was used.

Considering our results and those of Zhang and Winfree[39], it is reasonable to assume that the observed decrease in the rate constant of Target hybridization is due to a decrease in the number of nucleotides available for nucleation, rather than the presence of an additional strand displacement step.

Next, situation 2 was evaluated, where the 3' end of the TP bends to interact with the OTP forming a 5 base-pair double helix (Figure 4.7b). For this case, a rate constant of 3.1×10^5 $M^{-1}s^{-1}$ was observed, representing a dramatic 69% decrease in the hybridization rate. This result indicates that the presence of secondary structure within the TP further isolates it from the invading Target (Figure S6 in Appendix C), drastically reducing the nucleation rate and consequently, the hybridization process. In the case of a longer, 8-nt base-pair interaction between the Target and Off-Target Probes (Figure S7 in Appendix C), an additional decrease in the rate of hybridization was observed (a 79% decrease compared to experiments with no interaction between Probes, Figure 4.7b). A higher level of inaccessibility and/or a further reduction of the number of nucleation sites are expected to contribute to the slower hybridization rate. Finally, a free 8-nt strand was pre-hybridized to the interaction domain of the OTP preventing an inter-probe interaction, freeing the TP for hybridization of the Target. With no requirement to displace the Off-Target and without any secondary structure within the TP, the rate of hybridization increased to the expected level (Figure 4.7b).

We propose that the changes in hybridization rate constants reported here are due to a single factor: the probability of nucleation. The number of Target

trajectories that produce successful collisions leading to hybridization is dependent on the steric hindrance caused by the position of the Target Probe within the tile, and also the presence of other DNA surrounding the site of hybridization. When considering the presence of secondary structure between the TP and the flanking single stranded DNA, double stranded domains between the TP and neighboring DNA reduce the probability of nucleation. This effect is more pronounced at the free 3' end of the TP than at the 5' end, where greater shielding by neighboring DNA already occurs. This explains why no differences in kinetics between the 5-nt and 8-nt long double stranded domains were observed. Moreover, an equivalent interaction is attained when the TP bends towards the flanking neighboring strand, with a more dramatic decrease in hybridization rate constant. For this case, the nucleation site is more deeply entrenched among the neighbor strands and the tile core, reducing the number of trajectories available for nucleation, and thus the probability of successful collisions.

4.4. Materials and Methods

See APPENDIX C

4.5. Conclusions

The results presented here strongly suggest that the rate constant of hybridization of a DNA strand to its complementary probe within a DNA tile is strongly dominated by a rate-limiting nucleation step. In the presence of additional DNA surrounding the hybridization site, the frequency of successful collisions between the Target and the Target Probe, and the subsequent hybridization of nucleotides is reduced due to the steric impairment of the Target

binding site. Particularly, the hybridization rate is more severely affected by the formation of secondary structures between the Target Probe and the adjacent DNA. For all reported experiments here, the sequences of the Target and the Target Probe were held constant. It is reasonable to predict that changes in the sequences of the hybridization pairs, or those of the adjacent DNA, will produce different behavior, thus, additional study is required to obtain a more comprehensive understanding of the hybridization kinetics in DNA nanostructures.

In the context of DNA nanotechnology, it is crucial to understand how the thermodynamics and kinetics of the final structure formation are affected by the number, length, sequence, and structure of the strands connecting the supramolecular arrangements. We believe that the results presented here will contribute to a better understanding of the physical behavior of DNA nanostructures. It will be interesting to determine if the effects observed for a 1D arrangement of DNA probes will translate to more complex architectures, and whether the effects are cumulative and amplified when multiple hybridization sites are present. The design of DNA walkers and other DNA-based motors will benefit from such knowledge, where the arrangement of single stranded extensions (or tracks) in 1D or 2D arrangements may be tuned and optimized by considering the effects of the surrounding local environment. Notably, the presence of double-stranded DNA will not affect the hybridization of the walker to a DNA tile any more than their single-stranded DNA counterparts. In addition, hybridization of DNA targets to a network of probes will likely occur at a faster

rate for peripheral probes than for interior ones, and in the context of DNA-walkers, this may result in walker path bias. Finally, the application of micro-array-based platforms for disease detection can benefit from improved sequence design and spatial control of the probes to enhance the kinetics of DNA hybridization.

It is our hope that the work presented here expands beyond its application in the field of DNA nanotechnology to be used as a proof-of-concept for the study of other molecules and systems that require precise spatial arrangement of components for the study of chemical kinetics.

4.6. References

(1) Aldaye, F. A.; Palmer, A. L.; Sleiman, H. F. *Science* **2008**, 321, 1795-1799.

(2) Shih, W. M.; Lin, C. *Curr. Opin. Struc. Biol.* **2010**, 20, 276-282.

(3) Kuzuya, A.; Komiyama, M. *Nanoscale* **2010**, 2, 310-322.

(4) Tørring, T.; Voigt, N. V.; Nangreave, J.; Yan, H.; Gothelf, K. V. *Chem. Soc. Rev.* **2011**, ASAP.

(5) Pinheiro, A. V.; Han, D.; Shih, W. M.; Yan, H. *Nat. Nanotechnol.*, in press.

(6) Zhang, D. Y.; Seelig, G. *Nat. Chem.* **2011**, 3, 103-113.

(7) Han, D.; Pal, S.; Liu, Y.; Yan, H. *Nat. Nanotech.* **2010**, 5, 712-717.

(8) Goodman, R. P.; Heilemann, M.; Doose, S.; Erben, C. M.; Kapandis, A. N.; Turberfield, A. J. *Nature* **2008**, 3, 93-96.

(9) Lo, P.; Karam, P.; Aldaye, F.; Hamblin, G.; Cosa, G.; Sleiman, H. *Nat. Chem.* **2010**, 2, 319-328.

(10) Gu, H.; Chao, J.; Xiao, S.-J.; Seeman, N. C. *Nature* **2010**, 465, 202-205.

(11) Lund, K.; Manzo, A. J.; Dabby, N.; Michelotti, N.; Johnson-Buck, A.; Nangreave, J.; Taylor, S.; Pei, R.; Stojanovic, M. N.; Walter, N. G.; Winfree, E.; Yan, H. *Nature* **2010**, 465, 206-210.

(12) Wickham, S. F. J.; Endo, M.; Katsuda, Y.; Hidaka, K.; Bath, J.; Sugiyama, H.; Turberfield, A. J. *Nat. Nanotechnol.* **2011**, 6, 166-169.

(13) Chen, X.; Ellington, A. D. *Curr. Opin. Biotechnol.* **2010**, 21, 392-400.

(14) Stojanovic, M. N. *Isr. J. Chem.* **2011**, 51, 99-105.

(15) Yin, P.; Choi, H. M. T.; Calvert, C. R.; Pierce, N. A. *Nature* **2008**, 451, 318-322.

(16) Qian, L.; Winfree, E. *Science* **2011**, 332, 1196-1201.

(17) Dirks, R. M.; Pierce, N. A. P. Natl. Acad. Sci. USA 2004, 101, 15275-15278.

(18) Choi, H. M. T.; Chang, J. Y.; Trinh, L. A.; Padilla, J. E.; Fraser, S. E.; Pierce, N. A. Nat. Biotechnol. 2010, 28, 1208-1212.

(19) Delebecque, C. J.; Lindner, A. B.; Silver, P. A.; Aldaye, F. A. *Science*, in press.

(20) Chen, C.; Wang, W.; Wang, Z.; Wei, F.; Zhao, X. S. *Nucleic Acids Res.* **2007**, 35, 2875-2884.

(21) Wetmur, J. G. *Annu. Rev. Biophys. Bioeng.* **1976**, 5, 337-361.

(22) Morrison, L. E. and Stols, L. M. *Biochemistry* **1993**, 32, 3095-3104.

(23) Yin, Y. and Zhao, X. S. *Accounts Chem. Res.* **2011**, ASAP.

(24) Sacca, B.; Meyer, R.; Feldkamp, U.; Schroeder, H.; Niemeyer, C. M. *Angew. Chem. Int. Ed.* **2008**, 47, 2135-2137.

(25) Miyoshi, D.; Sugimoto, N. *Biochimie* **2008**, 90, 1040-1051.

(26) SantaLucia, J.; Hicks, D. *Annu. Rev. Biophys. Biomol. Struct.* **2004**, 33, 415-440.

(27) Yuan, B.; Zhuang, X.; Hao, Y.; Tan, Z. *Chem. Commun.* **2008**, 48, 6600-6602.

(28) Nangreave, J.; Yan, H.; Liu, Y. *Biophys J.* **2009**, 97, 563-571.

(29) Nangreave, J.; Yan, H.; Liu, Y. *J. Am. Chem. Soc.* **2011**, 133, 4490-4497.

(30) Ke, Y.; Liu, Y.; Zhang, J.; Yan, H. *J. Am. Chem. Soc.* **2006**, 128, 4414-4421.

(31) Delgadillo, R. F. and Parkhurst, L. J. *Photochem. Photobiol.* **2009**, 86, 261-272.

(32) Murakami, A.; Nakaura, M.; Nakatsuji, Y.; Nagahara, S.; Tran-Cong, Q.; Makino, K. *Nucleic Acids Res.* **1991**, 19, 4097-4102.

(33) Kumke, M. U.; Li, G.; Linn, C. P. *Anal. Chem.* **1995**, 67, 3945-3951.

(34) Torimura, M.; Kurata, S.; Yamada, K.; Yokomaku, T.; Kamagata, Y.; Kanagawa, T.; Kurane, R. *Anal. Sci.* **2001**, 17, 155-160.

(35) Crockett, A. O. and Wittwer, C. T. *Anal. Biochem.* **2001**, 290, 89-97.

(36) Doose, S.; Neuweiler, H.; Sauer, M. *ChemPhysChem* **2009**, 10, 1389-1398.

(37) Ke, Y.; Nangreave, J.; Yan, H.; Lindsay, S.; Liu, Y. *Chem. Comm.* **2008**, 43, 5622-5624.

(38) Yurke, B.; Mills, A. P. *Genet. Program. Evol. M.* **2003**, 4, 111-122.

(39) Zhang, D. Y. and Winfree, E. *J. Am. Chem. Soc.* **2009**, 131, 17303-17314.

Chapter 5

Summary and Outlook

5.1. Conclusions

An important goal of nanotechnology is to develop complex, self-assembling systems with predictable 3D structure, molecular dynamics, and functionality. DNA nanotechnology is an area of nanotechnology that is accomplishing these goals with considerable success. *Structural* DNA nanotechnology has achieved the construction of multi dimensional objects of varying sizes and complexity using 'bottom-up' DNA self-assembly, in which the products are a function of the equilibrium end-states of the system, and has culminated in the development of macroscopic materials with nanometer scale addressability. In contrast, dynamic DNA nanotechnology is exemplified by reconfigurable and autonomous devices in which the critical feature of the system is the non-equilibrium dynamics of the components rather than the equilibrium states. A number of open challenges remain to fully exploit the potential of self-assembled DNA nanostructure systems, including reducing assembly error rates and finely programming the interaction between system components (beyond simple base complementarity). These challenges motivated an investigation of the equilibrium (thermodynamics) and non-equilibrium (kinetics) association behavior of several representative DNA nanostructures, illuminating several factors that govern their higher-order self-assembly.

The research presented in this dissertation represents fundamental steps toward achieving a greater understanding of the essential factors that affect the

organization of discrete DNA nanostructures into higher-order constructions. First, several discrete multi-helical DNA tiles were chosen to serve as representative DNA nanostructures; their assembly into higher-order dimer super-structures through sticky end cohesion was monitored and the equilibrium products were analyzed. The valency of the tiles was intentionally varied to identify the degree with which polyvalency affects the assembly process. The number of interactions between the DNA nanostructures and the arrangement of the contact points were found to influence the thermal stability of the assembled super-structures. In general, the greater the number of interactions between the discrete structures, the higher the stability, with the highest stability reserved for those nanostructures in which the contact points were clustered together. Presumably, closely spaced interactions act in a cooperative manner as opposed to independently, enhancing the thermal stability of the products.

Next, the influence of conformational flexibility of discrete DNA nanostructures on their assembly into higher-order dimer super-structures through sticky end cohesion was investigated. Several representative DNA nanostructures with well-characterized structural flexibility were selected for the study and the equilibrium products of their association were analyzed. Flexible DNA nanostructures were found to assemble into dimers with moderate stability, while dimers composed of rigid nanostructures were significantly more stable. Identification of the enthalpic and entropic contributions to the overall free energy of nanostructure association provided a more detailed view of the assembly process. While the enthalpic contribution of the weak interactions (hydrogen

bonding, polar forces, dispersive interactions, etc.) between DNA nanostructures was more favorable for flexible structures, the entropic penalty was significant, leading to lower stability of the equilibrium products. Meanwhile, the enthalpic contribution of the weak interactions was not as favorable for the dimerization of rigid structures, however, the reduced entropic penalty lead to the most stable association. It is reasonable to hypothesize that increased conformational flexibility allows the weak interactions through which the nanostructures associate to adopt the most favorable arrangement in space, leading to greater stability. However, rigidity within a DNA nanostructure results in the effective pre-organization of the binding site, with the entropic cost of binding groups paid when the individual nanostructure is assembled. Association of the discrete DNA nanostructures demonstrated a well known thermodynamic phenomenon referred to as enthalpy-entropy compensation in which there is a linear relationship between the enthalpy and entropy changes. Overall, the most stable higher-order structures were formed from rigid components, while the least stable were formed from flexible components, with a very large (> 10°C) margin between the two cases.

Finally, the non-equilibrium characteristics of the assembly of DNA nanostructures into higher-order complexes were examined. A multi-helical DNA nanostructure was selected to serve as a nanoscale ‘molecular chip’, for the ‘detection’ of an oligonucleotide ‘target’. The influence of binding site accessibility and character was evaluated in the study. Varying degrees of crowding of the binding site were achieved by inclusion or exclusion of certain

features of the corresponding nanostructures. Several states of crowding were simulated, from near complete accessibility (relative to the other states) to virtual inaccessibility. The rate of transformation from individual unbound DNA nanostructure and oligonucleotide target to bound complex was determined for each crowding situation, revealing that the most accessible binding site results in the fastest transformation from unbound to bound states. However, the difference in the rate of transformation for the two extreme cases of crowding was smaller than expected, with the least accessible binding site corresponding to 30% slower kinetics than the most accessible. Unexpectedly, it wasn't crowding of the binding site, but interactions between the binding site and proximal elements of the DNA nanostructures that led to the greatest reduction in the rate of complexation. The formation of secondary structures between the Target Probe and neighboring single stranded DNA was found to significantly affect the hybridization process, with a nearly order of magnitude reduction in the rate of Target binding in some cases. Presumably, the partial occupation of the binding site by other elements of the DNA nanostructure reduced the number of successful collisions between the target and target Probe and subsequent hybridization of nucleotides. The results presented here strongly suggest that the rate constant of hybridization of a DNA strand to its complement in a DNA tile, in the presence of additional DNA surrounding the hybridization site, is strongly dominated by a rate-limiting nucleation step.

5.2. Future Directions

Considering the diversity of DNA nanostructure building blocks and higher-order structures that have been developed over the past 30 years, there have been remarkably few attempts to characterize the bottom-up self-assembly of DNA nanostructures. Nobel physicist Richard Feynman's statement, "There is (still) plenty of room at the bottom" is an excellent description of the opportunity that exists in DNA nanotechnology to investigate the details of nanostructure self-assembly.[1] With greater knowledge of the equilibrium and non-equilibrium factors that govern intermolecular DNA nanostructure association, it will be possible to exert greater control over the self-assembly process. For example, one of the main obstacles in achieving robust algorithmic DNA self-assembly is the presence of several types of errors: structural, nucleation, and growth errors have hindered the development of this field. As the size of DNA nanostructure building blocks and the consequent DNA nanoarrays increases, the presence of small assembly errors lead to large defects in the products. It may be possible to reduce error rates by carefully tuning the kinetics and thermodynamics of assembly, and studies that characterize various assembly situations will lead to better control over the self-assembly process. In addition, this knowledge may lead to more efficient DNA nanostructures that are composed of the minimum number and arrangement of intermolecular interactions, a favorable atom-by-atom economy of sorts.

There is an ongoing effort to extend control over the self-assembly process to as many dimensions as possible and in some cases, this includes time.[2] In

addition to exerting greater control over end point structures, knowledge of particular DNA nanostructure assembly details could prove useful to dynamic systems. Many DNA nanostructures have been developed to undergo a triggered change in shape with a variety of different principles used to actuate the change including: buffer condition, strand-displacement equilibria, and protein binding.[2] In addition to changes in shape, changes in the size of DNA nanostructure arrays can also be executed. For example a 'hybridization chain reaction' can be used to trigger the self-assembly of DNA nanostructures: the ability to perform this transformation comes from the potential energy that is stored in locked conformations of DNA, such as loops that are kinetically stable at a certain temperature over a long time scale. The conformations may be unlocked using a chain reaction of successive hybridizations initiated by a catalyst oligonucleotide. With knowledge of the rate of transformation of a given hybridization or intermolecular DNA nanostructure recognition event, it will be possible to maximize the performance of dynamic systems by adjusting the structural details of the system components.

5.3. References

(1) Feynman, R. P. *Miniaturization.;* Reinhold Publishing Corp.: New York, 1961; pp 282-296.

(2) Brucale, M.; Zuccheri, G.; Samori, B. *Trends Biotechnol.* **2006**, *24*, 235–243.

Bibliography

Chapter 1 References

(1) Watson, J. D.; Crick, F. H. C. *Nature.* **1953**, *171*, 737-738.

(2) Dahm, R. *Dev. Biol.* **2005**, *278*, 274-288.

(3) Seeman, N. C. *J. Theor. Biol.* **1982**, *99*, 237-247.

(4) Service, R. F. *Science.* **2011**, *332*, 1141-1143.

(5) Hecht, S. M., Ed. *Bioorganic Chemistry: Nucleic Acids;* Oxford University Press: New York, U.S.A., 1996.

(6) Wing, R.; Drew, H.; Takano, T.; Broka, C.; Tanaka, S.; Itakura, K.; Dickerson, R. E. *Nature.***1980**, *287*, 755-758.

(7) Klug, A. *Nature.***1968**, *219*, 808-812.

(8) Bustamante, C.; Bryant, Z.; Smith, S. B. *Nature.* **2003**, *421*, 423-427.

(9) Seeman, N. C. *Acc. Chem. Res.* **1997**, *30*, 357-363.

(10) Britt, A. B. *Annu. Rev. Plant Physiol. Plant Mol. Biol.* **1996**, *47*, 75-100.

(11) Kibbe, W. A. OligoCalc: an online oligonucleotide properties calculator. *Nucleic Acids Res.* [Online] **2007**, ***35,*** 43-46**.** http://nar.oxfordjournals.org/content/35/suppl_2/W43.full (accessed July 27, 2011).

(12) Caruthers, M. H. *Science.* **1985**, *230*, 281-285.

(13) Seeman, N. C. *Nanotechnology.* **1999**, *17*, 437-443.

(14) Seeman, N. C. *Annu. Rev. Biophys. Biomol. Struct.* **1998**, 27, 225-248.

(15) Fu, T. J.; Seeman, N. C. *Biochemistry.* **1993**, 32, 3211-3220.

(16) Chen, J. H.; Kallenbach, N. R.; Seeman, N. C. *J. Am. Chem. Soc.* **1989**, 111, 6402-6407.

(17) Chen, J. H.; Seeman, N. C. *Nature.* **1991**, 350, 631-633.

(18) Zhang, Y.; Seeman, N. C. *J. Am. Chem. Soc.* **1994**, 116, 1661-1669.

(19) Li, X. J.; Yang, X. P.; Qi, J.; Seeman, N.C. *J. Am. Chem. Soc.* **1996**, 118, 6131-6140.

(20) LaBean, T. H.; Yan, H.; Kopatsch, J.; Liu, F. R.; Winfree, E.; Reif, J. H.; Seeman, N. C. *J. Am. Chem. Soc.* **2000**, 122, 1848-1860.

(21) Winfree, E.; Liu, F.; Wenzler, L. A.; Seeman, N. C. *Nature.* **1998**, 394, 539-544.

(22) Liu, Y.; Lin, C.; Li, H.; Yan, H. *Angew. Chem. Int. Ed.* **2005**, 44, 4333-4338.

(23) Lin, C.; Liu, Y.; Rinker, S.; Yan, H. *ChemPhysChem.* **2006**, 7, 1641-1647.

(24) Yan, H.; Park, S. H.; Ginkelstein, G.; Reif, J. H.; LaBean, T. H. *Science.* **2003**, 301, 1882-1884.

(25) Loweth, C. J.; Caldwell, W. B.; Peng, X. G.; Alivisatos, A. P.; Schultz, P. G. *Angew. Chem. Int. Ed.* **1999**, 38, 1808-1812.

(26) Deng, Z. X.; Tian, Y.; Lee, S. H.; Ribbe, A. E.; Mao, C. D. *Angew. Chem. Int. Ed.* **2005**, 44, 3582-3585.

(27) Sharma, J.; Ke, Y.; Lin, C.; Chhabra, R.; Wang, Q.; Nangreave, J.; Liu, Y.; Yan, H. *Angew. Chem. Int. Ed.* **2008**, 47, 5157-5159.

(28) Woodbury, C. P. Introduction to macromolecular binding equilibria; CRC Press: New York, 2008; pp 1-20.

(29) Carlson, H. A.; McCammon, J. A. *Mol. Pharmacol.* **2000**, 57, 213-218.

(30) Mergny, J.-L.; Lacroix, L. *Oligonucleotides.* **2003**, 13, 515-537.

(31) SantaLucia, Jr., J.; Turner, D. H. *Biopolymers.* **1997**, 44, 309-319.

(32) Wartell, R. M.; Benight, A. S. *Phys. Rep.* **1985**, 126, 67-107.

(33) Schmitz, M.; Steger, G. *Comput. Appl. Biosci.* **1992**, 8, 389-399.

(34) Gutfreund, H. *Kinetics for the Life Sciences: receptors, transmitters and catalysts*; Cambridge University Press: Cambridge, U.K., 1995.

Chapter 2 References

(1) Klug, A. *Phil. Trans. R. Soc. Lond. A.* **1994**, *348*, 167-178.

(2) Van Workum, K.; Douglas, J. F. *Phys. Rev. E.* **2006**, *73*, 031502.

(3) Seeman, N. C. *J. Theor. Biol.* **1982**, *99*, 237-247.

(4) Winfree, E.; Liu, F.; Wenzler, L. A.; Seeman, N.C. *Nature.* **1998**, *394*, 539-544.

(5) Chen, J. H.; Seeman, N. C. *Nature.* **1991**, *350*, 631-633.

(6) Yan, H.; Park, S. H.; Finkelstein, G.; Reif, J. H.; LaBean, T. H. *Science.* **2003**, *301*, 1882-1884.

(7) Shih, W. M.; Quispe, J. D.; Joyce, G. F. *Nature.* **2004**, *427*, 618-621.

(8) Goodman, R. P.; Schaap, I. A.; Tardin, C. F.; Erben, C. M.; Berry, R. M.; Schmidt, C. F.; Turberfield, A. J. *Science.* **2005**, *310*, 1661-1665.

(9) Rothemund, P. W.; Papadakis, N.; Winfree, E. *PLOS Biol.* **2004**, *2*, 2041-2053.

(10) Rothemund, P. W. K. *Nature.* **2006**, *440*, 297-302.

(11) Aldaye, F. A.; Sleiman, H. F. *J. Am. Chem. Soc.* **2007**, *129*, 13376-13377.

(12) He, Y.; Ye, T.; Su, M.; Zhang, C.; Ribbe, A. E.; Jiang, W.; Mao, C. *Nature.* **2008**, *452*, 198-202.

(13) Le, J. D.; Pinto, Y.; Seeman, N. C.; Musier-Forsyth, K.; Taton, T. A.; Kiehl, R. A. *Nano Lett.* **2004**, *4*, 2343-2347.

(14) Zhang, J.; Liu, Y.; Ke, Y.; Yan, H. *Nano Lett.* **2006**, *6*, 248-251.

(15) Zheng, J.; Constantinou, P. E.; Micheel, C.; Alivisatos, A. P.; Kiehl, R. A.; Seeman, N. C. *Nano Lett.* **2006**, *6*, 1502-1504.

(16) Sharma, J.; Chhabra, R.; Liu, Y.; Ke, Y.; Yan, H. *Angew. Chem. Int. Ed.* **2006**, *45*, 730-735.

(17) Sharma, J., Y. Ke, C. Lin, R. Chhabra, Q. Wang, Nangreave, J.; Liu, Y.; Yan, H. *Angew. Chem. Int. Ed.* **2008**, *47*, 5157-5159.

(18) Williams, B. A. R.; Lund, K.; Liu, Y.; Yan, H.; Chaput, J. C. *Angew. Chem. Int. Ed.* **2007**, *46*, 3051-3054.

(19) He, Y.; Tian, Y.; Ribbe, A. E.; Mao, C. *J. Am. Chem. Soc.* **2006**, *128*, 12664-12665.

(20) Liu, Y.; Lin, C.; Li, H.; Yan, H. *Angew. Chem. Int. Ed.* **2005**, *44*, 4333-4338.

(21) Malo, J.; Mitchell, J. C.; Venien-Bryan, C.; Harris, J. R.; Wille, H.; Sherratt, D. J.; Turberfield, A. J. *Angew. Chem. Int. Ed.* **2005**, *44*, 3057-3061.

(22) Gothelf, K. V.; LaBean, T. H. *Org. Biomol. Chem.* **2005**, *3*, 4023-4037.

(23) Feldkamp, U.; Niemeyer, C. M. *Angew. Chem. Int. Ed.* **2006**, *45*, 1856-1876.

(24) Seeman, N. C.; Lukeman, P. S. *Rep. Prog. Phys.* **2005**, *68*, 237-270.

(25) Seeman, N. C. *Nature.* **2003**, *421*, 427-431.

(26) Lin, C.; Liu, Y.; Rinker, S.; Yan, H. *ChemPhysChem.* **2006**, *7*, 1641-1647.

(27) LaBean, T. H.; Yan, H.; Kopatch, J.; Liu, F.; Winfree, E; Reif, J. H.; Seeman, N. C. *J. Am. Chem. Soc.* **2000**, *122*, 1848-1860.

(28) Schulman R.; Winfree, E. *Proc. Nat. Acad. Sci*. **2007**, *104*, 15236-15241.

(29) Sacca, B.; Meyer, R.; Feldkamp, U.; Schroeder, H.; Niemeyer, C. M. *Angew. Chem. Int. Ed.* **2008**, *47*, 2135-2137.

(30) Ke, Y.; Liu, Y.; Zhang, J.; Yan, H. *J. Am. Chem. Soc.* **2006**, *128*, 4414-4421.

(31) Sjoback, R.; Nygren, J.; Kubista, M. *Biopolymers*. **1998**, *46*, 445-453.

(32) Ding, B.; Sha, R.; Seeman, N. C. *J. Am. Chem. Soc.* **2004**, *126*, 10230-10231.

(33) Cohen-Tannoudji, C.; Diu, B.; Laloe, F. *Quantum Mechanics, 2nd Edition*. **1977**, *1*, 632.

Chapter 3 References

(1) Mammen, M.; Choi, S. K.; Whitesides, G. M. *Angew. Chem. Int. Ed.* **1998**, *37*, 2754– 2794.

(2) Nangreave, J.; Yan, H.; Liu, Y. *Biophys. J.* **2009**, *97*, 563– 571.

(3) Seeman, N. C. *J. Theor. Biol.* **1982**, *99*, 237– 247.

(4) Seeman, N. C.; Kallenbach, N. R. *Biophys. J.* **1983**, *44*, 201– 209.

(5) Kallenbach, N. R.; Ma, R. I.; Seeman, N. C. *Nature* **1983**, *305*, 829– 831.

(6) Marky, L. A.; Kallenbach, N. R.; McDonough, K. A.; Seeman, N. C.; Breslauer, K. J. *Biopolymers* **1987**, *26*, 1621– 1634.

(7) Cooper, J. P.; Hagerman, P. J. *J. Mol. Biol.* **1987**, *198*, 711– 719.

(8) Churchill, M. E. A.; Tullius, T. D.; Kallenbach, N. R.; Seeman, N. C. *Proc. Natl. Acad. Sci. U.S.A.* **1988**, *85*, 4653– 4656.

(9) Duckett, D. R.; Murchie, A. I. H.; Diekmann, S.; von Kitzing, E.; Kemper, B.; Lilley, D. M. J. *Cell* **1988**, *55*, 79– 89.

(10) Cooper, J. P.; Hagerman, P. J. *Proc. Natl. Acad. Sci. U.S.A.* **1989**, *86*, 7336– 7340.

(11) Murchie, A. I. H.; Clegg, R. M.; von Kitzing, E.; Duckett, D. R.; Diekmann, S.; Lilley, D. M. J. *Nature* **1989**, *341*, 763– 766.

(12) Lu, M.; Guo, Q.; Marky, L. A.; Seeman, N. C.; Kallenbach, N. R. *J. Mol. Biol.* **1992**, *223*, 781– 789.

(13) Mao, C.; Sun, W.; Seeman, N. C. *J. Am. Chem. Soc.* **1999**, *121*, 5437– 5443.

(14) Fu, T. J.; Seeman, N. C. *Biochemistry* **1993**, *32*, 3211– 3220.

(15) Winfree, E.; Liu, F.; Wenzler, L. A.; Seeman, N. C. *Nature* **1998**, *394*, 539– 544.

(16) Miick, S. M.; Fee, R. S.; Millar, D. P.; Chazin, W. J. *Proc. Natl. Acad. Sci. U.S.A.* **1997**, *94*, 9080– 9084.

(17) McKinney, S. A.; Declais, A.-C.; Lilley, D. M. J.; Ha, T. *Nat. Struct. Biol.* **2002**, *10*, 93– 97.

(18) Altona, C. *J. Mol. Biol.* **1996**, *263*, 568– 581.

(19) Petrillo, M. L.; Newton, C. J.; Cunningham, R. P. *Biopolymers* **1988**, *27*, 1337– 1352.

(20) Li, X.; Yang, X.; Qi, J.; Seeman, N. C. *J. Am. Chem. Soc.* **1996**, *118*, 6131– 6140.

(21) Sa-Ardyen, P.; Vologodskii, A. V.; Seeman, N. C. *Biophys. J.* **2003**, *84*, 3829– 3837.

(22) von Kitzing, E.; Lilley, D. M. J.; Diekmann, S. *Nucleic Acids Res.* **1990**, *18*, 2671– 2683.

(23) Eis, P. S.; Millar, D. P. *Biochemistry* **1993**, *32*, 13852– 13860.

(24) Sacca, B.; Meyer, R.; Feldkamp, U.; Schroeder, H.; Niemeyer, C. M. *Angew. Chem. Int. Ed.* **2008**, *47*, 2135– 2137.

(25) Sacca, B.; Meyer, R.; Niemeyer, C. M. *Nat. Protoc.* **2009**, *4*, 271– 285.

(26) Du, S. M.; Zhang, S.; Seeman, N. C. *Biochemistry* **1991**, *31*, 10955– 10963.

(27) Wang, H.; Seeman, N. C. *Biochemistry* **1995**, *34*, 920– 929.

Chapter 4 References

(1) Aldaye, F. A.; Palmer, A. L.; Sleiman, H. F. *Science* **2008**, 321, 1795-1799.

(2) Shih, W. M.; Lin, C. *Curr. Opin. Struc. Biol.* **2010**, 20, 276-282.

(3) Kuzuya, A.; Komiyama, M. *Nanoscale* **2010**, 2, 310-322.

(4) Tørring, T.; Voigt, N. V.; Nangreave, J.; Yan, H.; Gothelf, K. V. *Chem. Soc. Rev.* **2011**, ASAP.

(5) Pinheiro, A. V.; Han, D.; Shih, W. M.; Yan, H. *Nat. Nanotechnol.*, in press.

(6) Zhang, D. Y.; Seelig, G. *Nat. Chem.* **2011**, 3, 103-113.

(7) Han, D.; Pal, S.; Liu, Y.; Yan, H. *Nat. Nanotech.* **2010**, 5, 712-717.

(8) Goodman, R. P.; Heilemann, M.; Doose, S.; Erben, C. M.; Kapandis, A. N.; Turberfield, A. J. *Nature* **2008**, 3, 93-96.

(9) Lo, P.; Karam, P.; Aldaye, F.; Hamblin, G.; Cosa, G.; Sleiman, H. *Nat. Chem.* **2010**, 2, 319-328.

(10) Gu, H.; Chao, J.; Xiao, S.-J.; Seeman, N. C. *Nature* **2010**, 465, 202-205.

(11) Lund, K.; Manzo, A. J.; Dabby, N.; Michelotti, N.; Johnson-Buck, A.; Nangreave, J.; Taylor, S.; Pei, R.; Stojanovic, M. N.; Walter, N. G.; Winfree, E.; Yan, H. *Nature* **2010**, 465, 206-210.

(12) Wickham, S. F. J.; Endo, M.; Katsuda, Y.; Hidaka, K.; Bath, J.; Sugiyama, H.; Turberfield, A. J. *Nat. Nanotechnol.* **2011**, 6, 166-169.

(13) Chen, X.; Ellington, A. D. *Curr. Opin. Biotechnol.* **2010**, 21, 392-400.

(14) Stojanovic, M. N. *Isr. J. Chem.* **2011**, 51, 99-105.

(15) Yin, P.; Choi, H. M. T.; Calvert, C. R.; Pierce, N. A. *Nature* **2008**, 451, 318-322.

(16) Qian, L.; Winfree, E. *Science* **2011**, 332, 1196-1201.

(17) Dirks, R. M.; Pierce, N. A. P. Natl. Acad. Sci. USA 2004, 101, 15275-15278.

(18) Choi, H. M. T.; Chang, J. Y.; Trinh, L. A.; Padilla, J. E.; Fraser, S. E.; Pierce, N. A. Nat. Biotechnol. 2010, 28, 1208-1212.

(19) Delebecque, C. J.; Lindner, A. B.; Silver, P. A.; Aldaye, F. A. *Science*, in press.

(20) Chen, C.; Wang, W.; Wang, Z.; Wei, F.; Zhao, X. S. *Nucleic Acids Res.* **2007**, 35, 2875-2884.

(21) Wetmur, J. G. *Annu. Rev. Biophys. Bioeng.* **1976**, 5, 337-361.

(22) Morrison, L. E. and Stols, L. M. *Biochemistry* **1993**, 32, 3095-3104.

(23) Yin, Y. and Zhao, X. S. *Accounts Chem. Res.* **2011**, ASAP.

(24) Sacca, B.; Meyer, R.; Feldkamp, U.; Schroeder, H.; Niemeyer, C. M. *Angew. Chem. Int. Ed.* **2008**, 47, 2135-2137.

(25) Miyoshi, D.; Sugimoto, N. *Biochimie* **2008**, 90, 1040-1051.

(26) SantaLucia, J.; Hicks, D. *Annu. Rev. Biophys. Biomol. Struct.* **2004**, 33, 415-440.

(27) Yuan, B.; Zhuang, X.; Hao, Y.; Tan, Z. *Chem. Commun.* **2008**, 48, 6600-6602.

(28) Nangreave, J.; Yan, H.; Liu, Y. *Biophys J.* **2009**, 97, 563-571.

(29) Nangreave, J.; Yan, H.; Liu, Y. *J. Am. Chem. Soc.* **2011**, 133, 4490-4497.

(30) Ke, Y.; Liu, Y.; Zhang, J.; Yan, H. *J. Am. Chem. Soc.* **2006**, 128, 4414-4421.

(31) Delgadillo, R. F. and Parkhurst, L. J. *Photochem. Photobiol.* **2009**, 86, 261-272.

(32) Murakami, A.; Nakaura, M.; Nakatsuji, Y.; Nagahara, S.; Tran-Cong, Q.; Makino, K. *Nucleic Acids Res.* **1991**, 19, 4097-4102.

(33) Kumke, M. U.; Li, G.; Linn, C. P. *Anal. Chem.* **1995**, 67, 3945-3951.

(34) Torimura, M.; Kurata, S.; Yamada, K.; Yokomaku, T.; Kamagata, Y.; Kanagawa, T.; Kurane, R. *Anal. Sci.* **2001**, 17, 155-160.

(35) Crockett, A. O. and Wittwer, C. T. *Anal. Biochem.* **2001**, 290, 89-97.

(36) Doose, S.; Neuweiler, H.; Sauer, M. *ChemPhysChem* **2009**, 10, 1389-1398.

(37) Ke, Y.; Nangreave, J.; Yan, H.; Lindsay, S.; Liu, Y. *Chem. Comm.* **2008**, 43, 5622-5624.

(38) Yurke, B.; Mills, A. P. *Genet. Program. Evol. M.* **2003**, 4, 111-122.

(39) Zhang, D. Y. and Winfree, E. *J. Am. Chem. Soc.* **2009**, 131, 17303-17314.

Chapter 5 References

(1) Feynman, R. P. *Miniaturization.;* Reinhold Publishing Corp.: New York, 1961; pp 282-296.

(2) Brucale, M.; Zuccheri, G.; Samori, B. *Trends Biotechnol.* **2006**, *24*, 235–243.

APPENDIX A

SUPPLEMENTAL INFORMATION FOR CHAPTER 2

Supplemental Information

Studies of Thermal Stability of Multivalent DNA Hybridization in a Nanostructured System*

Jeanette Nangreave, Hao Yan*, Yan Liu*

Department of Chemistry & Biochemistry and the Biodesign Institute
Arizona State University, Tempe, AZ, 85287, USA

DNA Sequences

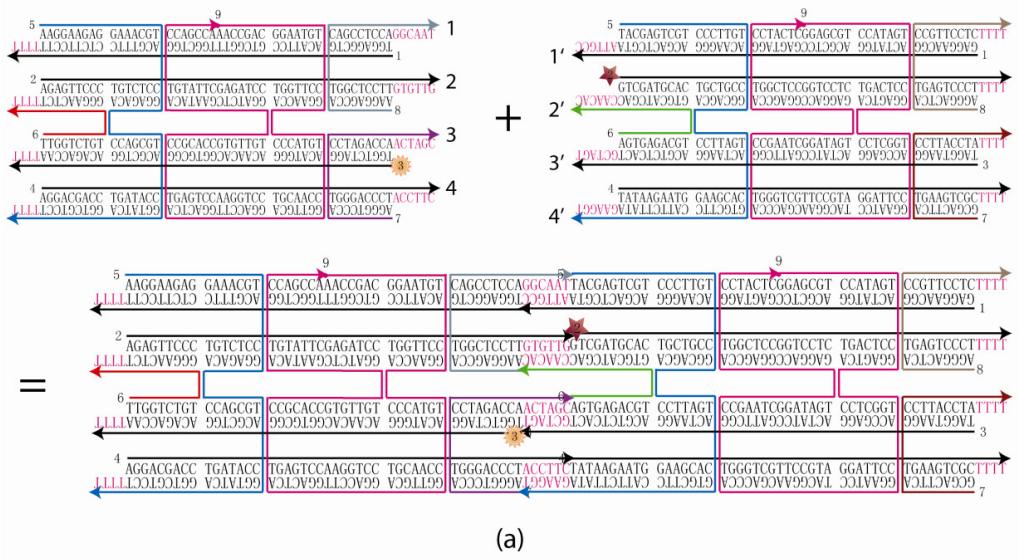

(a)

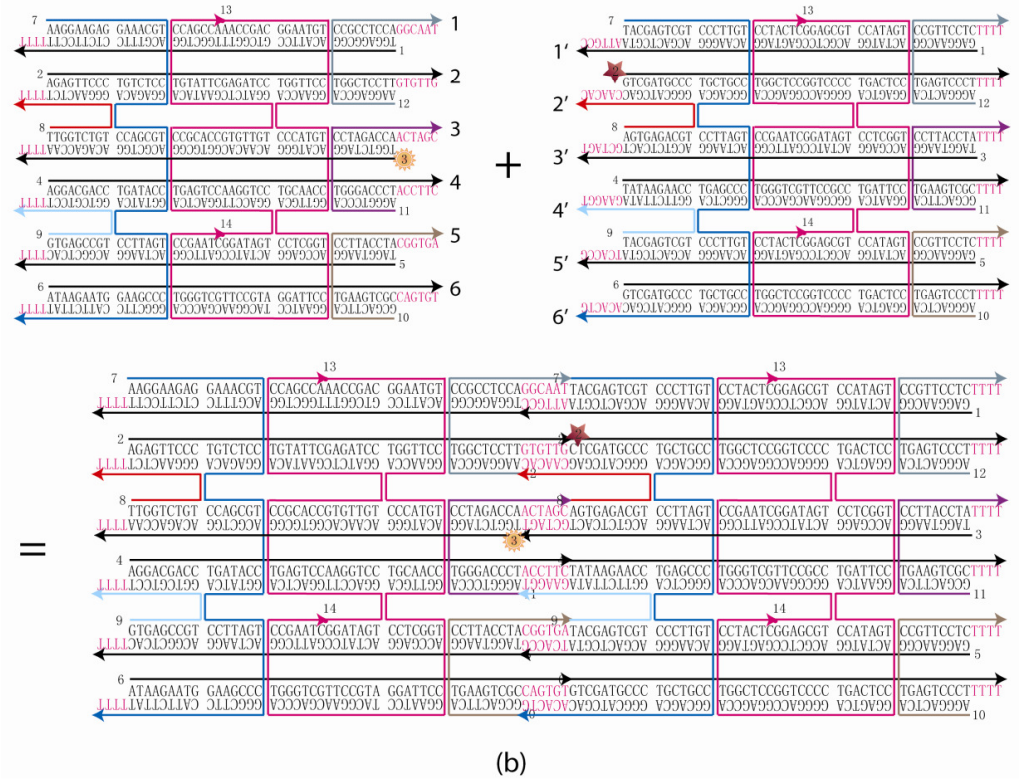

(b)

Figure S1. Schematic representation of the tile to tile association for 4 and 6 helix tiles. DNA sequences used in this study on the self-assembly of 4HX and 6 HX tiles and heterodimers are shown. For detailed design and sequence information for the 4HX system, see Figure S2. Each 6HT consisted of fourteen different oligonucleotides indicated by numbers on the 5' end of each strand. For the entire collection of designs explored for the 6HX system, the reporter oligomers were: 5'-Fsc-oligomer 3 of tile A and 5'-TAMRA-oligomer 2 of tile B. Complementary sticky end sequences are denoted 1-6 and 1'-6'. For every design investigated only oligomers necessary for sticky end cohesion (actual sequence of sticky end portion of oligomer shown in pink) varied, the core sequences of the tiles remained constant. For those designs not employing sticky ends at certain positions, the constituent oligomers at those positions were trimmed back six nucleotides (corresponding to the sticky end sequence).

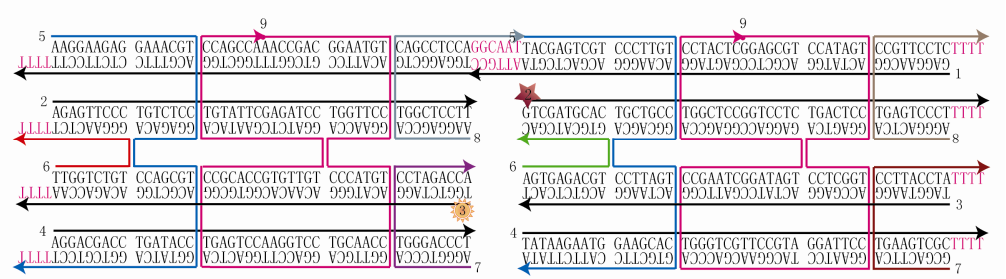

(a) 4-Helix Design #1

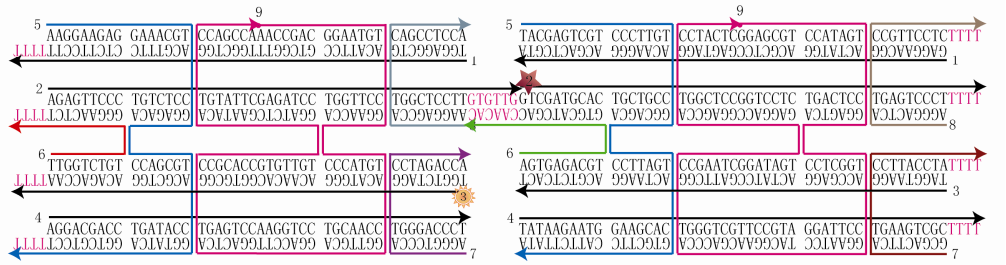

(b) 4-Helix Design #2

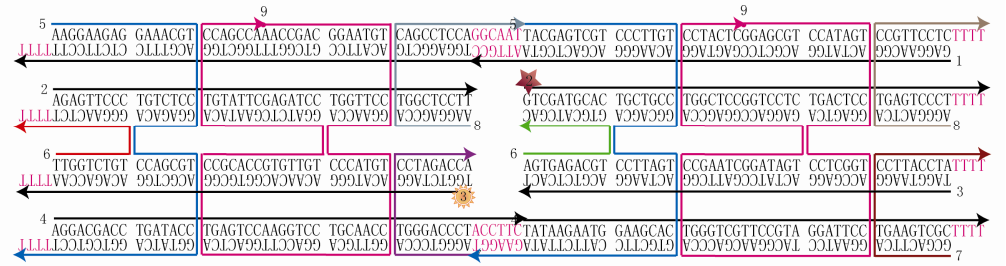

(c) 4-Helix Design #3

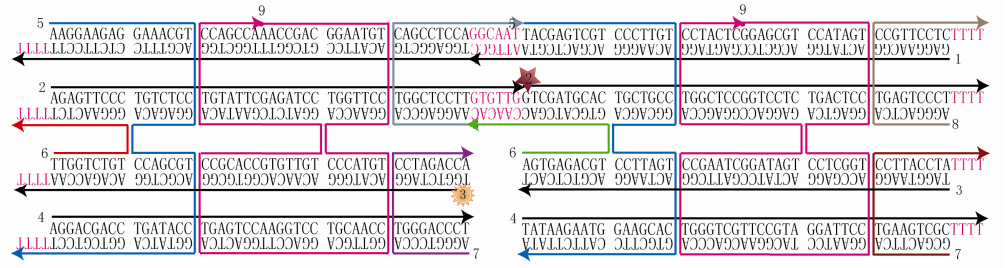

(d) 4-Helix Design #4

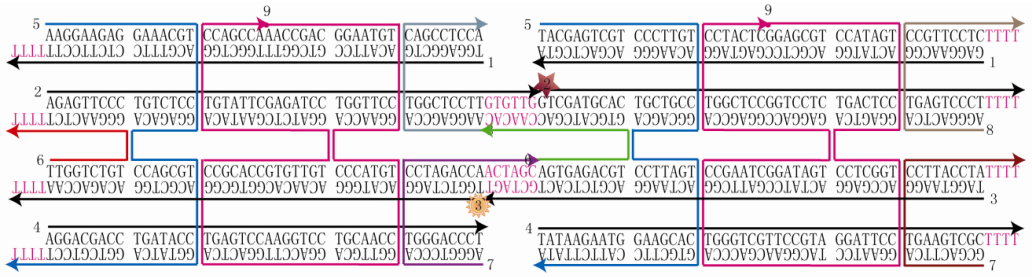

(e) 4-Helix Design #5

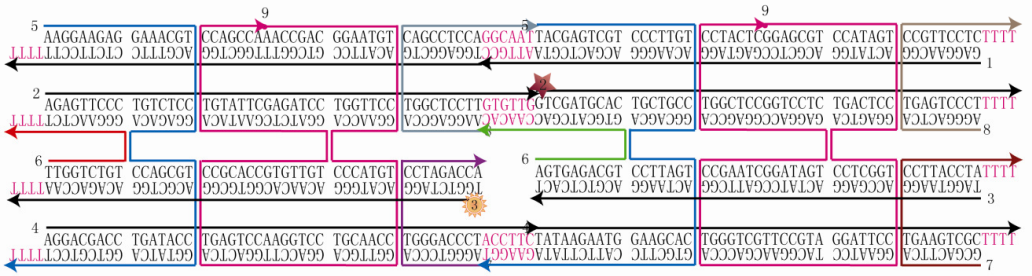

(f) 4-Helix Design #6

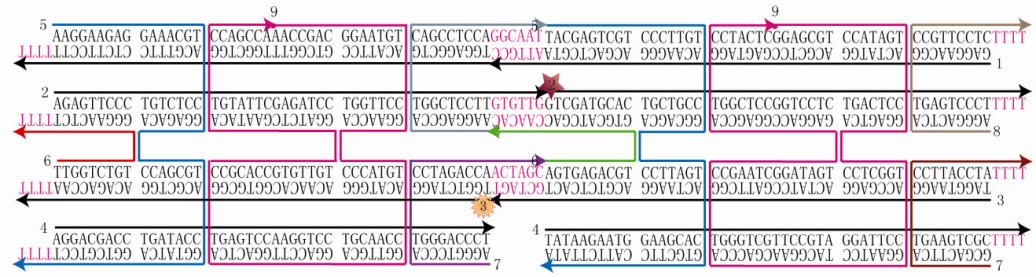

(g) 4-Helix Design #7

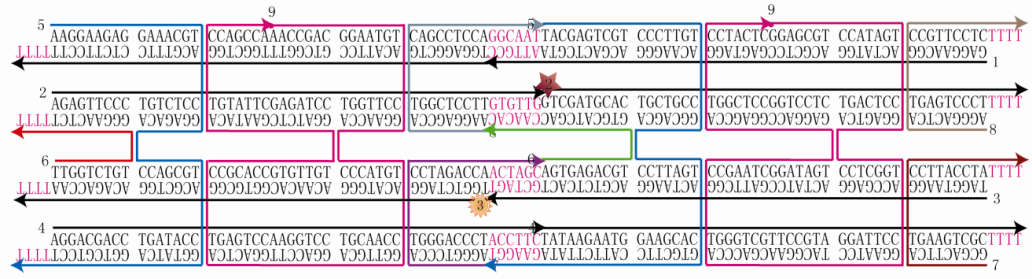

(h) 4-Helix Design #8

Figure S2. Schematic representation of the tile to tile association for 4 helix tiles. DNA sequences used in this study on the self-assembly of 4HX tiles and heterodimers are shown. Each 4HT consisted of nine different oligonucleotides indicated by numbers on the 5' end of each strand. For the entire collection of designs explored for the 4HX system (a-h), the reporter oligomers were: 5'-Fsc-oligomer 3 of tile A and 5'-TAMRA-oligomer 2 of tile B. For every design investigated only oligomers necessary for sticky end cohesion (actual sequence of sticky end portion of oligomer shown in pink) varied, the core sequences of the tiles remained constant. All sequences used for the 4HX system are exactly as shown in a-h.

Fluorescence Data

(a) 4-Helix Design #1

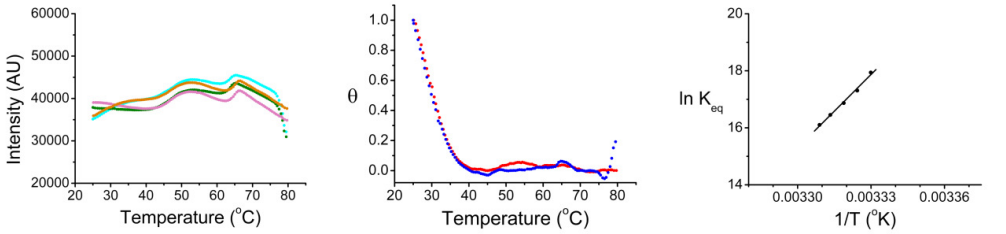

(b) 4-Helix Design #2

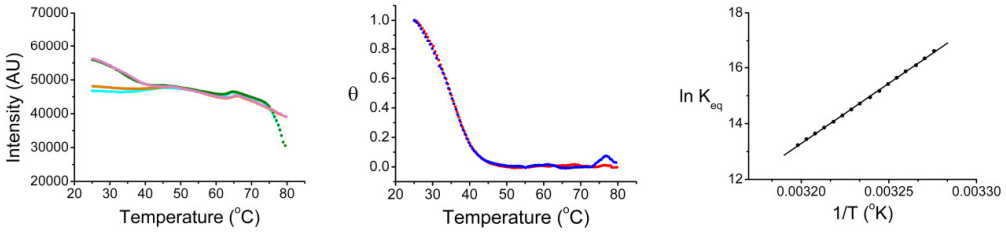

(c) 4-Helix Design #3

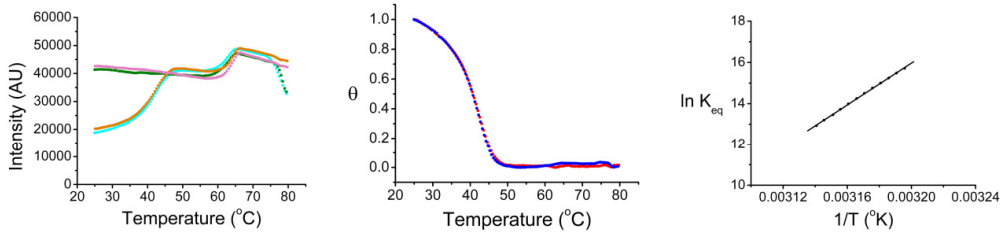

(d) 4-Helix Design #4

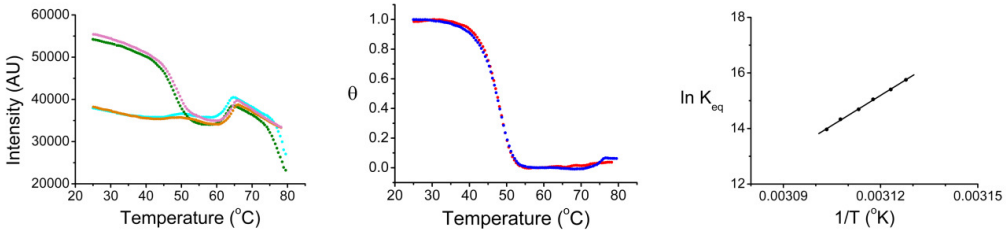

(e) 4-Helix Design #5

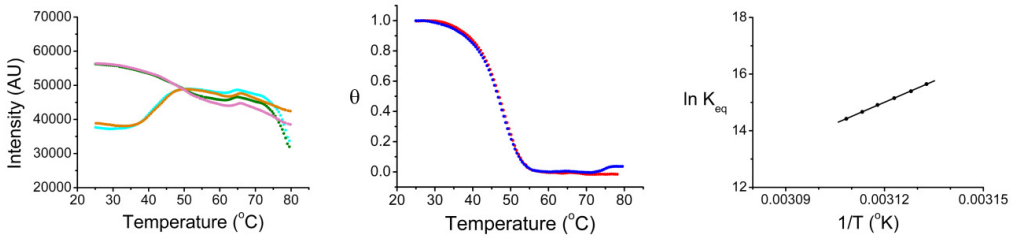

(f) 4-Helix Design #6

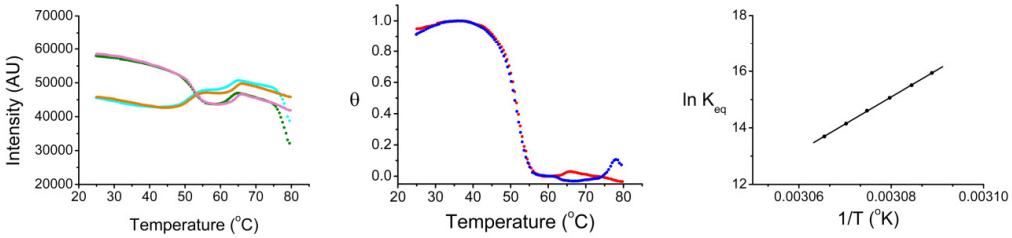

(g) 4-Helix Design #7

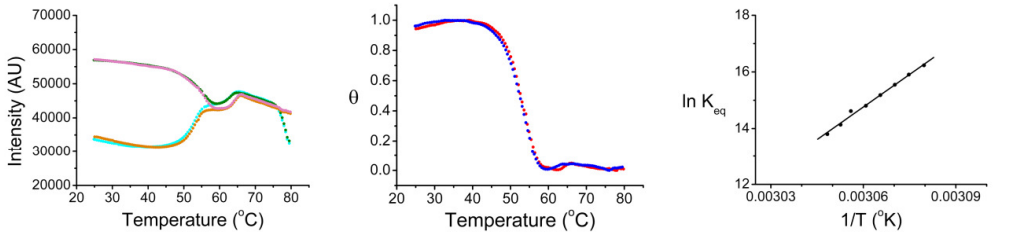

(h) 4-Helix Design #8

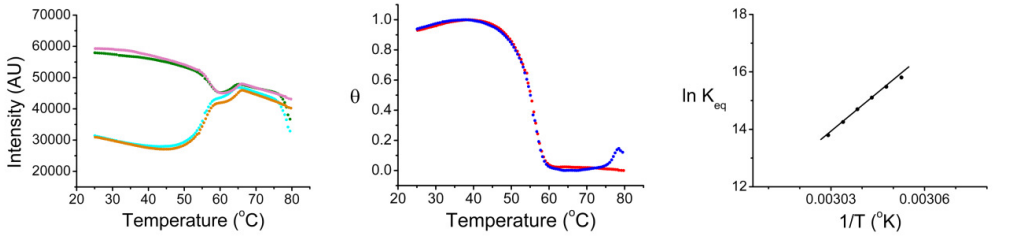

Figure S3. Raw data (left panels), normalized FRET thermal curves (center panels) and Arrhenius plots (right panels) obtained for 4HX dimers at 0.5 μM. From (a) to (h) the raw data, normalized FRET curves, and Arrhenius plots of 4HX designs 1-8 are shown. Left panels: the intensity of fluorescence emission of fluorescein (at 522 nm) is plotted against temperature in the 25 to 80 ºC range. The heating and cooling profiles of the donor-acceptor labeled samples are shown in orange and cyan, respectively. The heating and cooling profiles of the reference sample containing the donor only are shown in magenta and olive, respectively. Comparison of the thermal profiles allowed the determination of the normalized FRET efficiency curves illustrated in the center panels. Center panels: the normalized FRET efficiency is plotted against temperature in the 25 to 80 ºC range. The heating and cooling profiles are shown in red and blue, respectively. All the dimers analyzed showed a reversible and cooperative thermal transition which enabled the determination of thermodynamic parameters via application of the Van't Hoff law. Right panels: the application of the Van't Hoff law allowed for the creation of Arrhenius plots (ln K_{eq} vs 1/T). From the slope and intercept of the linear regression (shown in black) the enthalpy and entropy change for the assembly process was obtained.

(a) 6-Helix Design 2

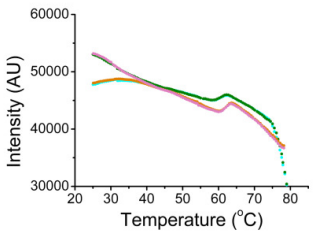

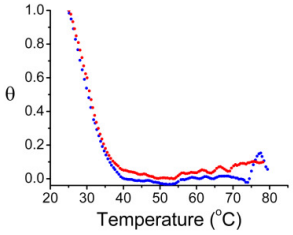

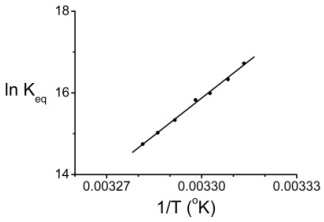

(b) 6-Helix Design 2,3

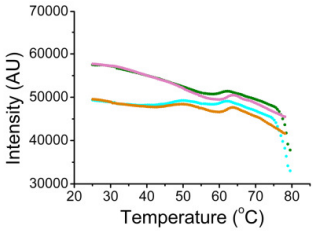

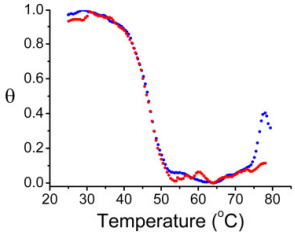

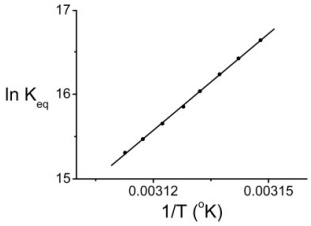

(c) 6-Helix Design 2,3,4

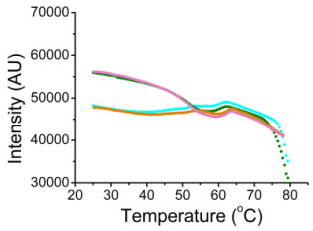

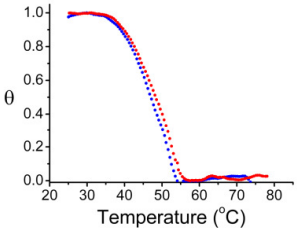

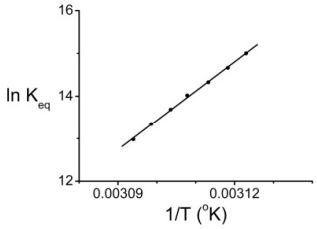

(d) 6-Helix Design 2,3,4,5

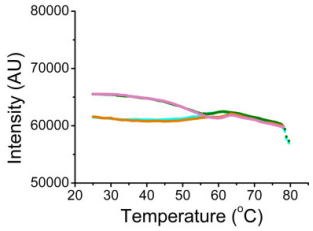

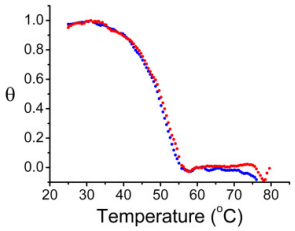

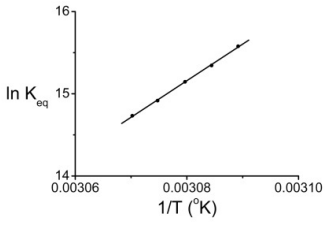

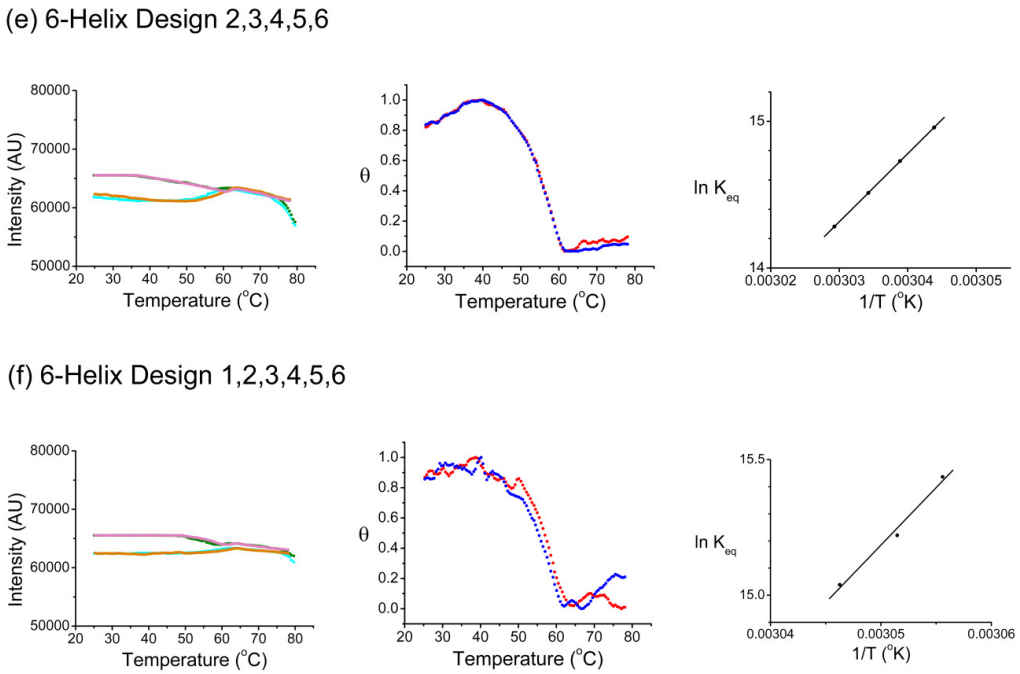

Figure S4. Raw data (left panels), normalized FRET thermal curves (center panels) and Arrhenius plots (right panels) obtained for 6HX dimers at 0.5 μM. From (a) to (f) the raw data, normalized FRET curves, and Arrhenius plots of representative 6HX designs denoted by the helix number(s) of sticky end associations. Left panels: the intensity of fluorescence emission of fluorescein (at 522 nm) is plotted against temperature in the 25 to 80 ºC range. The heating and cooling profiles of the donor-acceptor labeled samples are shown in olive and cyan, respectively. The heating and cooling profiles of the reference sample containing the donor only are shown in magenta and orange, respectively. Comparison of the thermal profiles allowed the determination of the normalized FRET efficiency curves illustrated in the center panels. Center panels: the normalized FRET efficiency is plotted against temperature in the 25 to 80 ºC range. The heating and cooling profiles are shown in red and blue, respectively. All the dimers analyzed showed a reversible and cooperative thermal transition which enabled the determination of thermodynamic parameters via application of the Van't Hoff law. Right panels: the application of the Van't Hoff law allowed for the creation of Arrhenius plots (ln K_{eq} vs 1/T). From the slope and intercept of the linear regression (shown in black) the enthalpy and entropy change for the assembly process was obtained.

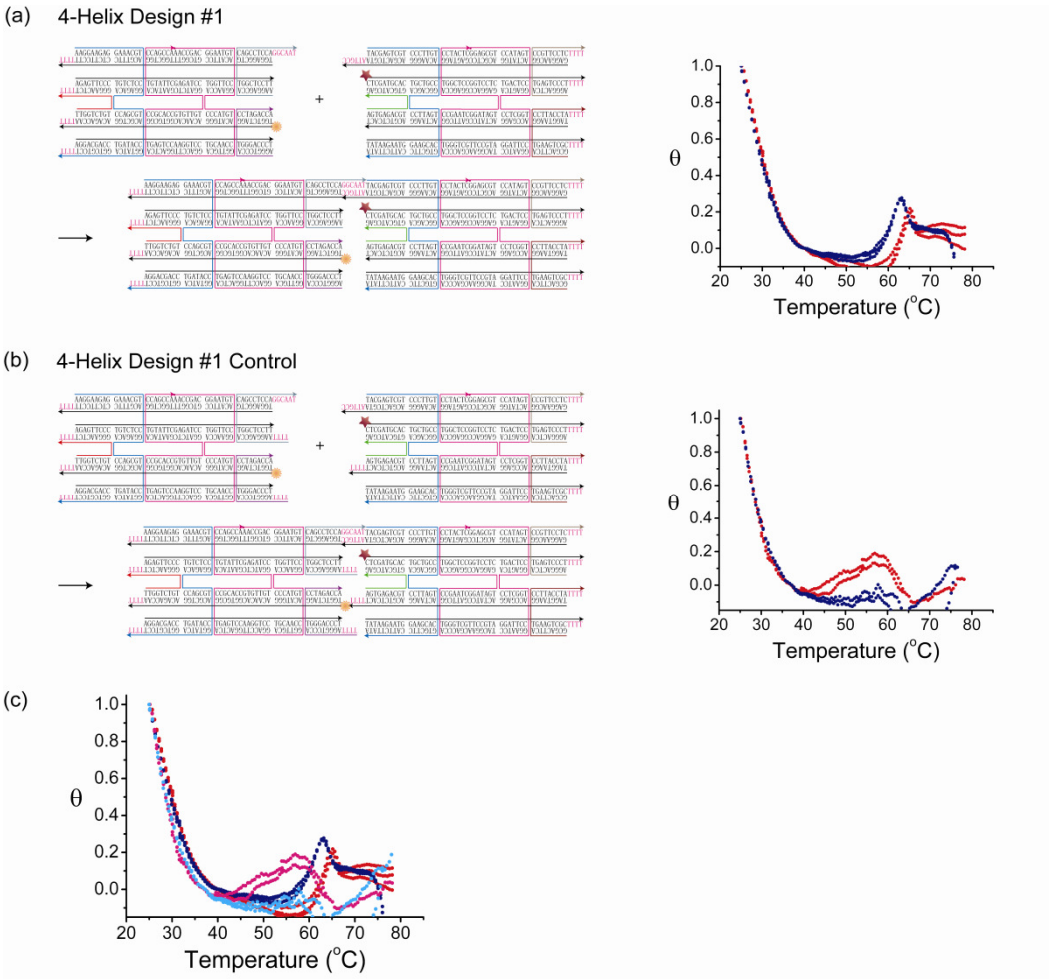

Figure S5. Control experiment to determine the contribution of stacking interactions between tiles to the inter-tile association measurements. The left panel in (a) schematically illustrates the dissociated individual tiles and associated dimer superstructure for 4-Helix Design #1. The left panel in (b) schematically illustrates the dissociated individual tiles and associated dimer superstructure for 4-Helix Design #1 Control, where one single strand from each of helices 2, 3, and 4 have been modified with a poly T sequence to prevent stacking interactions between the left and right side tiles. The right panels in (a) and (b) are the corresponding normalized FRET thermal curves for 4-Helix Design #1 and 4-Helix Design #1 Control, respectively. The normalized FRET efficiency is plotted against temperature in the 25 to 80 ºC range. The heating and cooling profiles are shown in red and blue, respectively. The graph in (c) is a superimposition of the FRET thermal curves for the 4-Helix Design #1 and 4-Helix Design #1 Control. The heating and cooling profiles of 4-Helix Design #1 are shown in red and blue, respectively. The heating and cooling profiles of 4-Helix Design #1 Control are shown in magenta and cyan, respectively. The curves for both designs show no considerable difference, indicating no significant contribution to the association between the tiles as a result of stacking interactions.

Structural Characterization

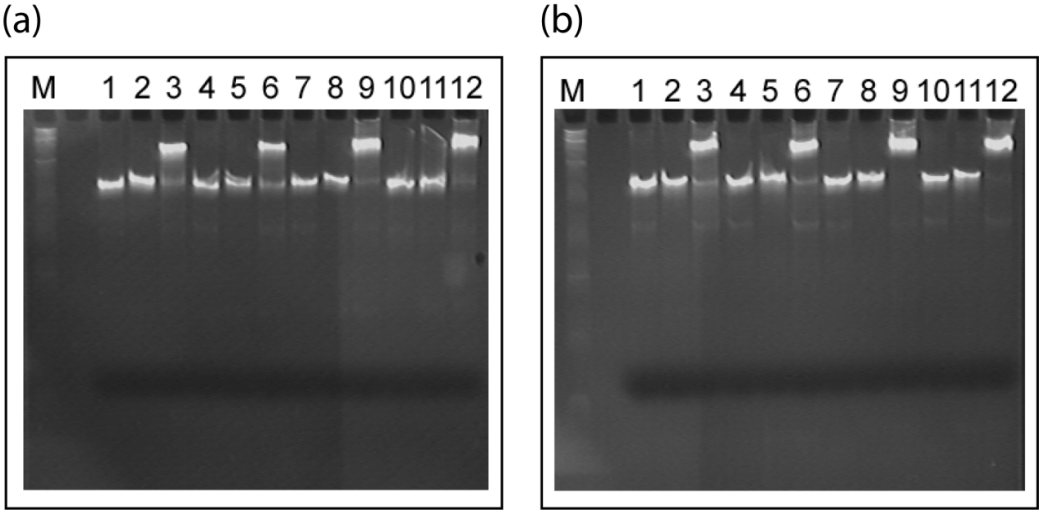

Figure S6. Characterization of the self-assembled individual 4HX tiles as well as the final superstructure was demonstrated by non-denaturing PAGE (8% PAGE in 1X TAE Mg buffer running conditions: 150V, 20ºC for 5 hours, ethidium bromide stained). In both gels, M contains a 10 bp DNA ladder size marker. The gel in (a) shows 4HX constructs 1-4. From lanes 1-12 the following individual tiles and dimer superstructures were loaded: 4HX design #1 tile A, tile B, and dimer; 4HX design #2 tile A, tile B, and dimer, 4HX design #3 tile A, tile B, and dimer; and 4HX design #4 tile A, tile B, and dimer. All individual and dimer tile structures showed one major band, with individual tiles migrating faster through the gel than dimer tile structures. The gel in (b) shows 4HX constructs 5-8. From lanes 1-12 the following individual tiles and dimer superstructures were loaded: 4HX design #5 tile A, tile B, and dimer; 4HX design #6 tile A, tile B, and dimer, 4HX design #7 tile A, tile B, and dimer; and 4HX design #8 tile A, tile B, and dimer. All individual and dimer tile structures showed one major band, with individual tiles migrating faster through the gel than dimer tile structures.

APPENDIX B

SUPPLEMENTAL INFORMATION FOR CHAPTER 3

Supplemental Information

DNA Nanostructures as Models for Evaluating the Role of Enthalpy and Entropy in Polyvalent Binding *

Jeanette Nangreave, Hao Yan*, Yan Liu*

Department of Chemistry & Biochemistry and the Biodesign Institute
Arizona State University, Tempe, AZ, 85287, USA

Materials and Methods

Self-assembly of DNA nanostructures: All DNA strands used for assembly of nanostructures were purchased from Integrated DNA Technologies, Inc. (www.idtdna.com) and purified by denaturing polyacrylamide gel electrophoresis (PAGE; 6-10% acrylamide in 1X TBE buffer: 89mM Tris base, 89 mM Boric acid, 2mM EDTA, pH 8.0) for the unmodified DNA oligomers or by HPLC for the dye labeled DNA oligomers. Assembly of the individual tiles as well as the final dimers were performed by mixing equimolar amounts of all the oligomers present in the structures at a final concentration of 0.3 μM for FRET experiments and 0.1 μM for gel assays, in 1x TAE Mg^2+ buffer (40 mM Tris base, 20mM Acetic acid, 2 mM EDTA·Na_2·$12H_2O$, 12.5 mM $(CH_3COO)_2Mg·4H_2O$). A-type tiles contained one oligomer with a Fluorescein dye modification and B-type tiles contained one oligomer with a TAMRA dye modification. For FRET experiments self-assembly of nanostructures occurred during the spectroscopic measurement process; the oligomer mixtures were heated at 80ºC for 5 minutes and cooled from 80ºC down to 25ºC (~ -0.1 ºC/min) using an automated real-time PCR thermocycler (Mx3005P, Strategene). The formation of self-assembled individual tiles as well as the final dimers were also verified by non-denaturing PAGE (7% acrylamide in 1x TAE Mg buffer (40 mM Tris base, 20mM Acetic acid, 2 mM EDTA·Na_2·$12H_2O$, 12.5 mM $(CH_3COO)_2Mg·4H_2O$)) at 200V, 20ºC for ~4 hours. For competitive displacement experiments the preassembled nanostructures was prepared by heating the oligomer mixtures at 90ºC and cooling to 4ºC over 12 hours using an automated PCR thermocycler (Mastercycler Pro, Eppendorf).

FRET experiments: The fluorescence thermal curves were measured in 8 well optical tube strips using a MX3005P real-time thermocycler (Strategene). After mixing equimolar amounts of all oligomers present in the nanostructures (0.3 μM final concentrations in 1xTAE.Mg buffer), 20 μL of each sample was pipetted into Strategene optical tube strips in triplicates and closed with Strategene optical caps. The samples were heated to 80ºC for 5 minutes, and upon excitation at 492 nm, the fluorescence emission of fluorescein (522 nm) was monitored while the temperature was reduced from 80ºC to 25ºC with a temperature gradient of -0.1ºC/min. Heating cycles were performed in the same manner: after one cooling cycle the samples were held at 25ºC for 10 minutes and upon excitation at 492

nm, the fluorescence emission was monitored while the temperature was increased from 25ºC to 80ºC with a temperature gradient of +0.1ºC/min. All experiments were repeated at least twice in triplicates to ensure reproducibility. For all the nanostructures investigated, two samples were prepared with identical experimental conditions: One sample (A^DB^A) contained the donor (fluorescein) on Tile A and the acceptor (TAMRA) on Tile B, while the second sample (A^DB) contained only the donor fluorophore on Tile A and corresponding unlabeled oligomer on Tile B. This scheme allowed for the measurement of the decrease in donor emission resulting from energy transfer to the acceptor in order to calculate the FRET efficiency. This method also allowed for the variations in the donor's fluorescence as a result of changes in temperature to be taken into account. Results of all FRET experiments can be found in SI Figure 2.

Competitive displacement: Initially, fluorophore labeled A^DB^A dimers were assembled with a 0.1 μM concentration as previously described, divided into aliquots and placed into individual PCR tubes. Unlabeled, type B tiles (displacement tiles) that contain complementary sticky ends to that of A tile were also assembled with final concentrations of 0.02 μM and 0.2 μM. Non-denaturing PAGE gels (7% acrylamide in 1X TAE Mg buffer) were prepared prior to adding the displacement tiles to the preassembled dimers. The competitive displacement experiments were performed as follows: a specific volume of displacement tile was added to each preassembled dimer aliquot, with the actual volumes corresponding to particular molar ratios of replacement tile to preassembled dimer. The following molar ratios of secondary tile to preassembled dimer were investigated: 0.1:1, 0.2:1, 0.35:1, 0.5:1, 0.7:1, 1:1, 1.5:1, 2:1, 3:1, 4:1, and 5:1 (lanes 4-14, respectively, in Figure 3.5 and SI Figures 3-5). Each mixture was then diluted to the same volume to maintain a constant dimer concentration for all samples and the competitive displacement reaction was allowed to proceed at constant temperature (5 ºC, 10 ºC, 15 ºC, and 20 ºC). After the elapsed time (ranging from 2 hours to 300 hours to allow certain reactions to reach equilibrium) the sample mixtures were analyzed by non-denaturing PAGE (200V, for 3.0-4.5 hours) at the same temperature as the corresponding displacement reaction. The mobility of the various structures in the PAGE gels could be followed via the fluorophore labeled oligomers contained within the individual tiles. In order to visualize the fluorescently labeled tiles the gels were imaged using a Typhoon Trio Variable Mode Imager (GE Healthcare) by scanning at 488 nm and 532 nm and collecting the fluorescence emission from the two fluorophores (fluorescein, 520 nm and Tamra, 583nm). The intensity of each band was determined using ImageQuant TL gel analysis software (Amersham Biosciences).

Thermodynamic characterization

After raw data was collected from FRET experiments, the efficiency of energy transfer (E) was determined at each temperature according to the following equation:

$$E(T) = 1 - \frac{I_{DA}(T)}{I_D(T)} \qquad [1],$$

where I_{DA} and I_D are, respectively, the fluorescence intensities of the FRET donor (Fluorescein) in the presence and absence of the FRET acceptor (TAMRA). Assuming the change in the fluorescence intensity of the donor is proportional to the formation of dimers containing the FRET pair, and that the system reaches equilibrium at each temperature as a result of the slow temperature gradient, the fraction of assembled dimer structures at any given temperature $\theta(T)$ is obtained by normalization of FRET efficiency as a function of temperature:

$$\theta(T) = \frac{E(T) - E_{\min}}{E_{\max} - E_{\min}} \qquad [2],$$

where $E_{\min}$ represents the minimum FRET efficiency that occurs when the dimer is completely dissociated, and $E_{\max}$ represents the maximum FRET efficiency that occurs when the dimer is completely assembled. $\theta(T)$ gives information about the equilibrium shift of the reaction of A+B $\Leftrightarrow$ AB as a function of temperature: at $E_{\max}$ all DNA tiles are fully assembled to form AB dimers, and therefore $\theta = 1$. In contrast, at $E_{\min}$ all DNA strands are completely dissociated and therefore $\theta = 0$.

The intensity of fluorescence emission of the FRET donor in the presence and absence of the acceptor, I_{DA} and I_D, was obtained for each pair of samples. The raw data was plotted against temperature in the 25ºC to 80ºC range and the heating and cooling profiles were superimposed (a typical sample is shown in Figure 3.3a in the main text). $E_{\min}$ and $E_{\max}$ are directly determined from E(T) data, obtained by equation [1], by averaging the lowest and highest range data from multiple samples. $E_{\min}$ and $E_{\max}$ are not temperature dependent: $E_{\min}$ (high temperature) is close to 0 for all cases, $E_{\max}$ is in the range of 0.65-0.8, depending on the nature of the sample. The lowest $E_{\max}$ values are mostly for the dimers with lower melting temperatures, which is likely the result of instrumental limitations in that we did not reach 100% formation of the dimer at the lowest temperature available (25°C). After determining the assembled fraction of dimers at each temperature using equations [1] and [2], θ was plotted against temperature with the heating and cooling profiles superimposed (Figure 3.3b). It is observed that the heating and cooling profiles for an individual construct followed each other closely with negligible hysteresis, especially for the normalized data (Figure 3.3b), indicating the reversibility of the dimer formation and dissociation processes.

The raw fluorescence intensity data (Figure 3.3a) reflects the assembly process for a typical sample. During the assembly process (cooling from 80°C to 25°C), the $A^{Donor}B^{Acceptor}$ constructs exhibited a gradual increase in the donor emission while cooling, with a sharp drop at ~42 °C. The $A^{Donor}B$ reference sample also exhibited a minor and gradual increase in the donor emission, with a slightly steeper increase at ~42 ºC. For both samples, the change in donor emission at ~42 °C corresponds to the formation of the dimer superstructure. The

significant drop in donor emission for the $A^{Donor}B^{Acceptor}$ sample is a result of efficient energy transfer to the acceptor when the FRET pair was brought into close proximity upon dimer formation. The slight increase for the $A^{Donor}B$ sample is most likely due to a change in the local environment of the dye upon dimer formation, which affects its emission.

The subtraction of the two curves and normalization according to equations [1] and [2] results in the curves shown in Figure 3.3b, which exhibit a single transition that is directly related to the dimer formation.

The transition temperature (melting temperature) was obtained by fitting the first derivative of θ vs. temperature with a Gaussian function,

$$Y = Y_0 + \frac{A}{w\sqrt{\pi/2}} e^{-2\left(\frac{T-T_m}{w}\right)^2} \qquad [3],$$

where T_m is the midpoint of the transition temperature, and w is ~ 0.849 the full width of the peak at half height (Figure 3.3c). All the constructs analyzed showed a reversible thermal transition, allowing the application of the van't Hoff law.

For van't Hoff analysis, the variation of the equilibrium constant (K_{eq}) with temperature is used to obtain the enthalpy and entropy changes of the complex formation. The equilibrium constant of dimer formation can be expressed as a function of the assembled fraction of dimers at equilibrium:

$$K_{eq} = \frac{\theta}{C_0(1-\theta)^2} \qquad [4],$$

where C_0 is the molar concentration of the individual tiles in the mixture, and θ is the assembled fraction of the dimer structure at equilibrium assuming a two-state transition. The following equation describes K_{eq} as a function of temperature:

$$\ln K_{eq} = \frac{-\Delta H}{RT} + \frac{\Delta S}{R} \qquad [5],$$

where ΔH is the enthalpy change and ΔS is the entropy change. Plots of $ln\ K_{eq}$ vs $1/T$ in the temperature range of the transitions were linear, indicating that ΔH and ΔS are temperature independent (Figure 3.3d). The van't Hoff enthalpy and entropy changes for the reversible thermal transitions allowed the calculation of changes in free energy for the assembly process using the Gibbs equation:

$$\Delta G = \Delta H - T\Delta S \qquad [6],$$

where T is 298 K (25 °C).

Figures

The design and components of the DNA tile dimers studied in this report are shown in SI Figure S1, including the sequences of the DNA strands used. FRET thermal data analysis is detailed for each sample in SI Figure S2, panels A-J. The thermodynamic constants of dimer formation obtained from the data analysis are summarized in Table 3.1 and Table 3.2 in the main text. The competitive displacement reactions at temperatures ranging from 5ºC to 20ºC were analyzed by native gel electrophoresis and the gel images are shown in duplicate in SI Figures S3-18.

Name	Tile B	Tile A
J	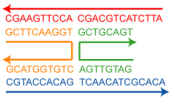	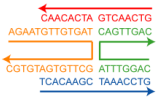
2T Mesojunction	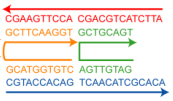	
4T Mesojunction	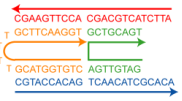	
6T Mesojunction	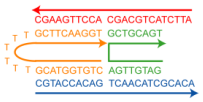	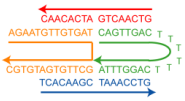
4T Tethered J	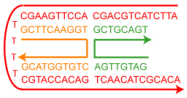	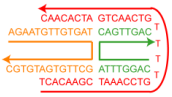
8T Tethered J		
12T Tethered J	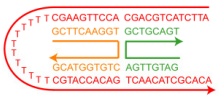	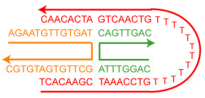
DX (158 bp dimer)	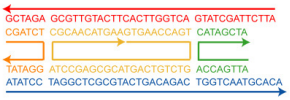	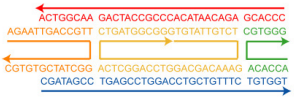
DX (166 bp dimer)	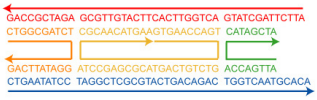	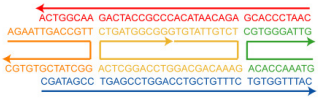
DX (182 bp dimer)	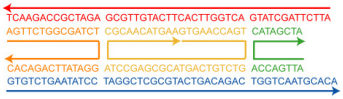	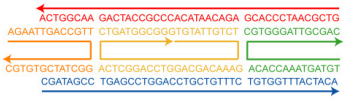

Figure S1. Design of all DNA tiles used in the study, with the corresponding sequences of the constituent oligonucleotides.

(A) Flexible Dimer (J Tile A/J Tile B)

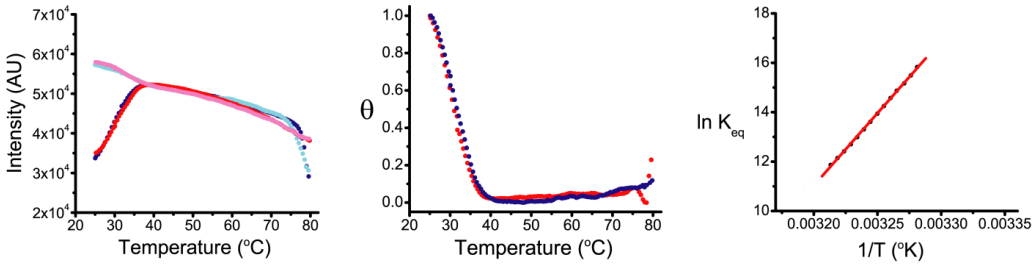

(B) Semi-rigid Dimer (DX Tile A/J Tile B)

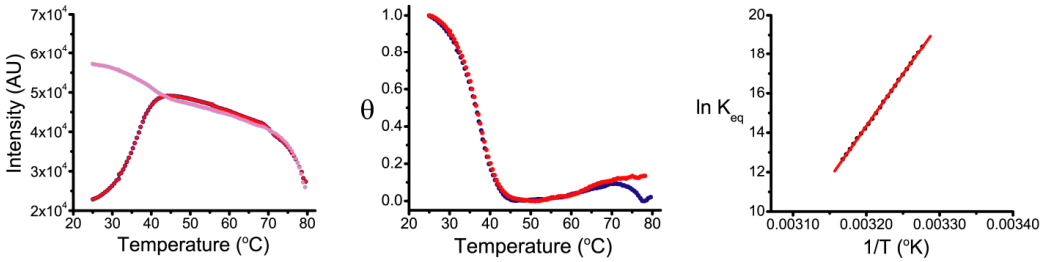

(C) 2T Mesojunction Dimer

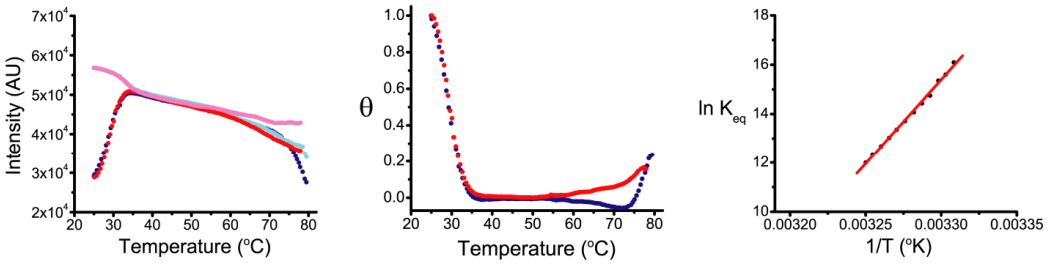

(D) 4T Mesojunction Dimer

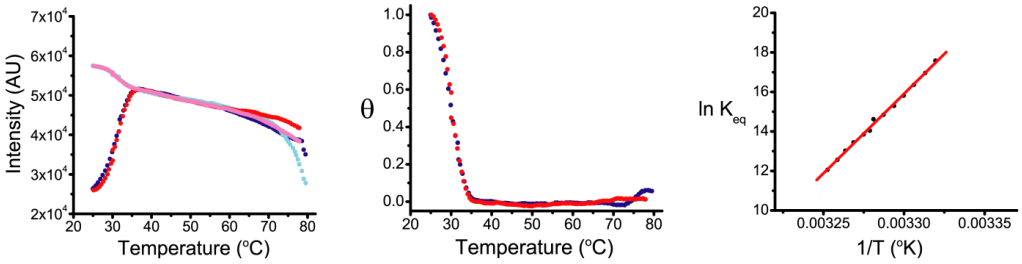

(E) 6T Mesojunction Dimer

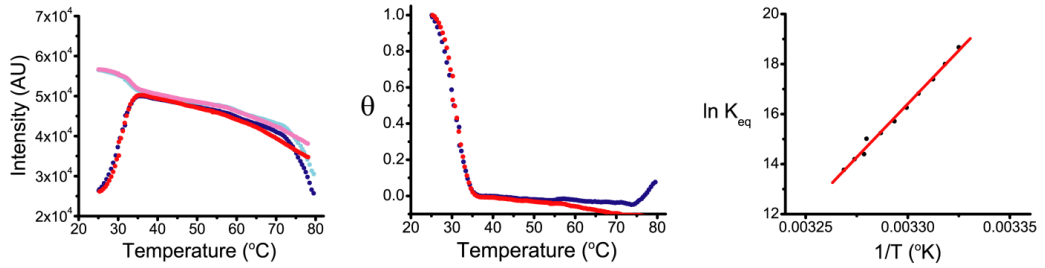

(F) 4T Tethered J Dimer

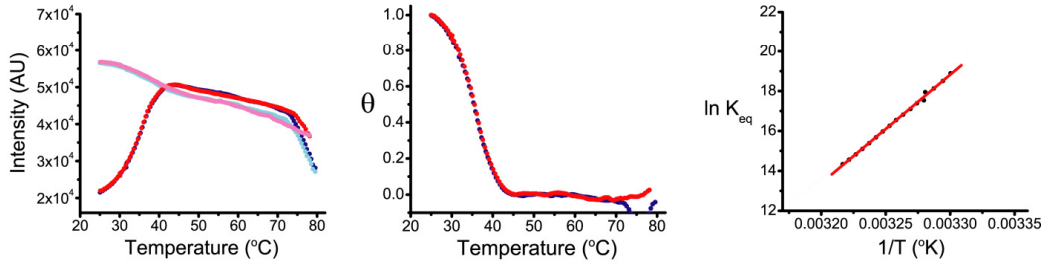

(G) 8T Tethered J Dimer

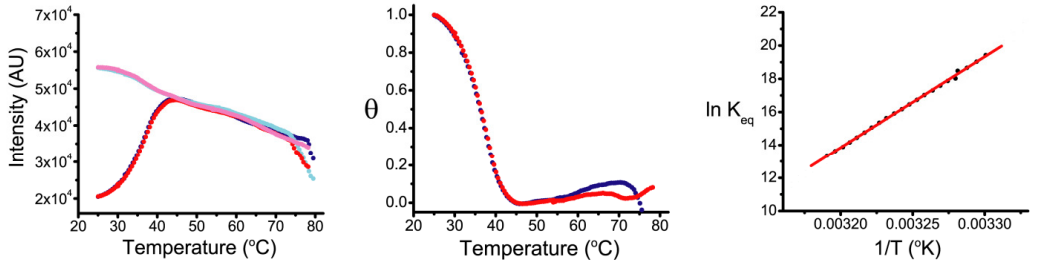

(H) 12T Tethered J Dimer

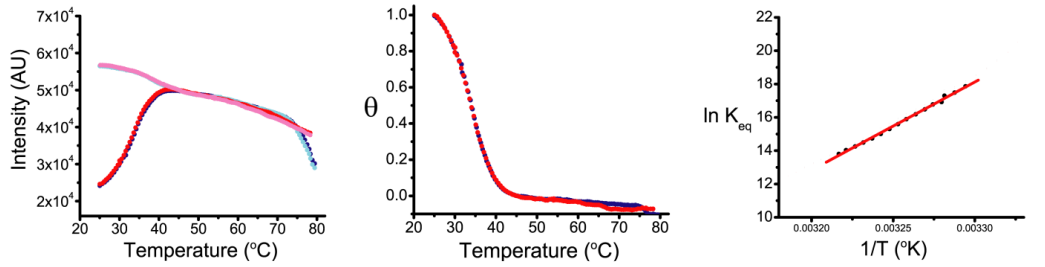

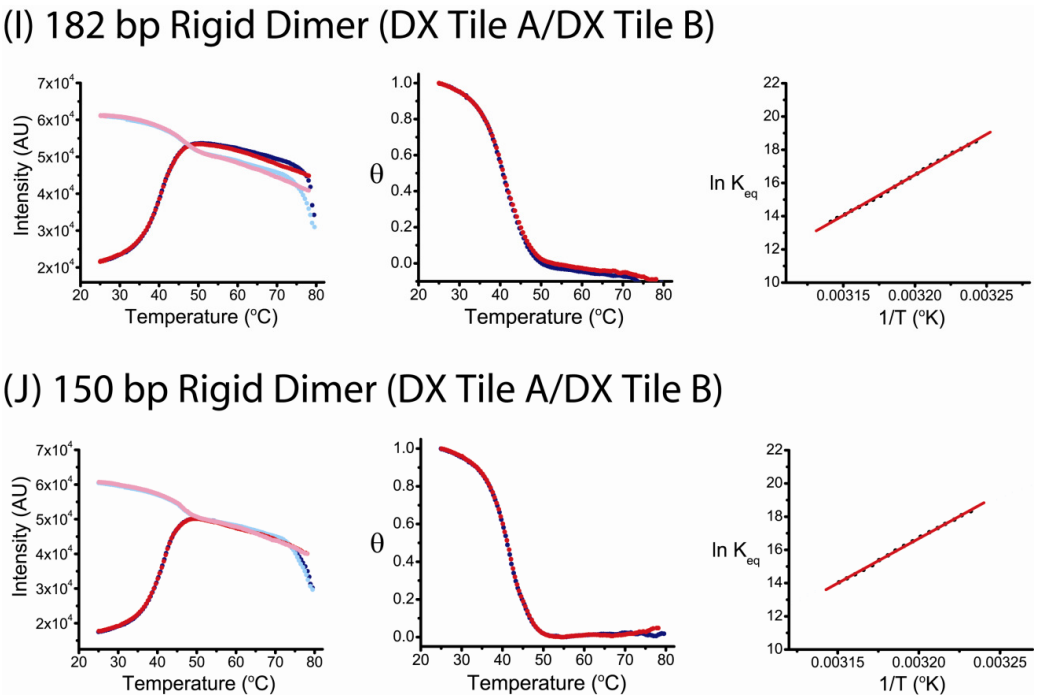

Figure S2. Results of the FRET thermal analysis, with samples identified above the graphs. The left panel corresponds to the raw data (fluorescence intensity vs. temperature) that is collected directly from the real-time PCR thermocycler, with the heating and cooling curves for the $A^{Donor}B^{Acceptor}$ samples in red and blue, respectively, and the heating and cooling curves for $A^{Donor}B$ samples in light magenta and cyan, respectively. The middle panel shows normalized FRET efficiency or fraction of dimer formation, θ, as a function of temperature. Profiles for both heating (red) and cooling (blue) are plotted together, exhibiting negligible hysteresis for dimers. The right panel contains van't Hoff plots with corresponding linear fit and is used to calculate the changes of enthalpy (ΔH), entropy (ΔS) and thereby the free energy change (ΔG).

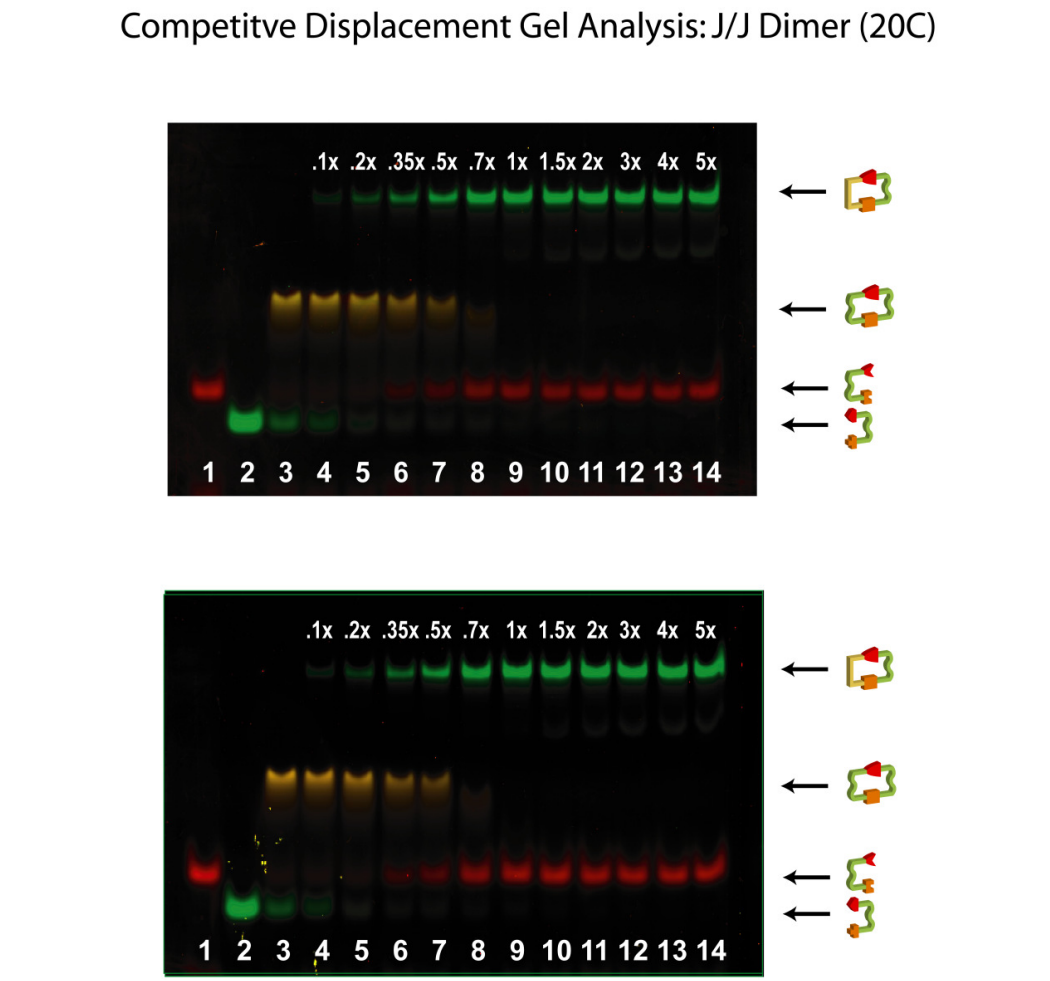

Figure S3. PAGE gel results of the competitive displacement experiments corresponding to the reaction illustrated in Figure 3.4a. Flexible J-A /J-B dimers are initially assembled, followed by the addition of rigid, DX-B as indicated. The displacement reaction was allowed to proceed for 2 hours at 20C. Two replicate trials are shown.

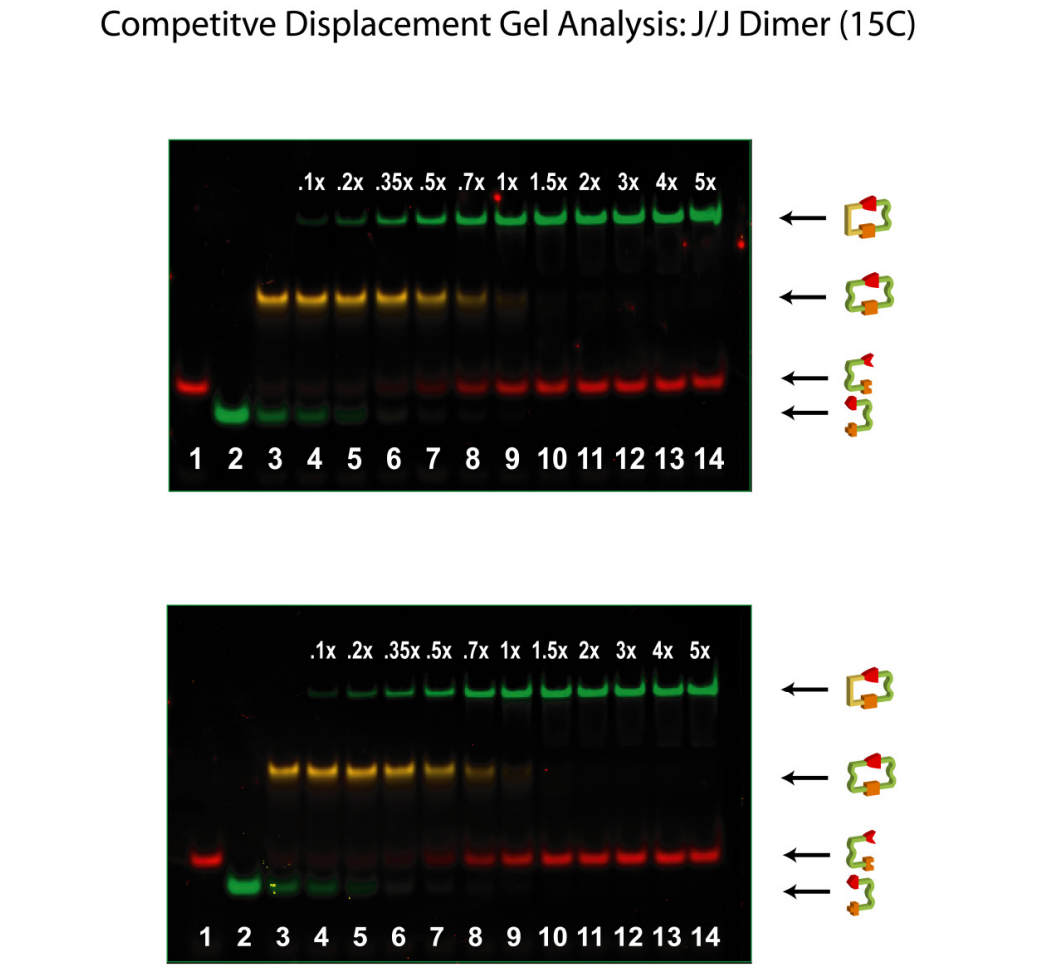

Figure S4. PAGE gel results of the competitive displacement experiments corresponding to the reaction illustrated in Figure 3.4a. Flexible J-A /J-B dimers are initially assembled, followed by the addition of rigid, DX-B as indicated. The displacement reaction was allowed to proceed for 2 hours at 15C. Two replicate trials are shown.

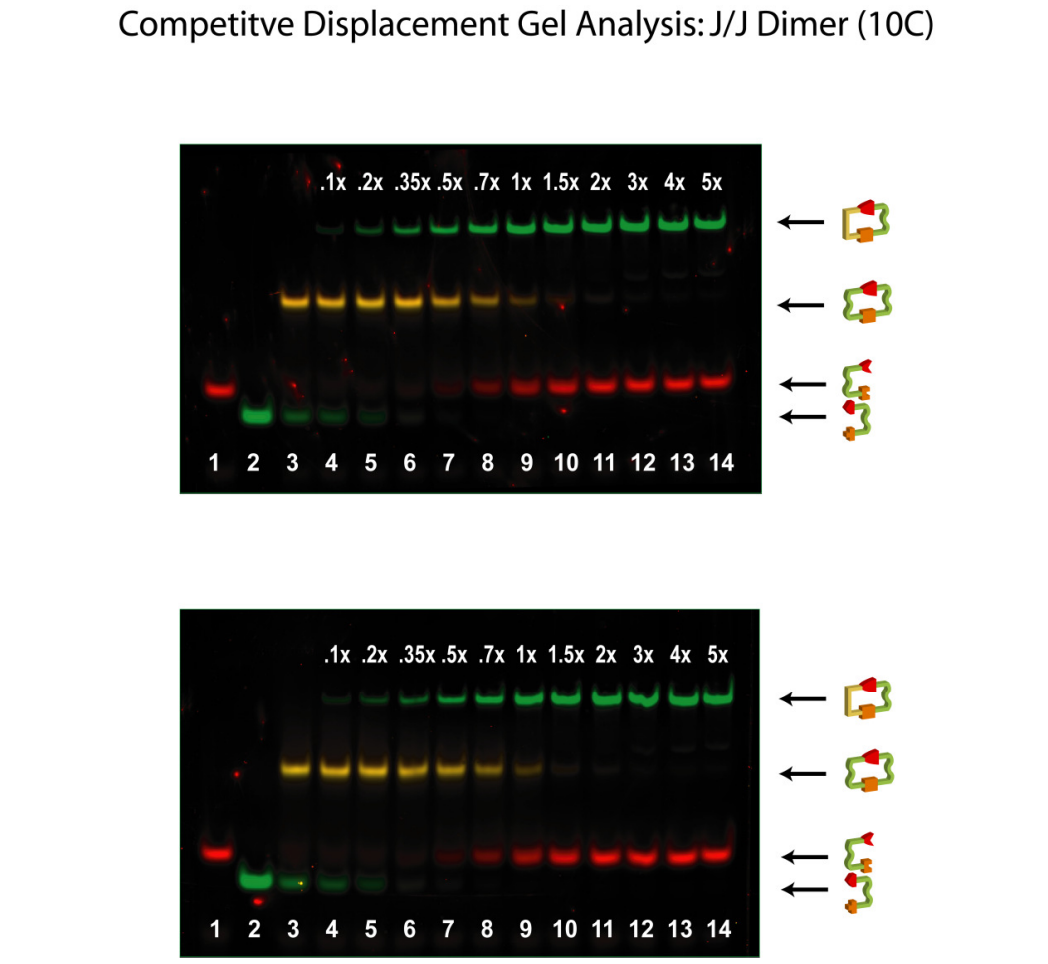

Figure S5. PAGE gel results of the competitive displacement experiments corresponding to the reaction illustrated in Figure 3.4a. Flexible J-A /J-B dimers are initially assembled, followed by the addition of rigid, DX-B as indicated. The displacement reaction was allowed to proceed for 2 hours at 10C. Two replicate trials are shown.

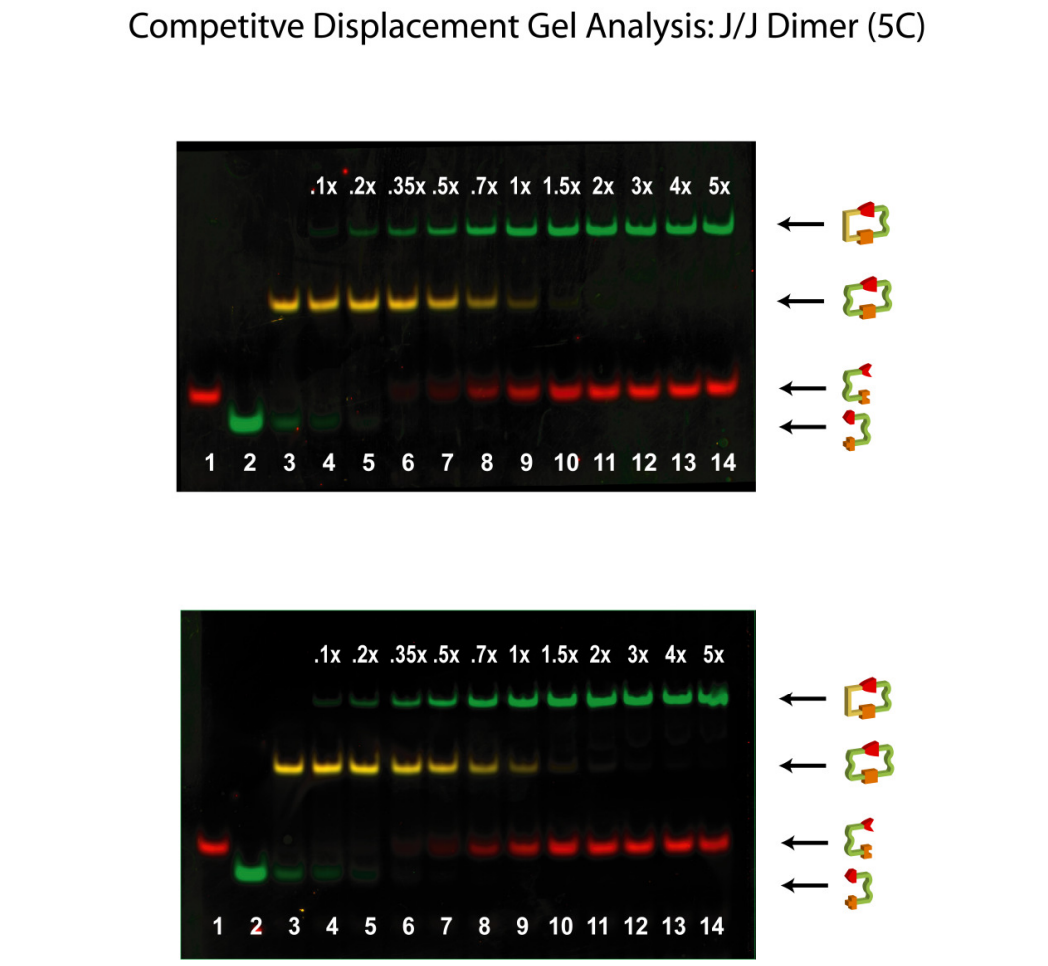

Figure S6. PAGE gel results of the competitive displacement experiments corresponding to the reaction illustrated in Figure 3.4a. Flexible J-A /J-B dimers are initially assembled, followed by the addition of rigid, DX-B as indicated. The displacement reaction was allowed to proceed for 2 hours at 5C. Two replicate trials are shown.

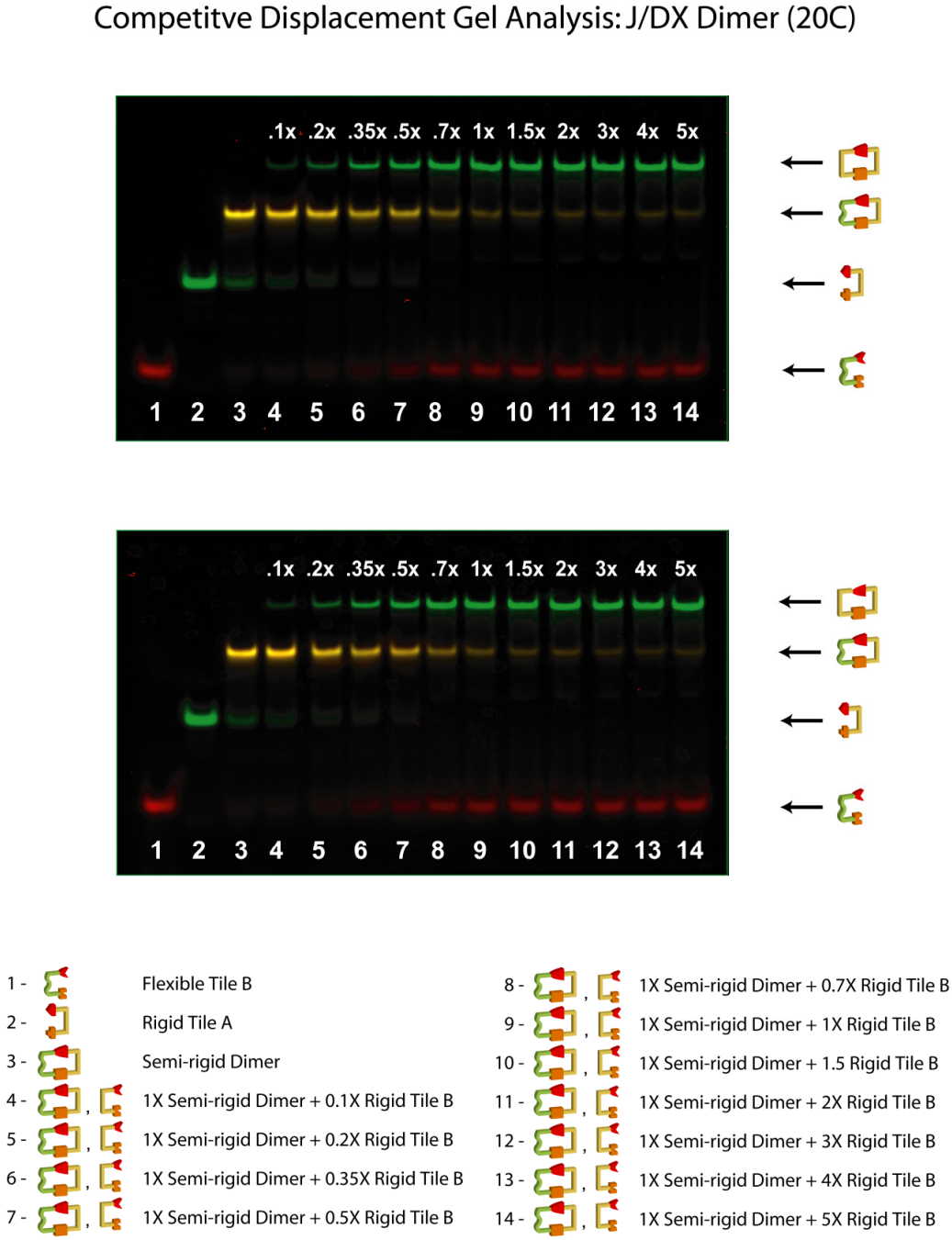

Figure S7. PAGE gel results of the competitive displacement experiments corresponding to the reaction illustrated in Figure 3.4b. Semi-rigid DX-A/J-B dimers are initially assembled, followed by the addition of rigid, DX-B as indicated. The displacement reaction was allowed to proceed for 2 hours at 20C. Two replicate trials are shown.

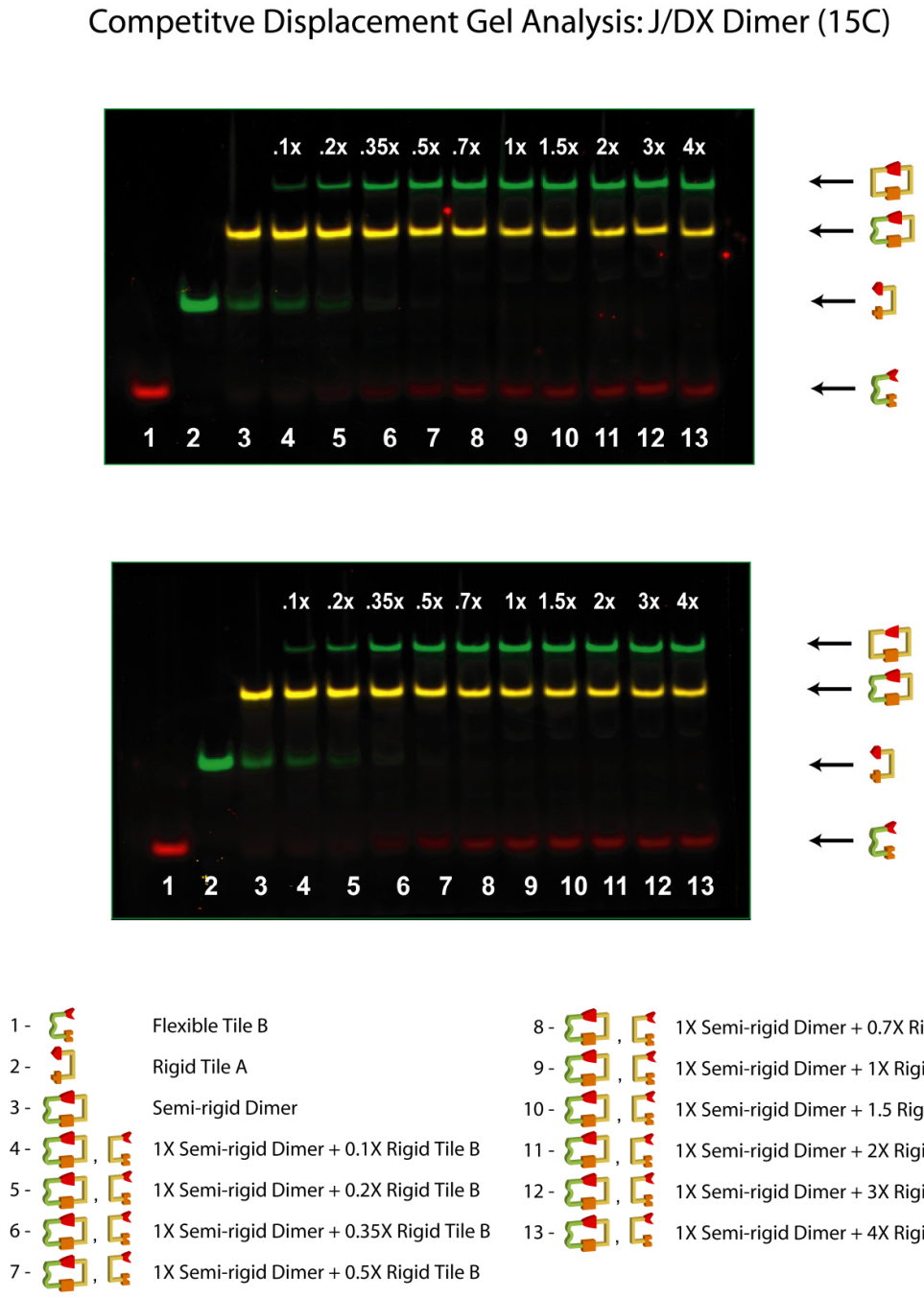

Figure S8. PAGE gel results of the competitive displacement experiments corresponding to the reaction illustrated in Figure 3.4b. Semi-rigid DX-A/J-B dimers are initially assembled, followed by the addition of rigid, DX-B as indicated. The displacement reaction was allowed to proceed for 2 hours at 15C. Two replicate trials are shown.

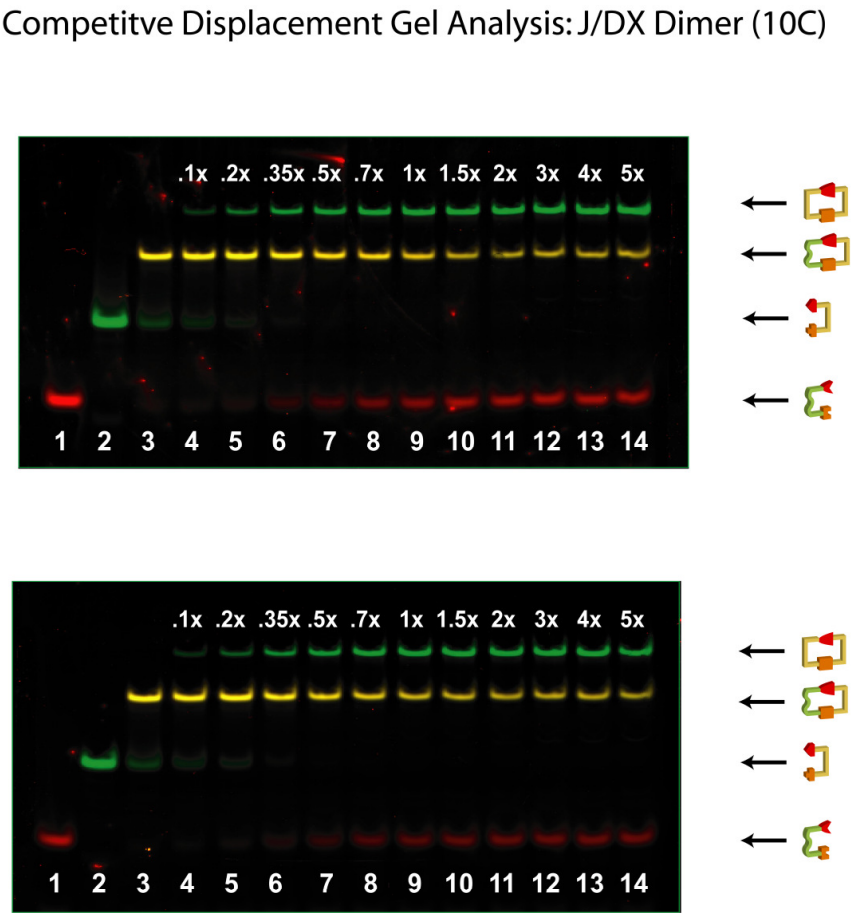

Figure S9. PAGE gel results of the competitive displacement experiments corresponding to the reaction illustrated in Figure 3.4b. Semi-rigid DX-A/J-B dimers are initially assembled, followed by the addition of rigid, DX-B as indicated. The displacement reaction was allowed to proceed for 2 hours at 10C. Two replicate trials are shown.

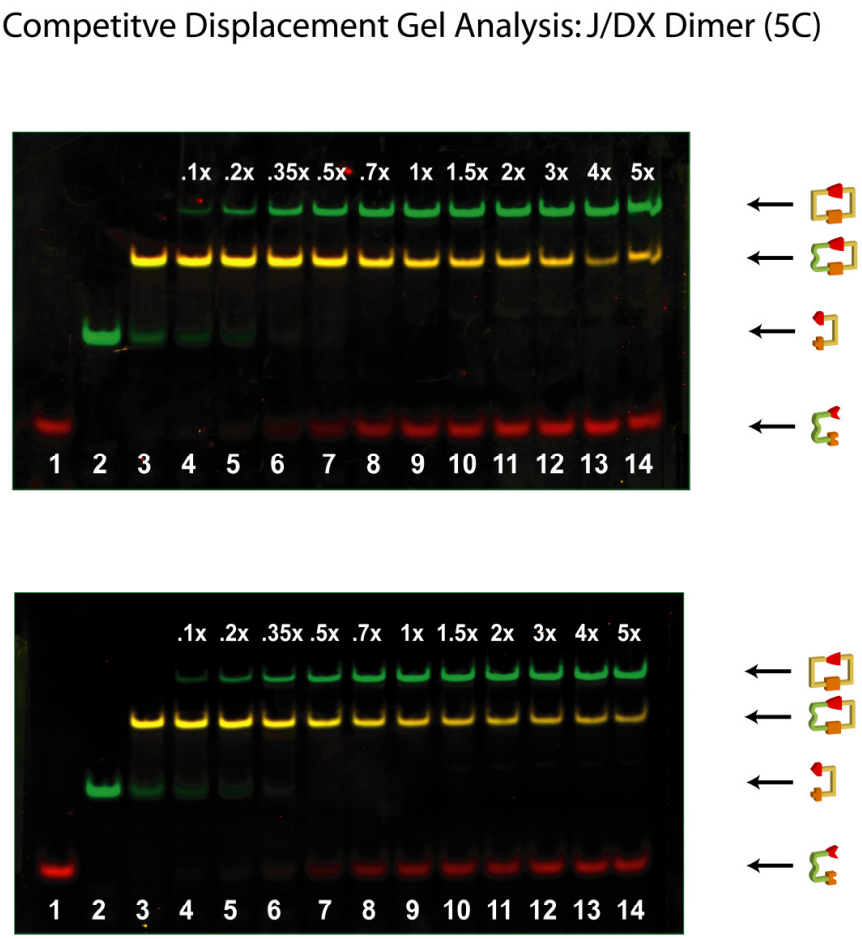

Figure S10. PAGE gel results of the competitive displacement experiments corresponding to the reaction illustrated in Figure 3.4b. Semi-rigid DX-A/J-B dimers are initially assembled, followed by the addition of rigid, DX-B as indicated. The displacement reaction was allowed to proceed for 2 hours at 5C. Two replicate trials are shown.

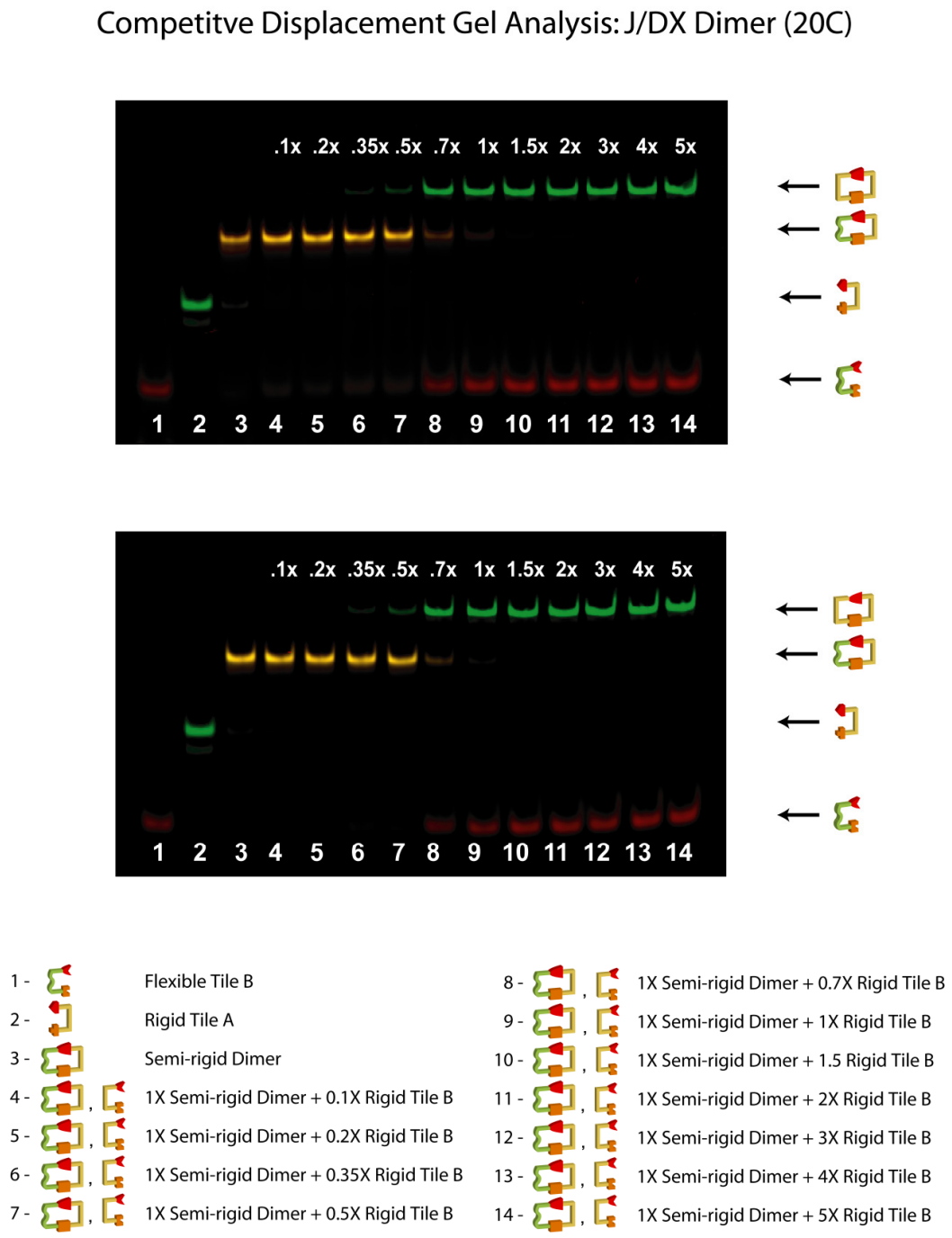

Figure S11. PAGE gel results of the competitive displacement experiments corresponding to the reaction illustrated in Figure 3.4b. Semi-rigid DX-A/J-B dimers are initially assembled, followed by the addition of rigid, DX-B as indicated. The displacement reaction was allowed to proceed for 300 hours at 20C. Two replicate trials are shown.

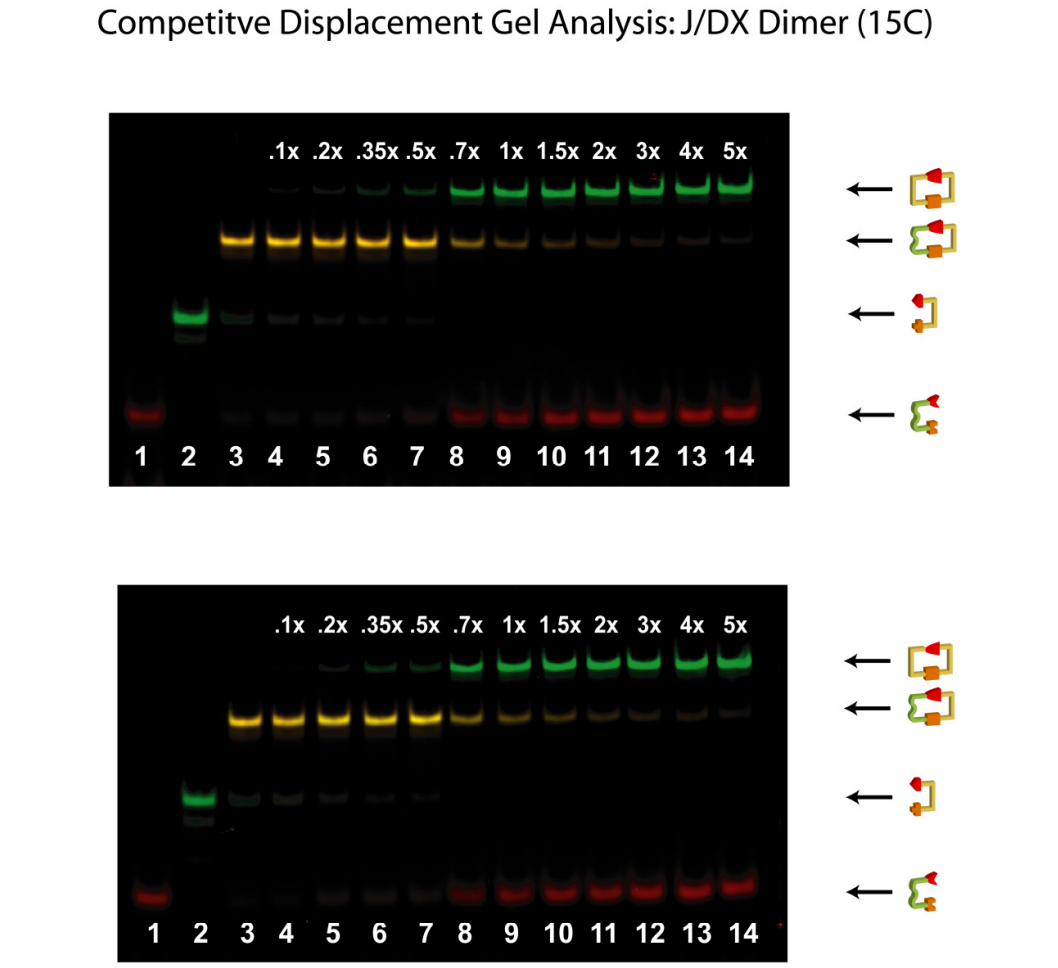

Figure S12. PAGE gel results of the competitive displacement experiments corresponding to the reaction illustrated in Figure 3.4b. Semi-rigid DX-A/J-B dimers are initially assembled, followed by the addition of rigid, DX-B as indicated. The displacement reaction was allowed to proceed for 300 hours at 15C. Two replicate trials are shown.

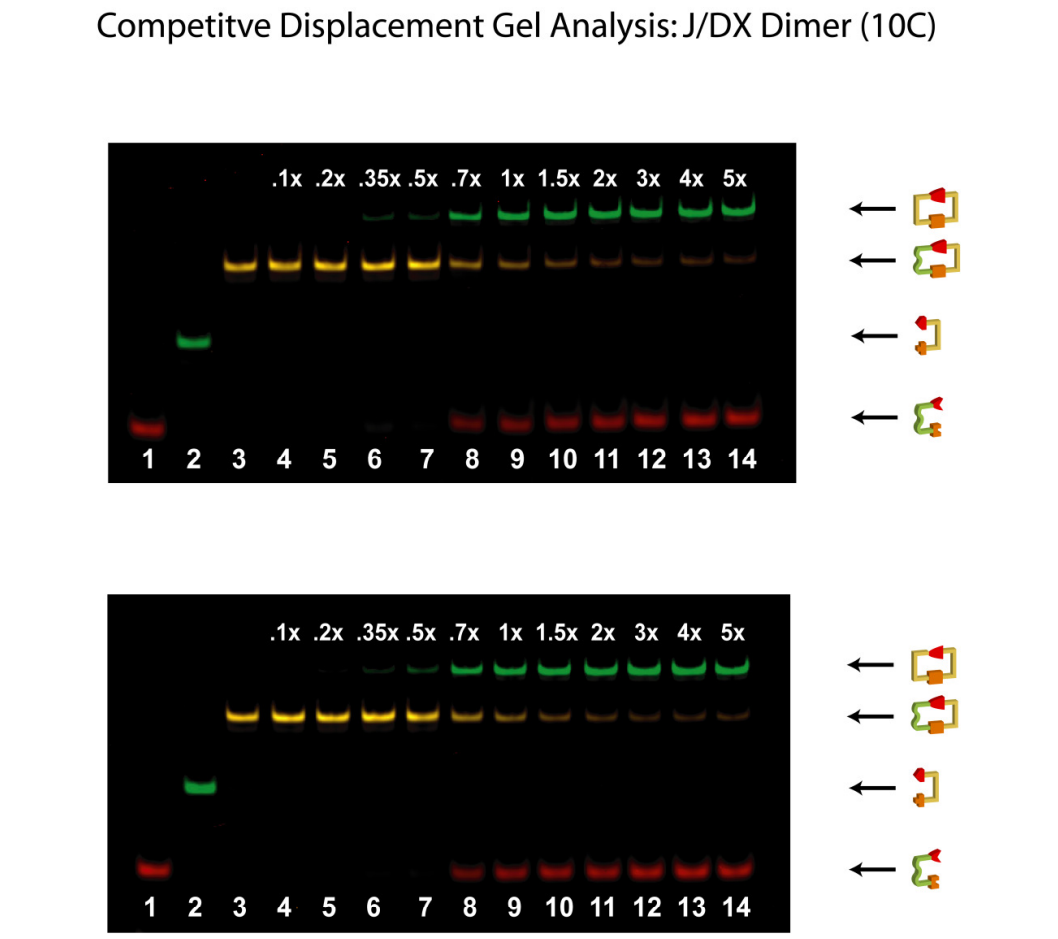

Figure S13. PAGE gel results of the competitive displacement experiments corresponding to the reaction illustrated in Figure 3.4b. Semi-rigid DX-A/J-B dimers are initially assembled, followed by the addition of rigid, DX-B as indicated. The displacement reaction was allowed to proceed for 300 hours at 10C. Two replicate trials are shown.

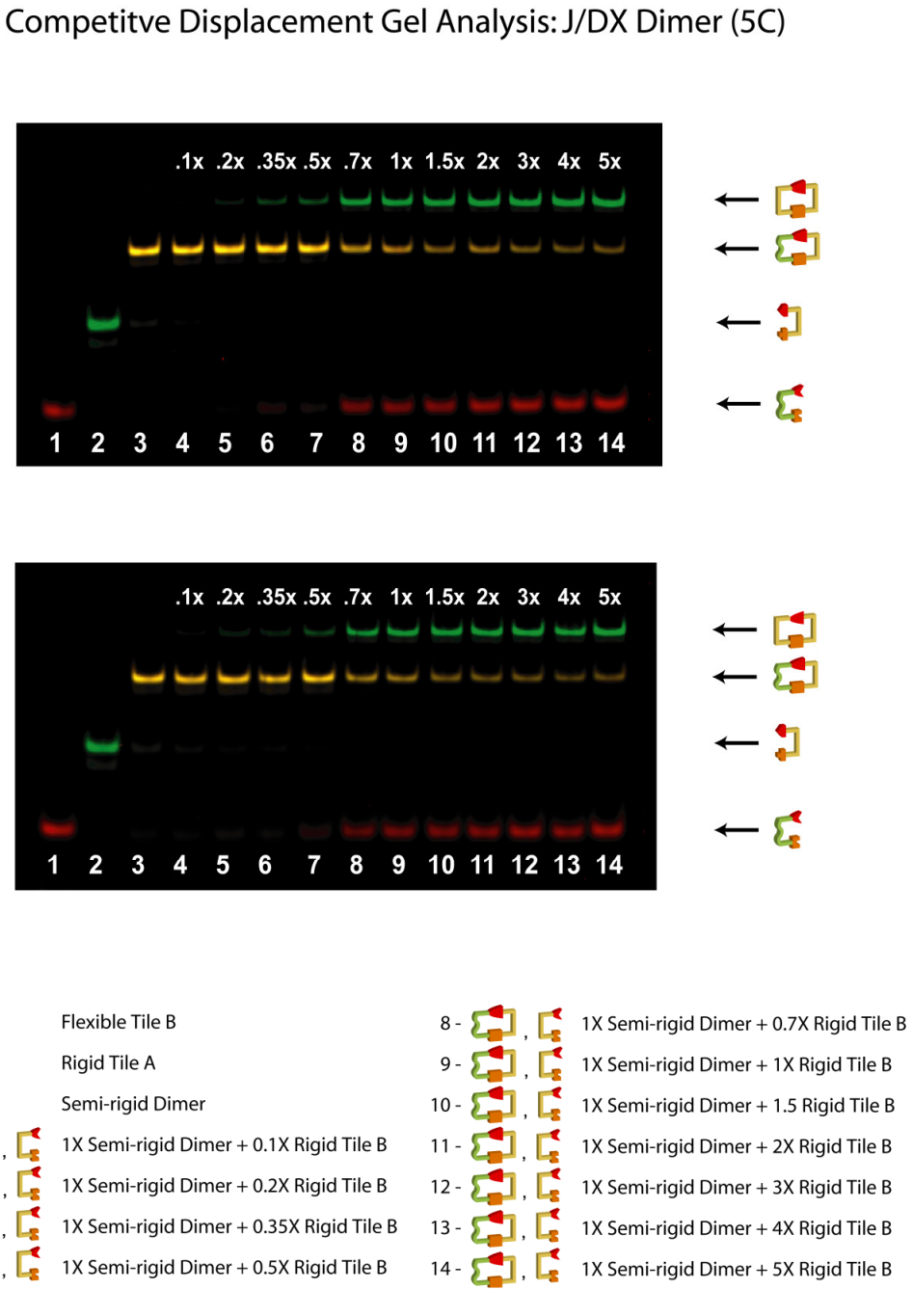

Figure S14. PAGE gel results of the competitive displacement experiments corresponding to the reaction illustrated in Figure 3.4b. Semi-rigid DX-A/J-B dimers are initially assembled, followed by the addition of rigid, DX-B as indicated. The displacement reaction was allowed to proceed for 300 hours at 5C. Two replicate trials are shown.

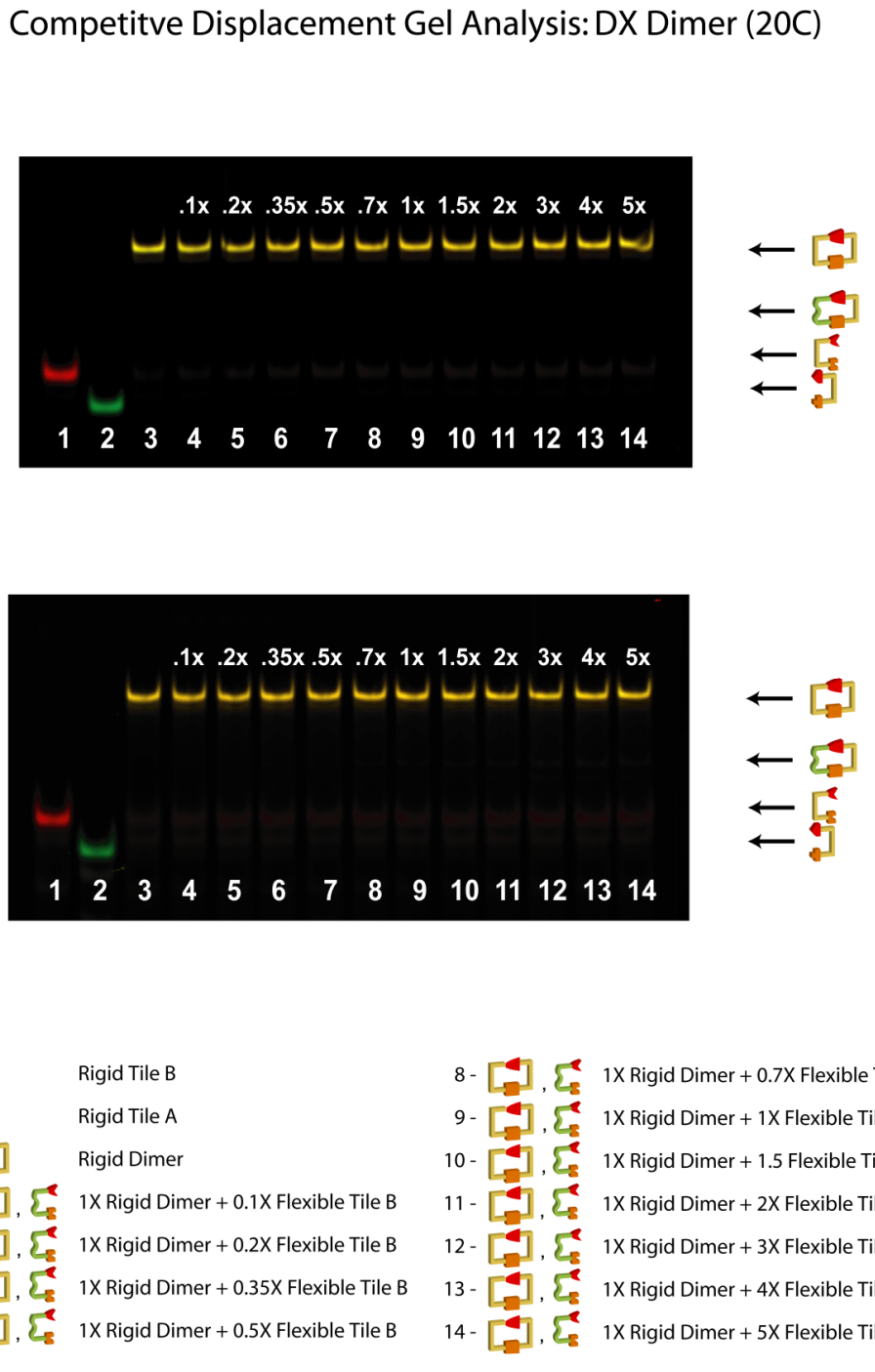

Figure S15. PAGE gel results of the competitive displacement experiments corresponding to the reaction illustrated in Figure 3.4c. Rigid DX-A/DX-B dimers are initially assembled, followed by the addition of flexible, J-B as indicated. The displacement reaction was allowed to proceed for 2 hours at 20C. Two replicate trials are shown.

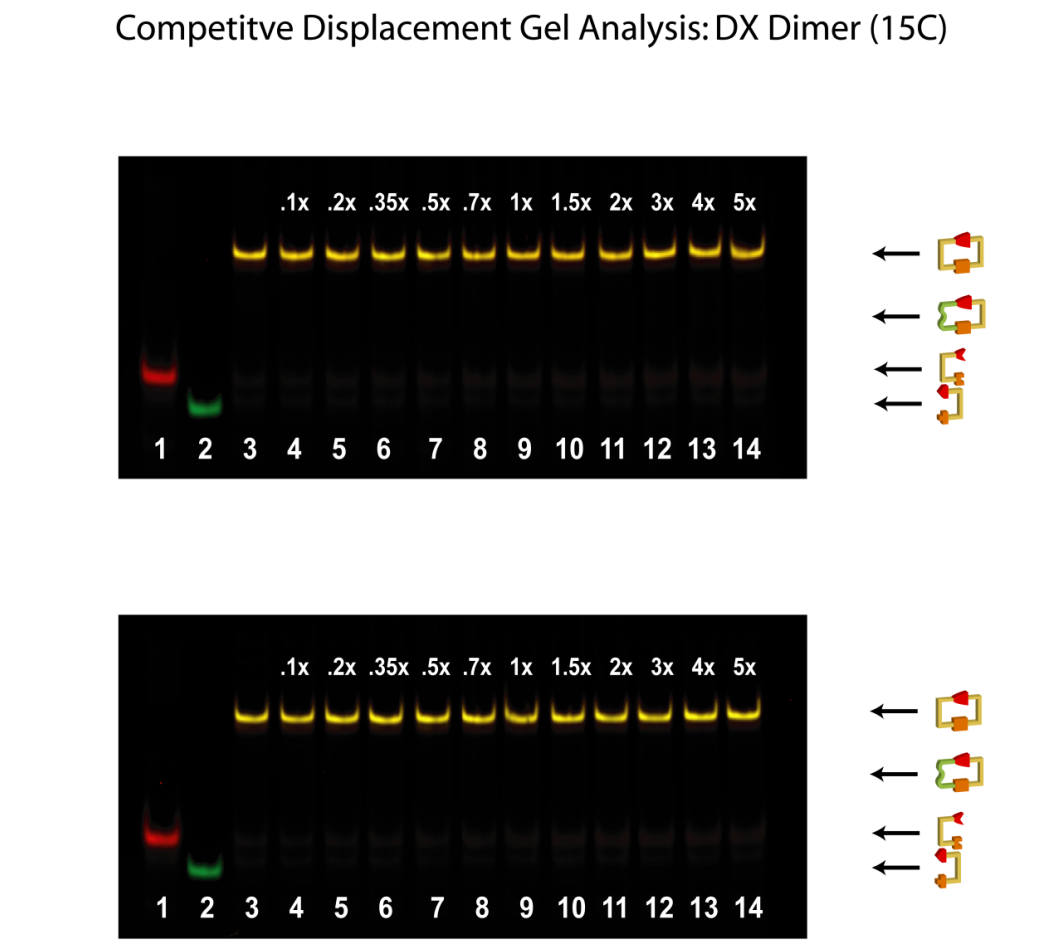

Figure S16. PAGE gel results of the competitive displacement experiments corresponding to the reaction illustrated in Figure 3.4c. Rigid DX-A/DX-B dimers are initially assembled, followed by the addition of flexible, J-B as indicated. The displacement reaction was allowed to proceed for 2 hours at 15C. Two replicate trials are shown.

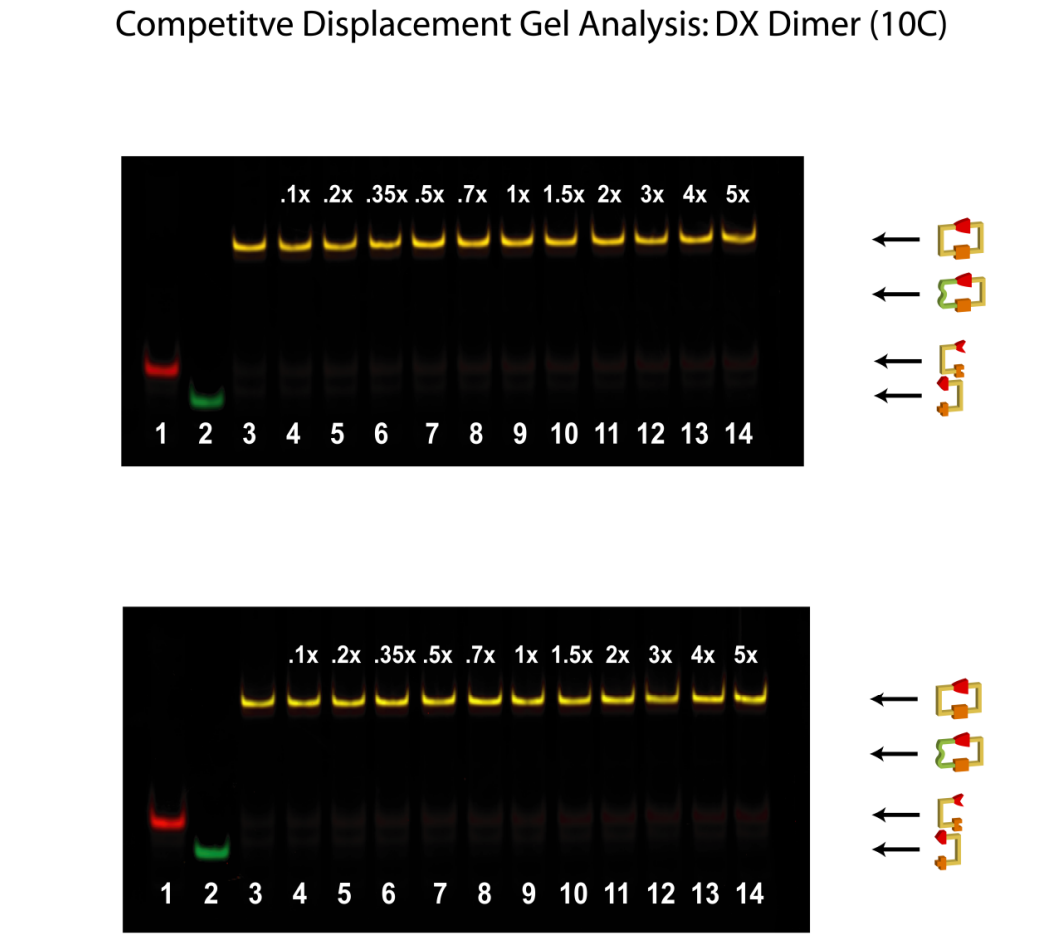

Figure S17. PAGE gel results of the competitive displacement experiments corresponding to the reaction illustrated in Figure 3.4c. Rigid DX-A/DX-B dimers are initially assembled, followed by the addition of flexible, J-B as indicated. The displacement reaction was allowed to proceed for 2 hours at 10C. Two replicate trials are shown.

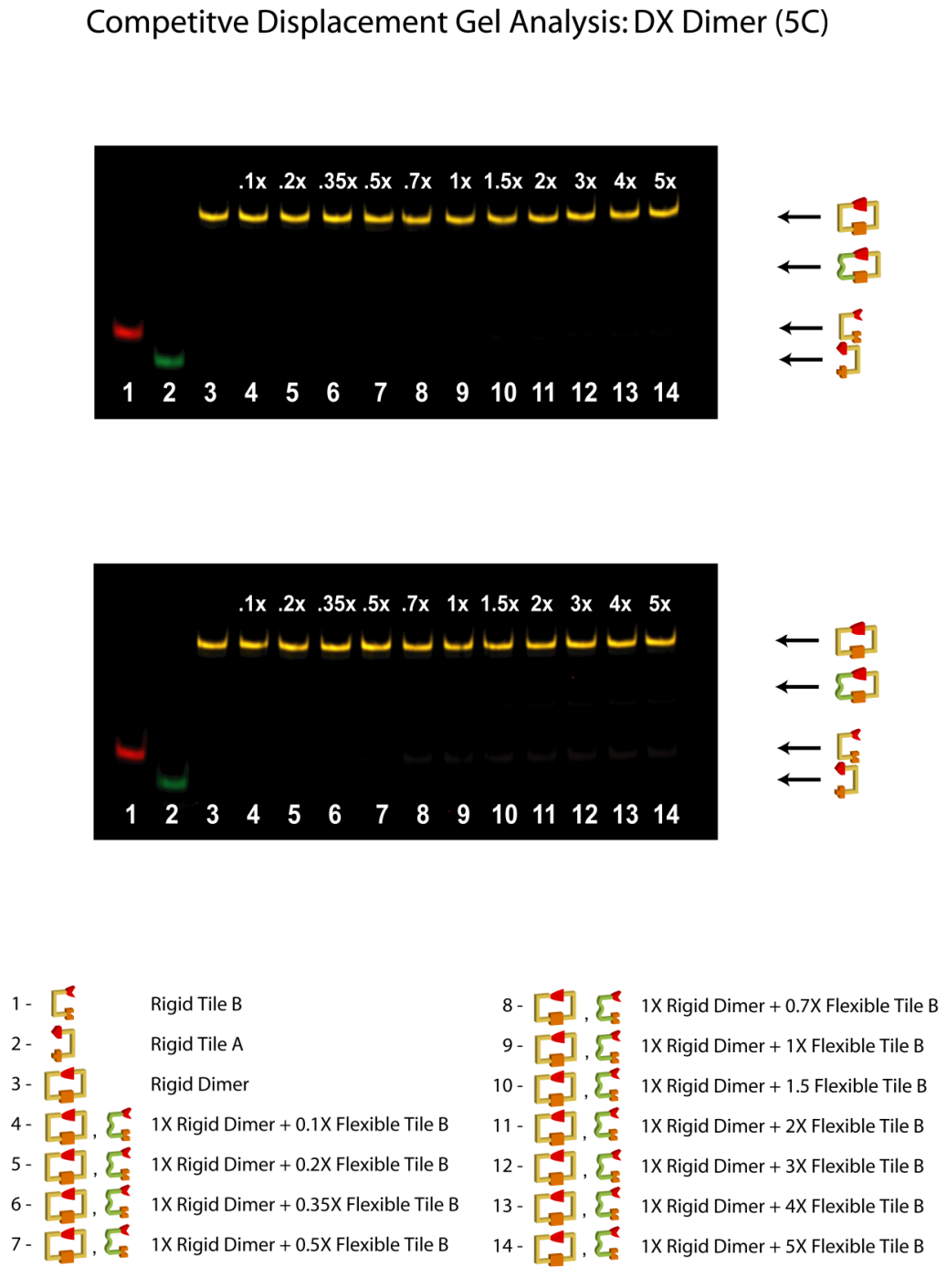

Figure S18. PAGE gel results of the competitive displacement experiments corresponding to the reaction illustrated in Figure 3.4c. Rigid DX-A/DX-B dimers are initially assembled, followed by the addition of flexible, J-B as indicated. The displacement reaction was allowed to proceed for 2 hours at 5C. Two replicate trials are shown.

Additional comments

Below is a graph that represents the results of analyzing multiple measurements of 6 independent samples of the same composition. There are totally 12 Gaussian curve fits (black lines) generated by Origin Pro 7 Software that are overlayed, with two plots corresponding to a single sample, one collected while heating (red dots) and one while cooling (blue dots).

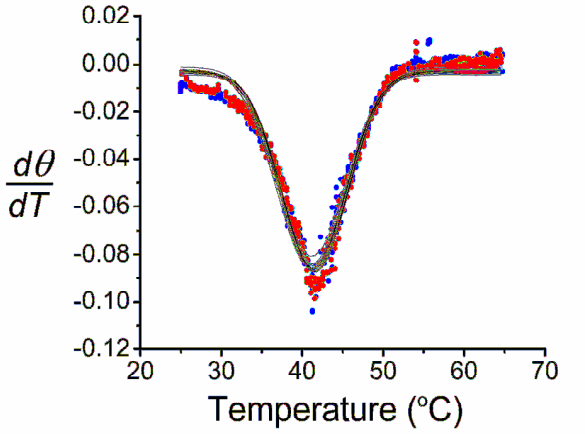

The software generates each Gaussian fit and provides the Tm (xc) and width of each curve (w) as shown in the lower right panel of the graph below.

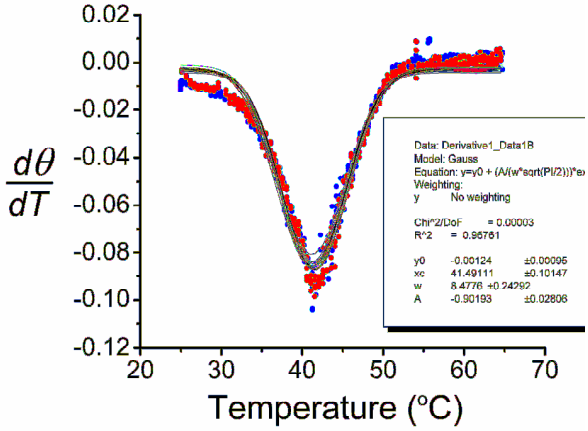

The values that are determined by the software are compiled in an Excel spreadsheet and descriptive statistics are generated by Excel, including the standard deviation reported in Tables 3.1 and 3.2 with the significant numbers reported according to the values of the standard deviation. Below is the excel analysis of a typical sample.

DX Dimer	Tm
Sample 1 Cooling	41.5
Sample 2 Cooling	41.3
Sample 3 Cooling	41.1
Sample 4 Cooling	41.5
Sample 5 Cooling	41.3
Sample 6 Cooling	41.1
Sample 1 Heating	41.4
Sample 2 Heating	41.2
Sample 3 Heating	41.4
Sample 4 Heating	41.6
Sample 5 Heating	41.3
Sample 6 Heating	41.6

Descriptive Statistics	
Mean	41.35833
Standard Error	0.049937
Median	41.35
Mode	41.3
Standard Deviation	0.172986
Sample Variance	0.029924
Kurtosis	-1.00592
Skewness	-0.10508
Range	0.5
Minimum	41.1
Maximum	41.6
Sum	496.3
Count	12

The mean and standard deviation are reported in Tables 3.1 and 3.2. W/2 is also generated in the similar way that provides the width of the transition.

The following is an example of how the error bars are determined for ΔH, ΔS, and ΔG. First, Origin Pro 7 is used to generate the Van't Hoff plots (black dots) that are required to determine ΔH, ΔS. The program is used to generate a linear fit of the data around the transition temperature (red line).

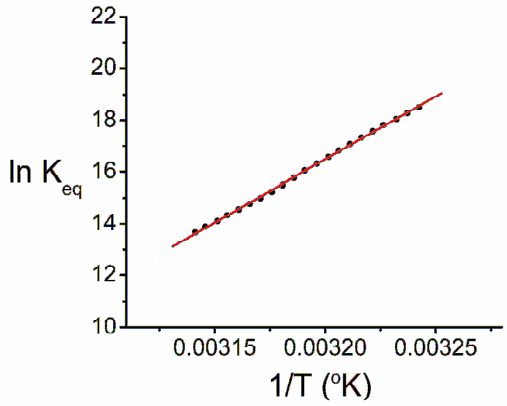

The slope and intercept of the linear fit is provided by the program and entered in an excel spreadsheet for multiple replicates, each represented by cooling and heating data. The equation, $\ln K_{eq} = \frac{-\Delta H}{RT} + \frac{\Delta S}{R}$, is used to relate the slope and intercept directly to ΔH and ΔS. The actual calculations are performed by Excel. A typical data set is shown below.

Replicate	Intercept	Slope	ÄH (kcal/mol)	TÄS (kcal/mol)	ÄS (kcal/mol*K)	ÄG (kcal/mol)
1	-142.48	49651	-98.66	-84.41	-0.283	-14.24
2	-146.85	51093	-101.52	-87.00	-0.292	-14.52
3	-145.73	50696	-100.73	-86.34	-0.290	-14.40
1	-144.07	50165	-99.68	-85.35	-0.286	-14.33
2	-141.64	49493	-98.34	-83.91	-0.281	-14.43
3	-142.94	49846	-99.04	-84.68	-0.284	-14.36

ΔG is related to the experimentally determined values of ΔH and ΔS by the Gibbs equation, $\Delta G = \Delta H - T\Delta S$, where T is 298 K (25 °C). The last column in the table above lists the calculated values of ΔG for this data set. Excel statistic analysis is then used to calculate the mean and standard deviation of the data as shown below.

ΔH (kcal/mol)	*Column1*	
-98.656		
-101.521	Mean	-99.66
-100.733	Standard Error	0.51
-99.679	Median	-99.36
-98.343	Mode	#N/A
-99.044	Standard Deviati	1.24
	Sample Variance	1.55
	Kurtosis	-1.15
	Skewness	-0.64
	Range	3.18
	Minimum	-101.52
	Maximum	-98.34
	Sum	-597.98
	Count	6.00

TΔS (kcal/mol)	*Column1*	
-84.411		
-86.998	Mean	-85.28
-86.335	Standard Error	0.49
-85.352	Median	-85.02
-83.911	Mode	#N/A
-84.682	Standard Deviation	1.19
	Sample Variance	1.41
	Kurtosis	-1.28
	Skewness	-0.50
	Range	3.09
	Minimum	-87.00
	Maximum	-83.91
	Sum	-511.69
	Count	6.00

ΔS (kcal/mol*K)	*Column1*	
-0.283		
-0.292	Mean	-0.286
-0.290	Standard Error	0.002
-0.286	Median	-0.285
-0.281	Mode	#N/A
-0.284	Standard Deviation	0.004
	Sample	0.000

ΔG (kcal/mol)	*Column1*	
-14.245		
-14.523	Mean	-14.38
-14.398	Standard Error	0.04
-14.327	Median	-14.38
-14.431	Mode	#N/A
-14.362	Standard Deviation	0.09
	Sample	0.01

Variance		Variance	
Kurtosis	-1.279	Kurtosis	0.41
Skewness	-0.497	Skewness	-0.11
Range	0.010	Range	0.28
Minimum	-0.292	Minimum	-14.52
Maximum	-0.281	Maximum	-14.24
Sum	-1.716	Sum	-86.29
Count	6.000	Count	6.00

Although the standard deviations for the experimentally determined ΔH and ΔS values are relatively large, when the ΔG values are calculated for each individual data set they all fall into a small range, yielding a very small standard deviation (about one tenth of the standard deviations of the ΔH and $T\Delta S$). An average ΔG value can also be calculated from the average ΔH and ΔS values, which would carry the large error to the calculated ΔG. Here we reported the data calculated from individual data sets, with surprisingly small standard deviations for ΔG, which reveals that the errors in ΔH and ΔS measurements actually compensate each other.

APPENDIX C

SUPPLEMENTAL INFORMATION FOR CHAPTER 4

Supplemental Information

Steric Crowding and the Kinetics of Hybridization in a DNA Nanostructure System*

Jeanette Nangreave, Andre Vidal Pinheiro, Hao Yan*, Yan Liu*

Department of Chemistry & Biochemistry and the Biodesign Institute
Arizona State University, Tempe, AZ, 85287, USA

EXPERIMENTAL

Self-assembly of DNA nanostructures: All DNA strands (Figures S1-S3) used for assembly of nanostructures were purchased from Integrated DNA Technologies, Inc. (www.idtdna.com) and purified by denaturing polyacrylamide gel electrophoresis (PAGE; 6-10% acrylamide in 1X TBE buffer: 89 mM Tris base, 89 mM Boric acid, 2 mM EDTA, pH 8.0) for the unmodified DNA oligomers or by HPLC for the dye labeled DNA oligomers. The design of each 6HX tile included one oligomer with a FAM (5-carboxyfluorescein) dye modification. Assembly of the 6HX tiles was performed by mixing equimolar amounts of all the oligomers present in the structures at a final concentration of 500 nM, in 1x TAE Mg^{2+} buffer (40 mM Tris base, 20 mM Acetic acid, 2 mM $EDTA{\cdot}Na_2{\cdot}12H_2O$, 12.5 mM $((CH_3COO)_2Mg{\cdot}4H_2O)$) for both fluorescence experiments and gel assays. The tiles were self-assembled by heating the oligomer mixtures at 90ºC and cooling to 4ºC over 12 hours, using an automated PCR thermocycler (Mastercycler Pro, Eppendorf). Before real time fluorescence analysis, the 6HX tile solutions were diluted to 1 nM concentration with 1x TAE Mg^{2+} buffer. For steady state fluorescence excitation, steady state fluorescence emission, fluorescence anisotropy measurements, and gel analysis, the samples were diluted to 50 nM concentration with 1x TAE Mg^{2+} buffer. The formation of the self-assembled 6HX tiles was verified by non-denaturing PAGE (5% acrylamide in 1x TAE Mg^{2+} buffer at 200V, 20ºC for ~4 hours (Figures S8-S12).

Fluorescence measurements: All the fluorescence life-time decay measurements were analyzed by a time-correlated single-photon-counting (TCSPC) method using a Titanium Sapphire kilohertz laser system (Millennia/Tsunami, Spectra Physics) with a 130 fs pulse duration operated at 80 MHz, in a 1 cm path length quartz cell (Hellma). The laser output was tuned to 740 nm and sent through a frequency doubler and pulse selector (Spectra Physics, Model 3980) to obtain 370 nm excitations at 4 MHz. Fluorescence emission was collected at a right angle to the excitation beam and detected using a double-grating monochromator (Jobin-Yvon, Gemini-180) and a microchannel plate photomultiplier tube (Hamamatsu R3809U-50). Data acquisition was performed using a single photon counting card (Becker-Hickl, SPC-830), and the emission was collected at 520 nm. The

instrument response function (IRF) had a full width at half-maximum (FWHM) of 35-45 ps, as verified by scattering from samples. Global analysis was performed using the in-house software package, ASUFIT. The lifetime of fluorescence decay of FAM in the 6HX tiles, before and after Target hybridization, was measured using the system described above; unless otherwise indicated, 120 μL of 250 nM 6HX tile solution was used for all measurements.

All steady state and real-time fluorescence spectra were measured by a Nanolog fluorometer (Horiba Jobin Yvon, L-format, equipped with a CW 450W Xenon light source, thermoelectrically cooled R928 PMT, and fully automated excitation and emission polarizers for anisotropy measurements), with a 1 cm path length quartz cell (Hellma); all spectra were corrected for the wavelength dependence of the detection system response. For real-time analysis, the temperature of the quartz cell was controlled/held constant by a refrigerated water recirculator (Thermoscientific). Unless otherwise indicated, 120 μL of 50 nM 6HX tile solution was used for all measurements.

Fluorescence emission spectra were collected in the same way as the excitation spectra, with the exception of experimental parameters. The parameters used to collect emission spectra were: 475 nm excitation wavelength, 5 nm excitation slits, 485-650 nm emission wavelength range, 5 nm emission slits, and 1 second integration time.

Fluorescence anisotropy was also measured in the same manner with the following parameters: 495 nm excitation wavelength, 5 nm excitation slits, 540 nm emission wavelength, 5 nm emission slits and 10 second integration time. Anisotropy values were calculated from the instrument software, FluorEssence for Windows by Horiba Scientific.

Real time measurements: The kinetics of hybridization of a DNA Target to a 6HX tile was monitored in real time via changes in a fluorescence dye reporter molecule (FAM). Changes in FAM fluorescence upon hybridization of the Target were recorded in real time using the system described above; unless otherwise indicated, 120 μL of 1 nM 6HX tile solution was used for all measurements. The parameters used to collect real-time spectra were: 485 nm excitation wavelength, 3 nm excitation slits, 520 nm emission wavelength, 15 nm emission slits, and 0.5 or 1 second integration time depending on the total measurement time. The tile bearing a FAM dye was tested for photobleaching under continuous excitation exposure. A reduction in overall emission of an equilibrated solution of 2-5% was found, over the course of each experiment. The temperature was held constant for the measurement period of all real-time data collection; the following temperatures were used: 11°C, 14°C, 16°C, 18°C, and 20°C.

Data collection: first, the temperature of the fluorometer cell holder and the 6HX tile sample under investigation were allowed to equilibrate for a given period of

time before any measurements were taken. After reaching the desired temperature, the tile solution was loaded in the cuvette and the cuvette was inserted in the instrument. The temperature of the instrument and sample were again allowed to equilibrate for 2 and 5 minutes, then data collection was initiated. The fluorescent signal was collected as a function of time for a given period. Typically, the signal was collected for time duration of 150 to 350 seconds, depending on the particular sample under investigation and the expected length of the subsequent hybridization reaction. The resulting spectra confirmed the stability (resistance to photobleaching) of the fluorophore in the sample over the course of the experiment. Next, data collection was again initiated and 20 equivalents of unlabeled Target were directly added to the cuvette while it was still in the instrument (in the dark). The solution was mixed by pipetting for 1-2 seconds and the kinetics of hybridization of the target was monitored for the length of the reaction. The resulting spectra reflected the changes in FAM emission that occurred as the Target hybridized to the 6HX tiles. The kinetic measurements were repeated at least 5 times for every design under investigation. Several control experiments were performed to confirm the sample addition process resulted in homogeneous mixing, and the results showed that the mixing delay was negligible compared to the hybridization kinetics. The kinetic curves were subsequently fit by a mono-exponential growth model and the bimolecular rate constants were extracted by dividing the time constant by the Target concentration.

Native gel electrophoretic characterization of nanostructures: The correct assembly of all 6HX tile designs under consideration and subsequent hybridization of all Target and Off Target DNA was confirmed by non-denaturing polyacrylamide gel electrophoresis at 200V, 10-20ºC for ~4 hours. 7 pmoles of each 6HX tile, before and after addition of 5 equivalents of Target, were analyzed by 5% nondenaturing PAGE gels in 1x TAE Mg buffer.

FIGURES

The crossover design and components of the 6HX DNA tiles studied in this report are shown in SI Figures S1-S7, including the sequences of the DNA strands used. Results of the non-denaturing polyacrylamide gel electrophoretic characterizations of the designs investigated in this study are shown in Figures S8-S12. Addition spectra and kinetic measurements are shown in Figures S13-20.

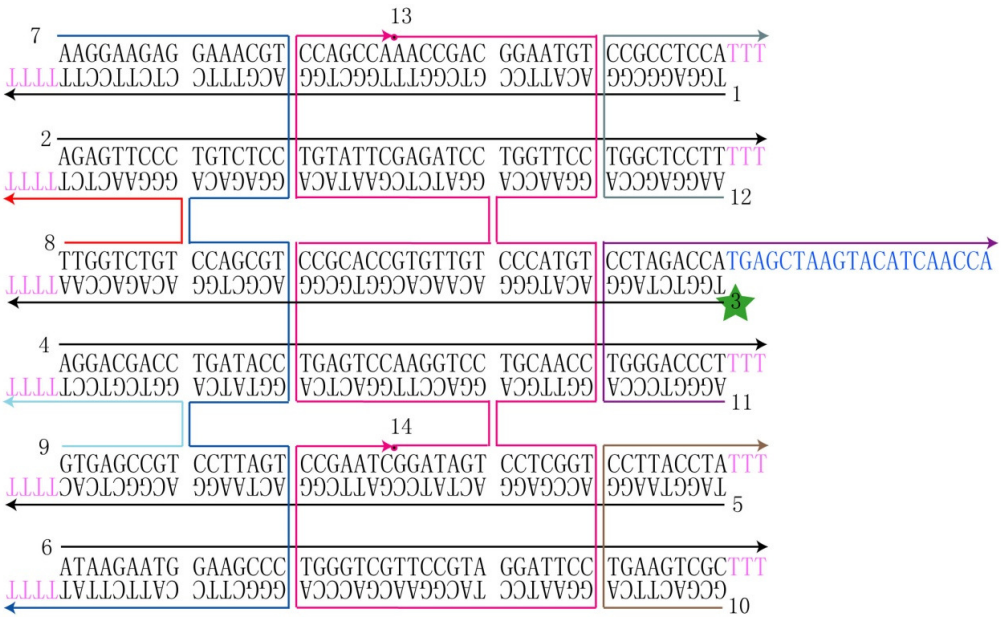

Figure S1. Schematic diagram of the 6HX tile design used for experiment with no DNA surrounding the site of hybridization. The sequences of the constituent strands are indicated in the scheme. A Target Probe (20 nucleotide sequence in blue at the 3' end of strand 11) is located at Position C, with FAM dye represented as a green star at the 5' end of strand 3. The design of 6HX tiles with Target Probes located at Positions A and B are identical to the illustrated schematic, with the exception of the particular location of the Target Probe and FAM dye label. For all designs, the 3' poly T termini (shown in pink on the left and right sides) of certain strands and were used to prevent non-specific association between 6HX tiles.

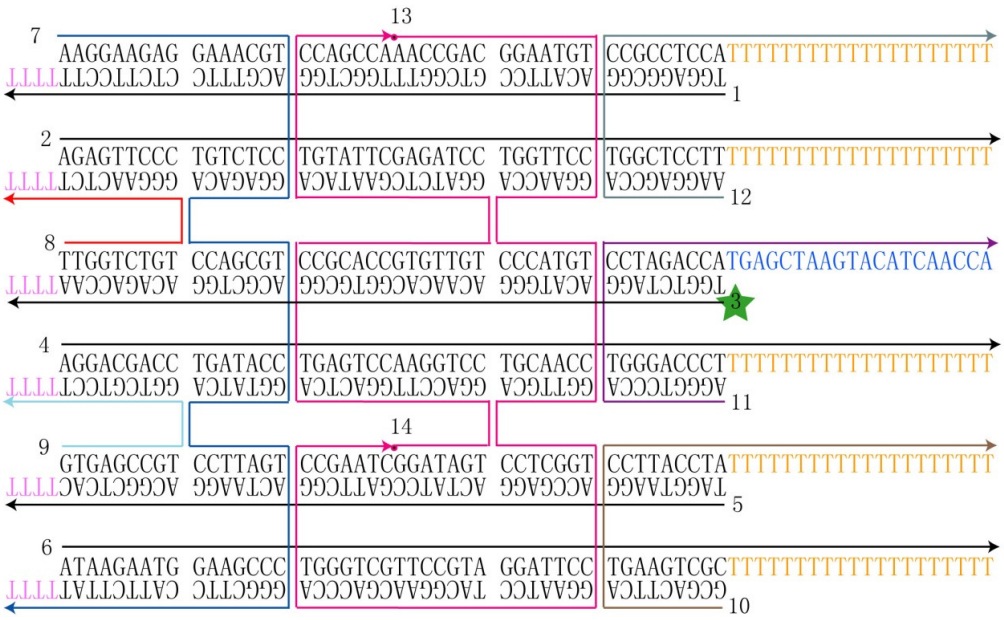

Figure S2. Schematic diagram of the 6HX tile design used for experiment with single stranded DNA surrounding the site of hybridization. A Target Probe (20 nucleotide sequence in blue at the 3' end of strand 11) is located at Position C, with FAM dye modified at the 5' end of strand 3 (green star). Single stranded extensions (20 nucleotide poly T sequences shown in orange at the 3' ends of strands 2, 4, 6, 10, and 12 for this design) crowding the site of Target hybridization. In addition, the poly T sequences used for the Off Target Probes ensure minimal interactions among the probes and between tiles. The design of 6HX tiles with Target Probes located at Positions A and B are identical to the illustrated schematic, with the exception of the particular location of the Target Probe and FAM dye label.

Figure S3. Schematic diagram of the 6HX tile design used for experiment with double stranded DNA surrounding the site of hybridization. A Target Probe is located at Position C, with FAM dye modified at the 5' end of strand 3 (green star). There are single stranded Off Target Probe extensions (20 nucleotide random sequences shown in orange at the 3' ends of strands 2, 4, 6, 10, and 12 for this design) that are used to recruit the Off Target to specific helices (20 nucleotide complement to the extensions, shown in brown). Off Target and Off Target Probe extension sequences were optimized to reduce the formation of undesirable secondary structures using NUPACK software (unpack.org). Before all analyses, including gel electrophoresis and kinetics of Target hybridization, the Off Target strand was hybridized to each Off Target Probe position, shielding the site of Target hybridization considerably. The design of 6HX tiles with Target Probes located at Positions A and B are identical to the illustrated schematic, with the exception of the particular location of the Target Probe and FAM dye label.

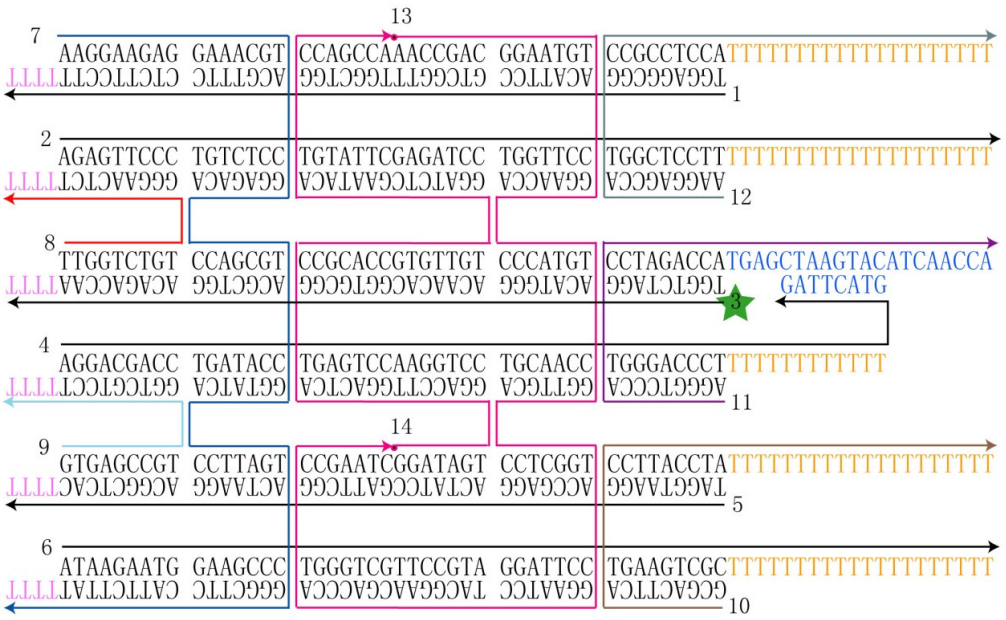

Figure S4. Schematic diagram of a 6HX tile design used for experiments to assess the effect of interactions of the Target Probe with a single stranded Off Target Probe adjacent to the site of Target hybridization and the resulting secondary structure, on the hybridization kinetics. The schematic corresponds to the design with a Target Probe (blue) located at Position C, with FAM dye modified at the 5' end of strand 3 (green star). There are single stranded extensions (20 nucleotide poly T sequences shown in orange at the 3' ends of strands 2, 6, 10, and 12 for this design) surrounding the site of Target hybridization. 8 nucleotides at the 3' end of strand 4 (shown in blue) are complementary to 8 nucleotides of the Target Probe, resulting in the formation of an 8 base-pair double helix between the Target Probe and Off Target Probe 4.

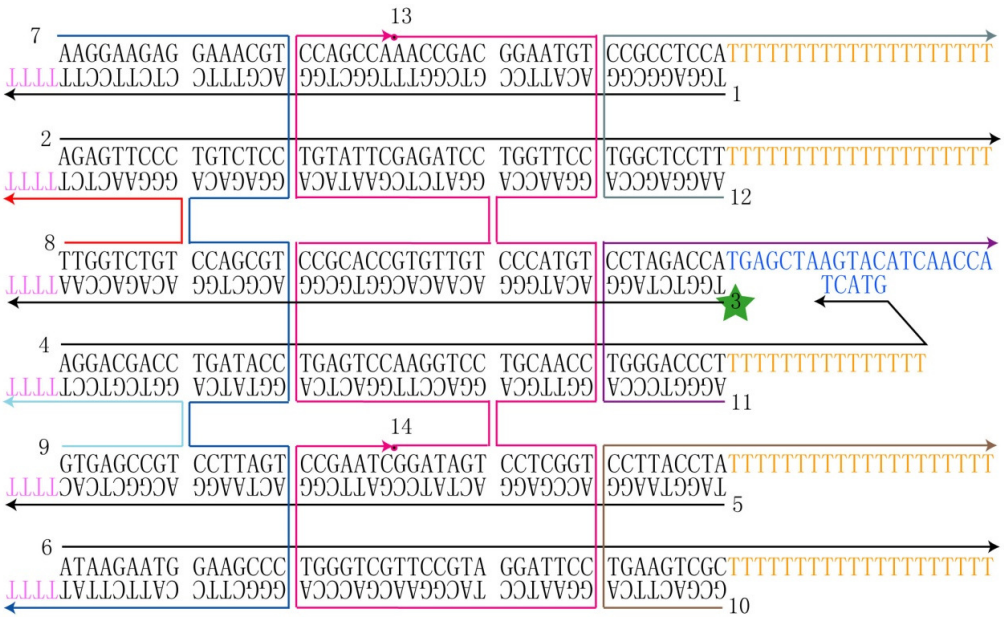

Figure S5. Schematic diagram of a 6HX tile design used to assess the effect of interactions of the Target Probe with a single stranded Off Target Probe adjacent to the site of Target hybridization and the resulting secondary structure, on the hybridization kinetics. The design is the same as shown in **Figure S4,** except that 5 nucleotides at the 3' end of strand 4 (shown in blue) are complementary to 5 nucleotides of the Target Probe, resulting in the formation of a 5 base-pair double helix between the Target Probe and Off Target Probe 4.

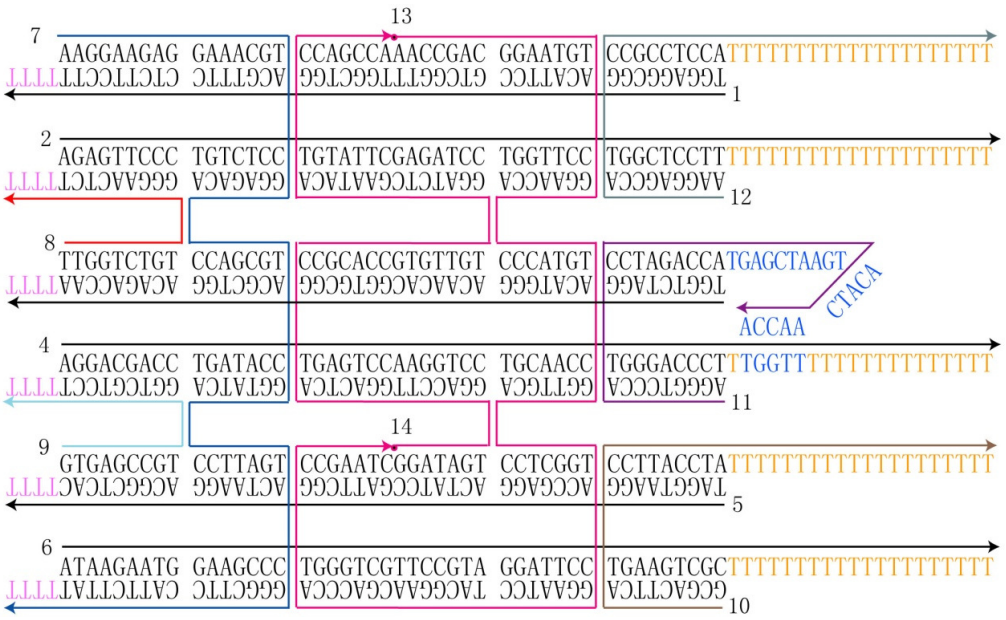

Figure S6. Schematic diagram of a 6HX tile design used for experiments to assess the effect of interactions of the Target Probe with a single stranded Off Target Probe adjacent to the site of Target hybridization and the resulting secondary structure, on the hybridization kinetics. The design is the same as shown in **Figure S5,** except that 5 nucleotides within the Off Target Probe extension of strand 4 (shown in blue) are complementary to 5 nucleotides of the Target Probe, providing a 'docking' station for the complementary nucleotides of the Target Probe.

Figure S7. Schematic diagram of a 6HX tile design used for experiments to assess the effect of interactions of the Target Probe with a single stranded Off Target Probe adjacent to the site of Target hybridization and the resulting secondary structure, on the hybridization kinetics. The design is the same as shown in **Figure S6,** except that 8 nucleotides within the Off Target Probe extension of strand 4 (shown in blue) are complementary to 8 nucleotides of the Target Probe, providing a 'docking' station for the complementary nucleotides of the Target Probe.

Please not that the sequence of the Target, 5'-TGGTTGATGTACTTAGCTCA, remained constant for all designs.

Figures S8 – S12 contain the electrophoretic characterization of all 6HX tile designs used in the study. All nondenaturing PAGE analyses were performed under the following conditions: 5% acrylamide, constant 200V, 11°C, ~4 hours, and ethidium bromide staining for visualization of the DNA.

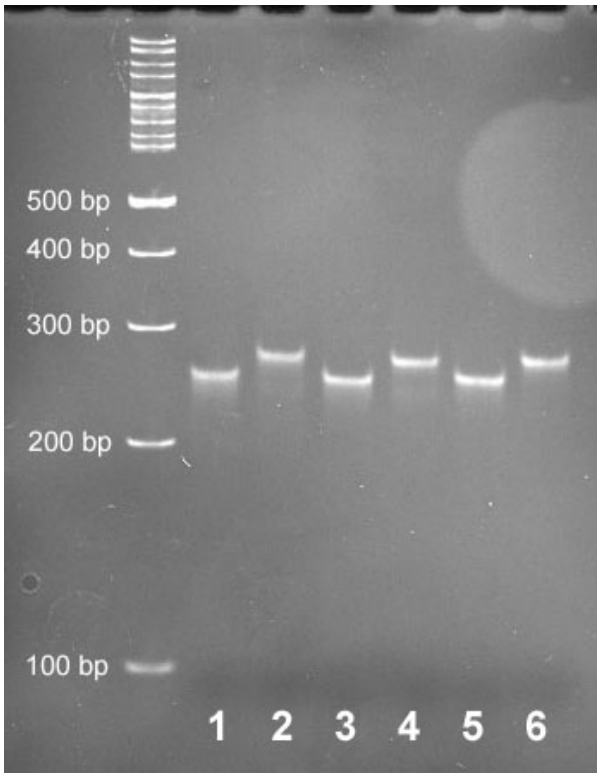

Figure S8. Characterization of 6HX with no DNA surrounding the Target hybridization site. Left lane- 100 bp ladder; lanes 1, 3, and 5 contain 0.5 pmole of 6HX tile with a FAM label and the Target Probe at Position A, B and C, respectively; and lanes 2, 4, and 6 have the same contents as lanes 1, 3, and 5, plus 5 equivalents of Target, added after tile formation.

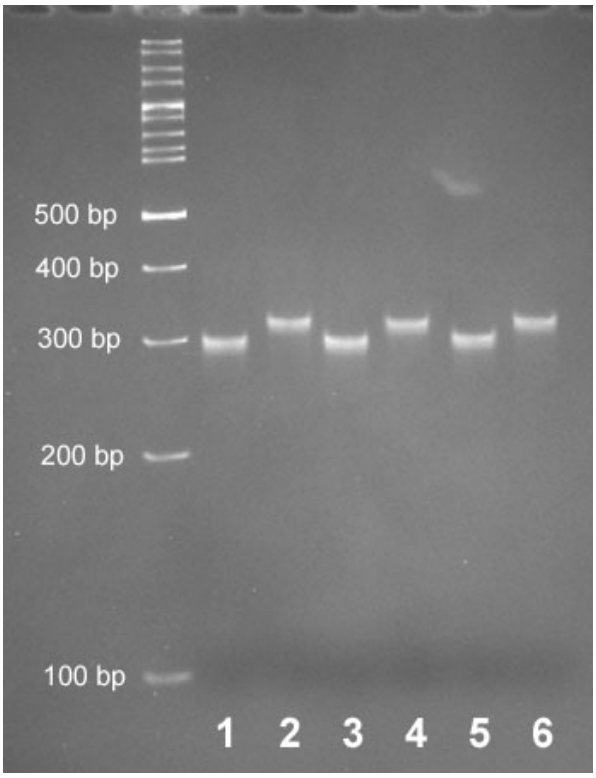

Figure S9. Characterization of 6HX with single stranded DNA surrounding the Target hybridization site. Left lane- 100 bp ladder; lanes 1, 3, and 5 contain 0.5 pmole of 6HX tile with a FAM label and the Target Probe at Position A, B and C, respectively; and lanes 2, 4, and 6 have the same contents as lanes 1, 3, and 5, plus 5 equivalents of Target, added after tile formation.

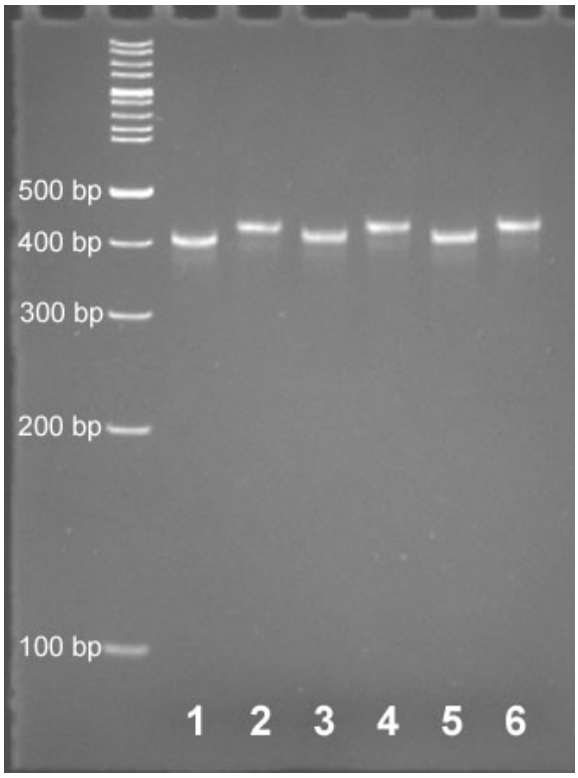

Figure S10. Characterization of 6HX with double stranded DNA surrounding the Target hybridization site. Left lane- 100 bp ladder; lanes 1, 3, and 5 contain 0.5 pmole of 6HX tile with a FAM label and the Target Probe at Position A, B and C, respectively; and lanes 2, 4, and 6 have the same contents as lanes 1, 3, and 5, plus 5 equivalents of Target, added after tile formation and Off Target hybridization.

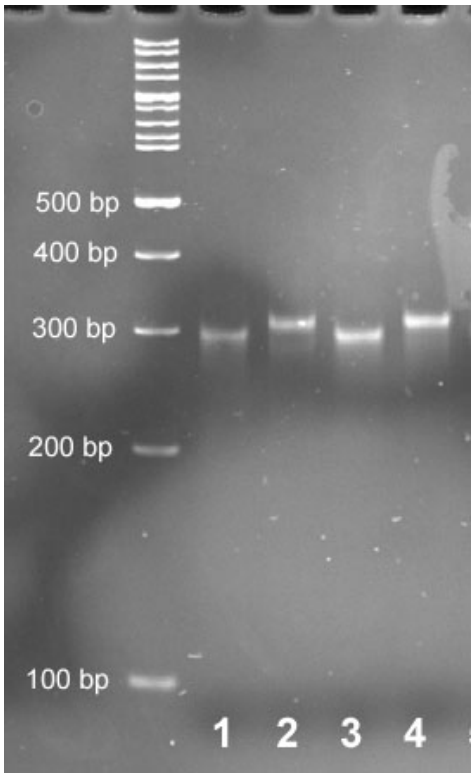

Figure S11. Characterization of 6HX with the Off Target Probe partially complementary to the adjacent Target Probe (a secondary structure formed from interaction between the probes with the *Off Target Probe* bending to hybridize to an extended Target Probe). Left lane - 100 bp ladder; lane 1 – 6HX tile with FAM label and Target Probe at Position C, with a 5 base pair interaction between the Target Probe and adjacent Off Target Probe; lane 2 – the same contents as in lane 1, plus 5 equivalents of Target; lane 3 – 6HX tile with FAM label and Target Probe at Position C, with an 8 base pair interaction between the Target Probe and adjacent Off Target Probe; lane 4 – the same contents as in lane 3, plus 5 equivalents of Target.

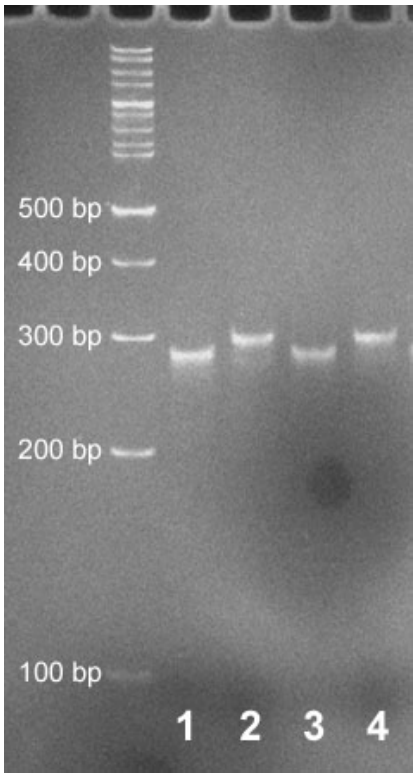

Figure S12. Characterization of 6HX with the Target Probe partially complementary to the adjacent Off Target Probe (the secondary structure formed from interaction between the probes with the *Target Probe* bending to hybridize to an extended Off Target Probe). Left lane - 100 bp ladder; lane 1 – 6HX tile with FAM label and Target Probe at Position C with a 5 base pair interaction between the Target Probe and adjacent Off Target Probe; lane 2 – the same contents as in lane 1 plus 5 equivalents of Target; lane 3 – 6HX tile with FAM label and Target Probe at Position C with an 8 base pair interaction between the Target Probe and adjacent Off Target Probe; lane 4 – the same contents as in lane 3 plus 5 equivalents of Target.

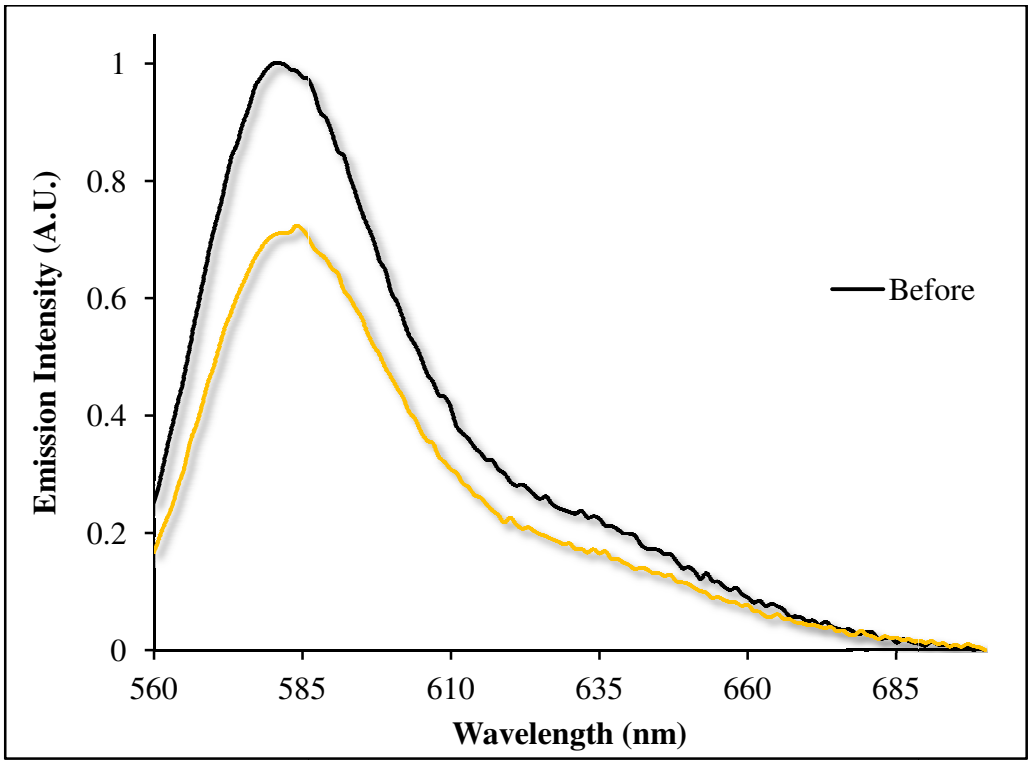

Figure S13. Effect of hybridization on the emission of TAMRA. TAMRA-labeled Target was added to a unlabelled 6HX tile with a Target probe located at position C (equimolar ratio of Target and tile, both 50 nM)**.** The black and yellow trace are emission spectra of a TAMRA-labeled Target strand, before and after hybridization to the 6HX tile. A 27% decrease in emission intensity and a 3-4 nm red-shift was observed after hybridization. Excitation was performed at 550 nm.

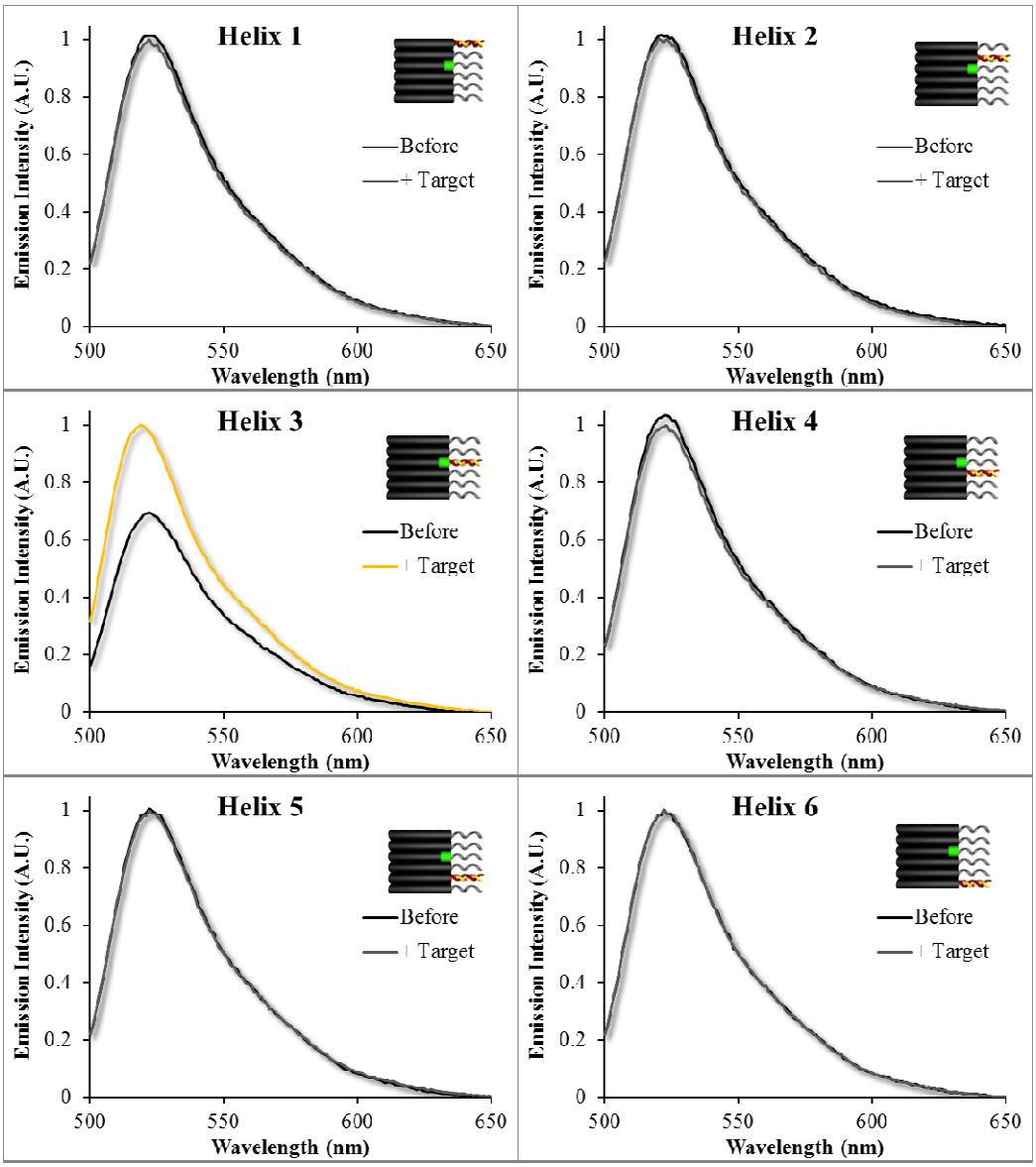

Figure S14. The positional effect of hybridization of an unlabeled Target on the emission of a Position C-FAM-labeled 6HX tile. Steady-state emission spectra of 6HX tiles (50 nM) labeled with FAM at Position C, before (black line) and after (gray or yellow line) the addition of 5 equivalents of Target. Each graph reveals the change in FAM emission upon Target hybridization to the denoted position, with the position of the dye held constant for all cases (Position C, Helix 3). The results demonstrate that an increase in emission only occurs when the Target hybridizes to Helix 3, the same helical position as the dye. The after/before hybridization enhancement ratios are shown in **Figure 4.3** in the main text. Excitation was performed at 475 nm.

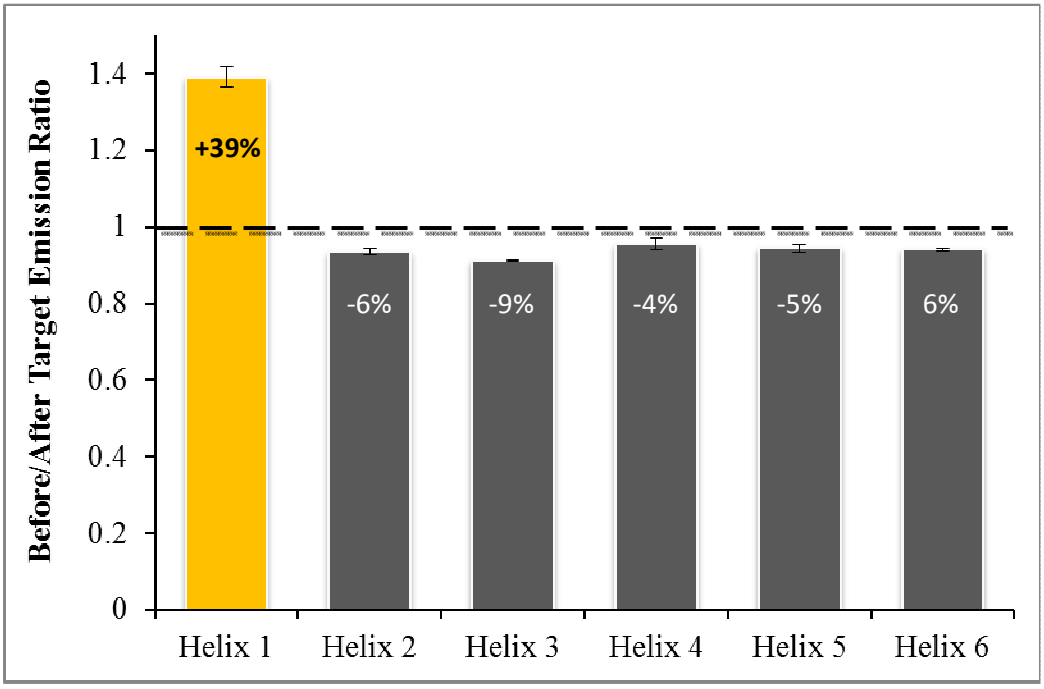

Figure S15. The positional effect of hybridization of an unlabeled Target on the emission of a Position A-FAM-labeled 6HX tile. Steady-state emission spectra of 6HX tiles (50 nM) labeled with FAM at Position A were measured before and after the addition of 5 equivalents of Target. For each sample, the Target Probe was located at a different helical position within the tile (denoted beneath each bar in the graph), while the position of the FAM dye was held constant. The results demonstrate that enhancement in emission only occurs when hybridization occurs when the Target hybridizes to Helix 1, the same helical position as the dye. Excitation was performed at 475 nm.

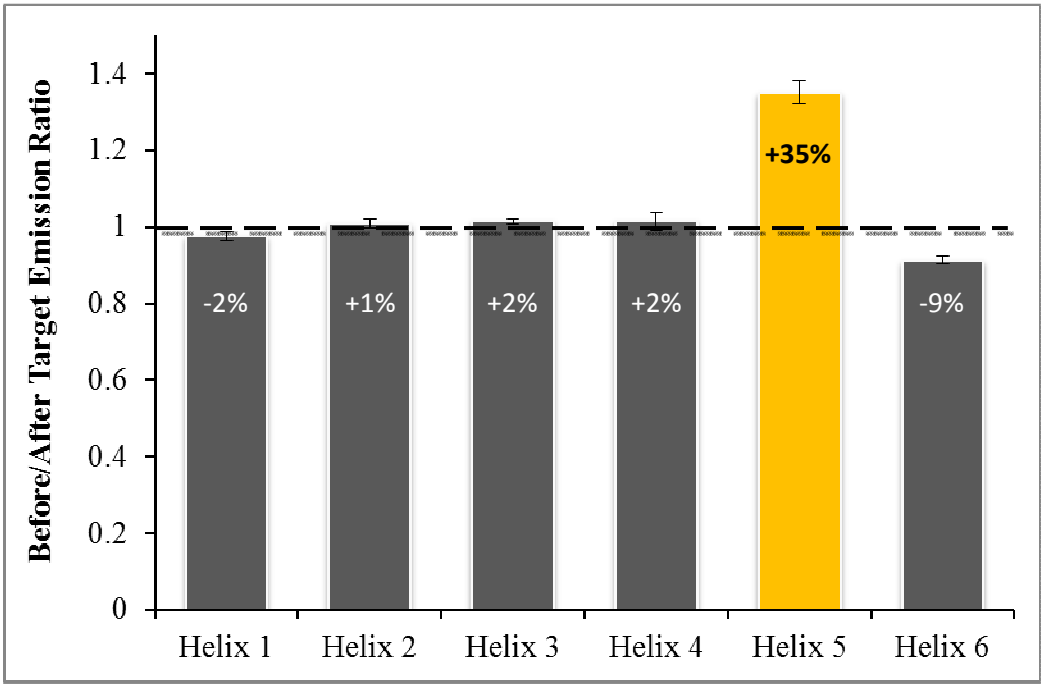

Figure S16. The positional effect of hybridization of an unlabeled Target on the emission of a Position B-FAM-labeled 6HX tile. Steady-state emission spectra of 6HX tiles (50 nM) labeled with FAM at Position B (helix 5) were measured before and after the addition of 5 equivalents of Target. For each sample, the Target Probe was located at a different helical position within the tile (denoted beneath each bar in the graph), while the position of the FAM dye was held constant. The results demonstrate that enhancement in emission only occurs when hybridization occurs when the Target hybridizes to Helix 5, the same helical position as the dye. Excitation was performed at 475 nm.

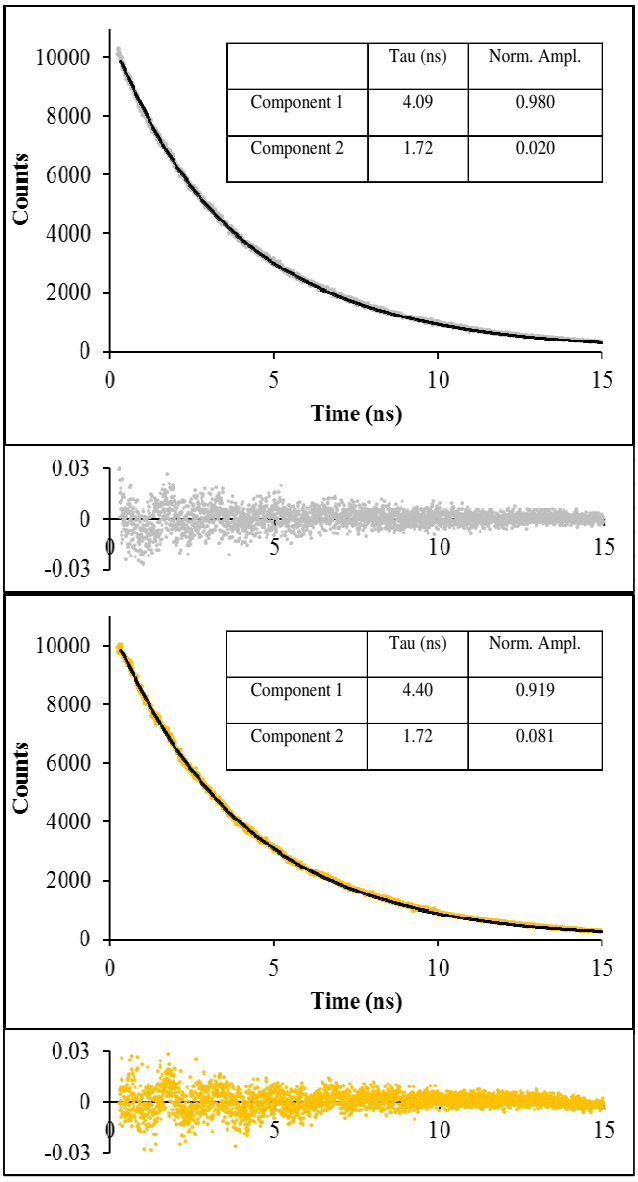

Figure S17. Time-resolved fluorescence decay spectra of FAM-labeled 6HX tiles (Position C) **before (upper panel; gray series) and after (lower panel; yellow series) hybridization of the Target.** The sample contains 250 nM 6HX tile and 1.25 µM Target. Excitation was at 370 nm, and emission collected at 520 nm. The decays were fit by a bi-exponential law and residual analysis is presented below the decays. Lifetimes and normalized amplitudes are indicated in the inset tables. **Figures S18-S20** show the Arrhenius plots of 6HX tiles in the presence of no-, single-stranded- and double-stranded DNA surrounding the site of Target hybridization. The values obtained for the activation energies and pre-exponential factors corresponding to the various hybridization reactions are included **Table 4.1** in the main text.

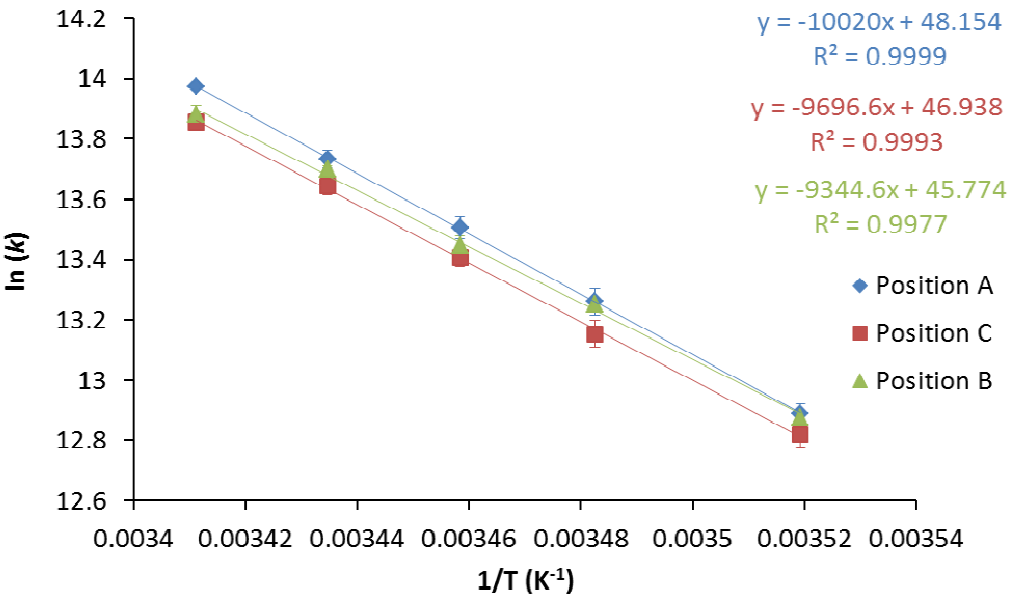

Figure S18. Arrhenius Plots corresponding to the hybridization of the Target to a 6HX tile in the absence of DNA surrounding the site of hybridization. Rate constants corresponding to the hybridization of a Target strand to a 6HX FAM-labeled tile with Target Probe located at Position A (blue series), Position B (green series) and Position C (red series) were measured at different temperatures. The plot of the rate constants as a function of temperature confirms a linear relationship that was fit by a linear regression. The regression equation and R^2 values are presented in the graph. Error bars represent the standard deviation of the values obtained for the rate constant at each temperature (N = 7). Kinetic constants were determined as previously described, using 1 nM 6HX tile and the addition of 20 equivalents of Target, in 1x TAE Mg^{2+} buffer.

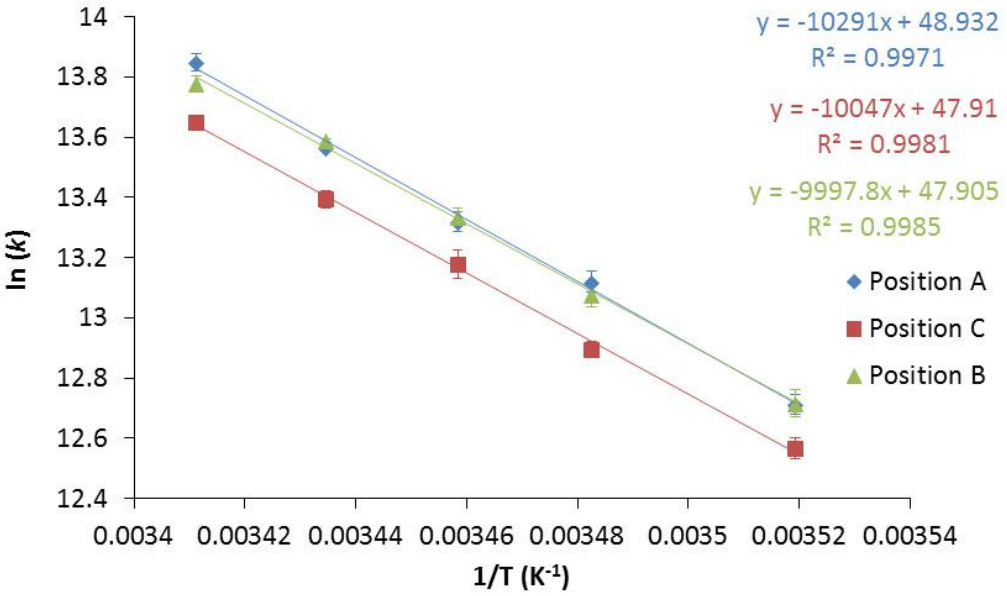

Figure S19. Arrhenius Plots corresponding to the hybridization of the Target to a 6HX tile in the presence of single stranded DNA surrounding the site of hybridization. Rate constants corresponding to the hybridization of a Target strand to a 6HX FAM-labeled tile with Target Probe located at Position A (blue series), Position B (green series) and Position C (red series) were measured at different temperatures. The plot of the rate constants as a function of temperature confirms a linear relationship that was fit by a linear regression. The regression equation and R^2 values are presented in the graph. Error bars represent the standard deviation of the values obtained for the rate constant at each temperature (N = 7). Kinetic constants were determined as previously described, using 1 nM 6HX tile and the addition of 20 equivalents of Target, in 1x TAE Mg^{2+} buffer.

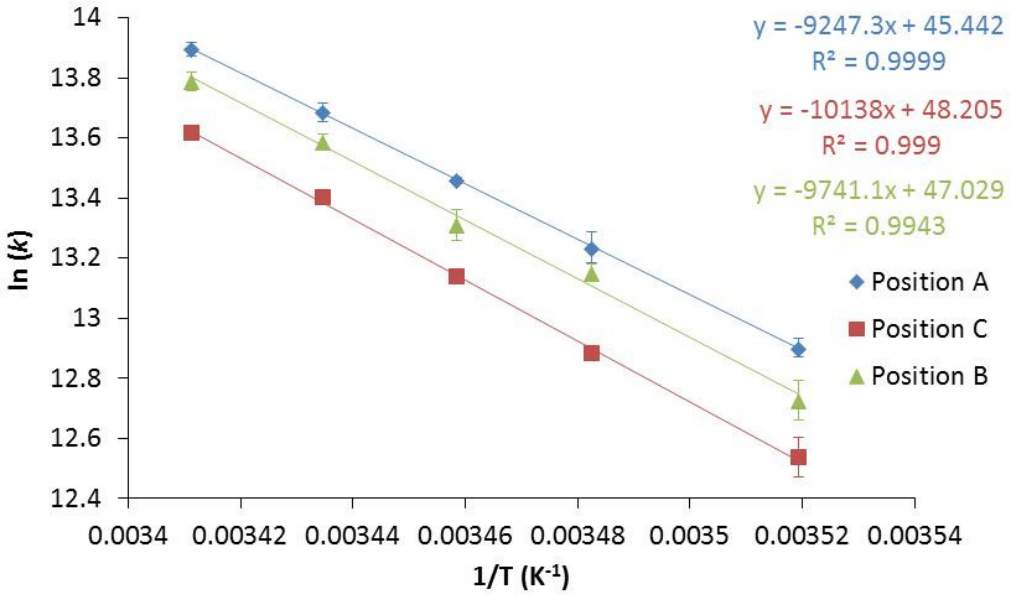

Figure S20. Arrhenius Plots corresponding to the hybridization of the Target to a 6HX tile in the presence of double stranded DNA surrounding the site of hybridization. Rate constants corresponding to the hybridization of a Target strand to a 6HX FAM-labeled tile with Target Probe located at Position A (blue series), Position B (green series) and Position C (red series) were measured at different temperatures. The plot of the rate constants as a function of temperature confirms a linear relationship that was fit by a linear regression. The regression equation and R^2 values are presented in the graph. Error bars represent the standard deviation of the values obtained for the rate constant at each temperature (N = 7). Kinetic constants were determined as previously described, using 1 nM 6HX tile and the addition of 20 equivalents of Target, in 1x TAE Mg^{2+} buffer.

APPENDIX D

CO-AUTHOR APPROVAL

I verify that the following co-authors have approved of my use of our publications in my dissertation.

Yan Liu (Arizona State University)

Hao Yan (Arizona State University)

Andre-Vidal Pinheiro (Arizona State University)